

**Investigating the Relationship between Small and
Large Scale Test Methods for the Combustion
Toxicity of Cables**

by

Cameron Smith

A thesis submitted in partial fulfilment for the requirements of the degree of
Master of Philosophy at the University of Central Lancashire

December 2010

Student Declaration

Concurrent registration for two or more academic awards

I declare that while registered as a candidate for the research degree, I have not been a registered candidate or enrolled student for another award of the University or other academic or professional institution

Material submitted for another award

I declare that no material contained in the thesis has been used in any other submission for an

academic award and is solely my own work

Collaboration

Where a candidate's research programme is part of a collaborative project, the thesis must indicate in addition clearly the candidate's individual contribution and the extent of the collaboration. Please state below:

The raw data for the large-scale test is the only data displayed that wasn't produced by me, as stated in the thesis. However all subsequent interpretation, manipulation and analysis was carried out by myself.

Signature of Candidate _____

Type of Award _____ MPhil _____

School _____ Forensic and Investigative Sciences _____

ABSTRACT

This project aimed to investigate the relationship between large and small scale testing for the combustion toxicity of cables. Cables can present a significant fire hazard due to the location in which they are installed; they are often located in hidden ducts or passageways that circumvent existing fire compartments. This potentially allows a cable fire to progress both swiftly and unnoticed through a building. Also investigated was the comparison of combustion toxicity between Polyvinyl Chloride (PVC) and a selection of Low Smoke Zero Halogen (LSOH) cable materials.

The large scale data that was being used to compare was of unknown ventilation conditions, thus the small scale testing was carried out across a range of ventilation conditions, defined by their equivalence ratio (ϕ), in order to be able to try and assign a ϕ value to the large scale data and thus quantify the ventilation conditions.

To compare the data a range of methods were utilised including equivalence ratio, CO₂/CO ratio, CO/CO₂ ratio, and heat release rate in both kW/g and kJ/g. They met with varying degrees of success, of those tried the most successful was the equivalence ratio, but only when combined with the large scale yield calculated using CO₂ based mass loss.

Highlighted by this research was the need for accurate mass loss estimation in the large scale test. The use of CO₂ based mass loss estimation was an improvement over the estimations based on burn length and TGA data; but there are still issues with the assumptions made during the CO₂ based mass loss calculations, such as the main polymer content being polyethylene and not taking into account the effect of other compounds such as chalk would have on the amount of CO₂ produced.

In terms of comparing toxicity the PVC cable shows a much higher toxicity across all ventilation conditions, with the main contribution to PVC cable's toxicity being HCl,

with HCl having the highest contribution in the most well ventilated conditions, lowering as ventilation decreases.

Table of Contents

ABSTRACT	i
List of Tables	viii
List of Figures	ix
Acknowledgements.....	1
List of Abbreviations and Terms	2
Aims and Objectives.....	2
1. INTRODUCTION	3
1.1 CABLES.....	3
1.2 FREE RADICAL REACTIONS.....	4
1.3 POLYMERS	5
1.3.1 Polymer Synthesis.....	5
1.3.1.1 Chain-reaction Polymerisation.....	6
1.3.1.2 Step-reaction Polymerisation	6
1.3.2 Polymer Decomposition	6
1.3.2.1 Physical Changes	7
1.3.2.2 Chemical Changes	7
1.3.2.2.1 Main Chain Mechanisms	8
1.3.2.2.1.1 Cross Linking.....	8
1.3.2.2.1.3 Chain Scission	8
1.3.2.2.2 Side Chain Mechanisms.....	10
1.3.2.2.2.1 Side Chain Elimination.....	10
1.3.2.2.2.2 Side Chain Cyclisation.....	10
1.4. IGNITION.....	10
1.4.1 Piloted Ignition.....	10
1.4.2 Auto-ignition	11
1.5 FIRE.....	12
1.5.1 Oxidative Pyrolysis.....	13
1.5.2 Well-ventilated Flaming.....	13
1.5.3 Under-ventilated Flaming.....	13

1.5.4 Comparing between Fire Stages	14
1.6 FIRE TOXICITY	15
1.6.1 Determining Toxicity.....	16
1.7 BENCH SCALE TESTS.....	17
1.7.1 Open Tests	17
1.7.1.1 Cone Calorimeter	18
1.7.2 Closed-Box Tests	19
1.7.3 Flow through Tests	20
1.7.3.1 Simple Tube Furnace.....	20
1.7.3.2 Steady State Tube Furnace	20
1.7.4 Micro Scale Tests	21
1.7.4.1 Thermogravimetry	21
1.8 LARGE-SCALE TEST.....	23
1.9 PROBLEMS SCALING FROM BENCH TO LARGE-SCALE TEST.....	24
2. BENCH SCALE INVESTIGATION.....	26
2.1 MATERIALS	26
2.2 STEADY STATE TUBE FURNACE.....	27
2.2.1 Preliminary Work.....	27
2.2.1.1 Air Flow Calibration.....	27
2.2.1.1.1 Calibration Results	29
2.2.1.2 Air flow Validation	30
2.2.1.2.1 Validation Results.....	31
2.2.1.3 Driving Mechanism Speed Calibration	35
2.2.1.3.1 Setting the Driving Mechanism Speed	35
2.2.1.3.2 Driving Mechanism Calibration Results	36
2.2.1.4 Cable Sample Preparation.....	38
2.2.2 Methodology	39
2.2.2.1 Setup and Calibration.....	39
2.2.2.2 Test	41
2.2.2.3 Post-test.....	41
2.2.3 Steady State Tube Furnace Results.....	41
2.2.3.1 Yield Results	43
2.2.3.2 Further CO Analysis.....	46
2.2.3.3 Melos and WLS Repeat Tests.....	49
3 LARGE-SCALE TESTING.....	51

3.1 CALCULATING AVERAGES	51
3.1.1 CO ₂ and CO averages.	51
3.1.2 O ₂ and Smoke averages.	53
3.2 CALCULATING MASS LOSS	54
3.2.1 TGA Based Mass Loss.....	54
3.2.2 CO ₂ Based Mass Loss	55
3.3 CALCULATING YIELDS.....	56
3.4 LARGE-SCALE TEST RESULTS	56
3.4.1 prEN50399-2-1 Results	57
3.4.1.1 1 x 2.5 mm ² LSOH.....	57
3.4.1.2 3 x 1.5 mm ² LSOH	58
3.4.1.3 FR 4804	59
3.4.1.4 Melos 1006F.....	61
3.4.1.5 MGN 09005.....	62
3.4.1.6 WLS 08006	64
3.4.1.7 1 x 25 mm ² PVC.....	65
3.4.2 prEN 50399-2-1 Results Summary	67
3.4.3 TGA	68
3.4.4 TGA Results	68
3.4.4.1 1x2.5 mm ² LSOH.....	68
3.4.4.2 3x1.5 mm ² LSOH:	69
3.4.4.3 FR 4804:	70
3.4.4.4 MGN 09005.....	72
3.4.4.5 Melos 1006F.....	73
3.4.4.6 WLS 08006	73
3.4.4.7 1x25 mm ² PVC.....	74
3.4.5 TGA Summary	75
3.4.6 Burn Length Results	76
3.4.6.1 FR 4804	76
3.4.6.2 Melos 1006F.....	77
3.4.6.3 MGN 09005.....	78
3.4.6.4 WLS 08006	78
3.4.7 Burn Length Summary	79
3.4.8 Estimated Mass Loss in Large-scale Test.	79
3.4.8.1 TGA Based	79
3.4.8.2 CO ₂ Based Mass Loss.....	80
3.4.9 Yield Results.....	81

3.4.9.1 CO ₂ Yields	81
3.4.9.2 CO Yields	82
3.4.9.3 O ₂ Consumed Yields	83
4 COMPARISON OF LARGE AND SMALL-SCALE DATA	85
4.1 EQUIVALENCE RATIO	85
4.1.1 1x2.5 mm ² LSOH	86
4.1.1.1 1 x 2.5 mm ² LSOH Recalculated Yields	87
4.1.2 3x1.5 mm ² LSOH	87
4.1.2.1 3 x 1.5 mm ² LSOH Recalculated Yields	89
4.1.3 FR 4804	90
4.1.4 Melos 1006F	91
4.1.4.1 Melos 1006F Recalculated Yields	92
4.1.5 MGN 09005	93
4.1.5.1 MGN 09005 Recalculated Yields	94
4.1.6 WLS 08006	95
4.1.6.1 WLS 08006 Recalculated Yields	96
4.1.7 1x25mm ² PVC	97
4.1.7.1 1x25mm ² PVC Recalculate Yields	98
4.2 EQUIVALENCE RATIO COMPARISON SUMMARY	98
4.3 EQUIVALENCE RATIO WITH RE-CALCULATED YIELDS COMPARISON SUMMARY	98
4.4 CO/CO ₂ RATIOS	99
4.4.1 1x2.5mm ² LSOH	99
4.4.2 3x1.5mm ² LOSH	101
4.4.3 FR 4804	102
4.4.4 Melos 1006F	103
4.4.5 MGN 09005	104
4.4.6 WLS 08006	105
4.5 CO/CO ₂ RATIO COMPARISON SUMMARY	106
4.6 CO ₂ /CO RATIOS	106
4.7 CO ₂ /CO RATIO COMPARISON SUMMARY	109
4.8 HEAT RELEASE (kW/g)	109
4.8.1 1 x 2.5mm ² LOSH	109
4.8.2 3 x 1.5mm ² LSOH	110
4.8.3 1 x 25mm ² PVC	111
4.8.3 FR 4804	112

4.8.4 Melos 1006F	112
4.8.5 MGN 09005.....	113
4.8.6 WLS 08006	114
4.9 HRR (kW/) COMPARISON SUMMARY	114
4.10 HEAT RELEASE (kJ/g).....	114
4.11 HEAT RELEASE (kJ/g) COMPARISON SUMMARY.....	115
5 COMPARING TOXICITY BETWEEN LSOH AND PVC CABLES	117
6 CONCLUSIONS	119
6.1 COMPARISON OF TOXICITY BETWEEN PVC AND NON-HALOGENATED CABLES.....	119
6.2 COMPARISON OF RESULTS BETWEEN SCALES.....	120
REFERENCE LIST.....	124
Appendix A	1
Appendix B.....	5
Appendix C.....	8
Appendix D	13

List of Tables

Table 1 Chain-reaction and Step-reaction Polymerisation Comparison	5
Table 2 Comparative Temperatures for Different Ignition Modes	11
Table 3 Parameters for Different Fire Stages, based on ISO 19706 ³⁷	14
Table 4 List of Materials	26
Table 5 0.6 – 5 L/min Primary Air Flow Calibration	29
Table 6 2 - 25 L/min Primary Air Flow Calibration	29
Table 7 6 – 50 L/min Secondary Air Flow Calibration	30
Table 8 Mass Flow Controller Validation.....	31
Table 9 Comparison of Measured and Expected O ₂ Results	32
Table 10 0.6 - 5 L/min Calibration Table	33
Table 11 2 - 25 L/min Calibration Table	33
Table 12 6 - 50 L/min Calibration Table	34
Table 13 Setting the Driving Mechanism Speed	35
Table 14 Driving Mechanism Speed Settings.....	36
Table 15 11.6 mm/min Speed Calibration	36
Table 16 23.3 mm/min Speed Calibration	37
Table 17 35.0 mm/min Speed Calibration	37
Table 18 46.6 mm/min Speed Calibration	37
Table 19 Calculating Feed Rate	38
Table 20 List of Small-scale Tests and Conditions used	42
Table 21 Large-scale Results Summary.....	67
Table 22 Percentage Mass Loss of Cable Components	76
Table 23 Large-scale Total Burn Length	79
Table 24 TGA Based Mass Loss Estimation in Large-scale Test.....	80
Table 25 CO ₂ Based Mass Loss Estimation in Large-scale Test	80

List of Figures

Figure 1 Cable Construction	3
Figure 2 Polymer Decomposition: Propagation Steps	8
Figure 3 Polymer Decomposition: Termination Processes	9
Figure 4 Scheme for Auto Ignition (left) and Piloted Ignition (right)	12
Figure 5 Effect of Fire Stage on Toxic Gas Production ⁴⁷	16
Figure 6 Cone Calorimeter Schematic ⁵⁵	19
Figure 7 NFX 70-100 Schematic	20
Figure 8 ISO TS 19700 Schematic	21
Figure 9 TGA Schematic	22
Figure 10 Generic Two Step Decomposition.....	23
Figure 11 prEN 50399-2-1 Schematic	23
Figure 12 Primary Air Flow Calibration Set-up	28
Figure 13 Secondary Air Flow Calibration Set-up	28
Figure 14 N ₂ Validation Results	32
Figure 15 Layout of SSTF Analyser Chain	39
Figure 16 SSTF CO Yields 1	43
Figure 17 SSTF CO Yields 2	43
Figure 18 SSTF CO ₂ Yields.....	44
Figure 19 SSTF O ₂ Consumed	44
Figure 20 SSTF Smoke Extinction Area.....	45
Figure 21 SSTF HCl Yield for 1x25 mm ² PVC.....	45
Figure 22 1x2.5 mm ² LSOH CO (%).....	46
Figure 23 3x1.5 mm ² LSOH CO (%).....	46
Figure 24 Melos CO (%).....	46
Figure 25 MGN CO (%)	46
Figure 26 WLS CO (%)	47
Figure 27 PVC CO (%).....	47
Figure 28 Comparison of CO Yields generated from either the Arithmetic Mean or Integral of the CO data.....	48
Figure 29 Comparison of CO Yields generated from either the Arithmetic Mean or Integral of the CO data (Y-axis has a smaller scale).....	48
Figure 30 Melos Repeat Tests vs. Original Tests CO Yields	49
Figure 31 WLS Repeat Tests vs. Original Tests CO Yields	49
Figure 32 Melos Complete CO Yield Data.....	50
Figure 33 WLS Complete CO Yield Data	50
Figure 34 Calculating CO ₂ Average (%)	52
Figure 35 Calculating CO Average (%).....	52
Figure 36 Calculating O ₂ and Transmission Values (%)	53
Figure 37 Large-scale Measurement Ruler	55
Figure 38 Large-scale Ladder Markings	55
Figure 39 125LSOH Large-scale CO ₂ Data.....	57
Figure 40 125 LSOH Large-scale CO Data	57
Figure 41 125LSOH Large-scale O ₂ Data	57
Figure 42 125LOSH Large-scale Transmission Data	57
Figure 43 315LSOH Large-scale CO ₂ Data.....	58
Figure 44 315LSOH Large-scale CO Data	58
Figure 45 315LSOH Large-scale O ₂ Data	59
Figure 46 315LSOH Large-scale Transmission Data	59
Figure 47 FR 4804 Large-scale CO ₂ Data	59

Figure 48 FR 4804 Large-scale CO Data.....	59
Figure 49 FR 4804 Large-scale O ₂ Data.....	60
Figure 50 FR 4804 Large-scale Transmission Data.....	60
Figure 51 Melos 1006F Large-scale CO ₂ Data	61
Figure 52 Melos 1006 Large-scale CO Data	61
Figure 53 Melos 1006F Large-scale O ₂ Data.....	62
Figure 54 Melos 1006F Large-scale Transmission Data	62
Figure 55 MGN 09005 Large-scale CO ₂ Data.....	62
Figure 56 MGN 09005 Large-scale CO Data	62
Figure 57 MGN 09005 Large-scale O ₂ Data.....	63
Figure 58 MGN 09005 Large-scale Transmission Data	63
Figure 59 WLS 08006 Large-scale CO ₂ Data.....	64
Figure 60 WLS 08006 Large-scale CO Data	64
Figure 61 WLS 08006 Large-scale O ₂ Data	64
Figure 62 WLS 08006 Large-scale Transmission Data.....	64
Figure 63 125PVC Large-scale CO ₂ Data.....	65
Figure 64 125PVC Large-scale CO Data.....	65
Figure 65 125PVC Large-scale O ₂ Data	66
Figure 66 125PVC Large-scale Transmission Data.....	66
Figure 67 125LSOH TGA Data	69
Figure 68 315LSOH TGA Data	70
Figure 69 FR 4804 TGA Data.....	71
Figure 70 MGN 09005 TGA Data	72
Figure 71 Melos 1006F TGA Data	73
Figure 72 WLS 08006 TGA Data	74
Figure 73 125PVC TGA Data.....	75
Figure 74 FR 4804 Large-scale Test Photo	77
Figure 75 Melos 1006F Large-scale Photo	78
Figure 76 MGN 09005 Large-scale Photo.....	78
Figure 77 WLS 08006 Large-scale Photo.....	79
Figure 78 Large-scale CO ₂ Yields	81
Figure 79 Large-scale CO Yields.....	82
Figure 80 Large-scale O ₂ Consumption.....	83
Figure 81 125LSOH CO ₂ Comparison	86
Figure 82 125LSOH 125 CO Comparison.....	86
Figure 83 125LSOH O ₂ Comparison	86
Figure 84 125 LSOH Recalculated CO Yield Comparison	87
Figure 85 315LSOH Original 3 Tests Comparison	88
Figure 86 315LSOH CO ₂ Comparison	88
Figure 87 315LSOH CO Comparison.....	88
Figure 88 315LSOH O ₂ Comparison	89
Figure 89 315LSOH Recalculated CO Yield Comparison	90
Figure 90 FR 4804 CO ₂ Comparison.....	90
Figure 91 FR 4804 CO Comparison	90
Figure 92 FR 4804 O ₂ Comparison.....	91
Figure 93 Melos 1006F CO ₂ Comparison.....	91
Figure 94 Melos 1006F CO Comparison.....	91
Figure 95 Melos 1006F O ₂ Comparison.....	92
Figure 96 Melos 1006F Recalculated CO Yield Comparison	93
Figure 97 MGN 09005 CO ₂ Comparison.....	93

Figure 98 MGN 09005 CO Comparison	93
Figure 99 MGN 09005 O2 Comparison	94
Figure 100 MGN 09005 Recalculated CO Yield Comparison	95
Figure 101 WLS 08006 CO ₂ Comparison	95
Figure 102 WLS 08006 CO Comparison.....	95
Figure 103 WLS 08006 O ₂ Comparison	96
Figure 104 WLS 08006 Recalculated CO Yield Comparison	96
Figure 105 125 PVC CO ₂ Comparison	97
Figure 106 125 PVC CO Comparison	97
Figure 107 125 PVC O2 Comparison	97
Figure 108 125 PVC CO Yield Comparison	98
Figure 109 125LSOH CO/CO ₂ Ratio.....	100
Figure 110 125LSOH CO ₂ and CO Data	100
Figure 111 125 LSOH CO ₂ , CO and Modified CO Data.....	100
Figure 112 125LSOH Modified CO/CO ₂ Ratio.....	101
Figure 113 315LSOH CO/CO ₂ Ratio	102
Figure 114 FR 4804 CO/CO ₂ Ratio	103
Figure 115 Melos 1006F CO/CO ₂ Ratio.....	104
Figure 116 MGN 09005 CO/CO ₂ Ratio.....	105
Figure 117 WLS 08006 CO/CO ₂ Ratio.....	106
Figure 118 125LSOH CO ₂ /CO Ratio.....	107
Figure 119 315LSOH CO ₂ /CO Ratio.....	107
Figure 120 FR 4804 CO ₂ /CO Ratio	107
Figure 121 Melos 1006F CO ₂ /CO Ratio.....	107
Figure 122 MGN 09005 CO ₂ /CO Ratio.....	107
Figure 123 WLS 08006 CO ₂ /CO Ratio.....	107
Figure 124 125LOSH 2 CO ₂ and CO Data	108
Figure 125 315LSOH 3 CO ₂ and CO Data	108
Figure 126 315LSOH 4 CO ₂ and CO Data	108
Figure 127 Melos 2 CO ₂ and CO Data.....	108
Figure 128 315LSOH 10 Point Moving Average	108
Figure 129 WLS 08006 10 Point Moving Average	108
Figure 130 125LSOH Heat Release Rate.....	110
Figure 131 315LSOH Heat Release Rate.....	111
Figure 132 125PVC Heat Release Rate	111
Figure 133 FR 4804 Heat Release Rate	112
Figure 134 Melos 1006F Heat Release Rate.....	113
Figure 135 MGN 09005 Heat Release Rate.....	113
Figure 136 WLS 08006 Heat Release Rate.....	114
Figure 137 Heat Release Rate (kJ/g).....	115
Figure 138 FED Results	117

Acknowledgements

I would like to thank my two supervisors: Dr Anna Stec and Professor Richard Hull for their time, guidance and support throughout the undertaking of this project.

I would like to thank Borealis and The European Association of Producers of Flame Retardant Olefinic Cable Compounds (FROCC) for the financial support, as well as the supply of materials that enabled me to undertake this research project.

I would also like to thank Steve Harris for his technical help and advice, along with Sal Tracey, Mick Ward, James Hewell, Jim Donnelly and Tamar Garcia-Sorribes for their help, advice and loaning of equipment.

My thanks also go to my friends and colleagues: Jen Rhodes, Parina Patel, Artur Witkowska, Adam May, David Kind, and Luke Hollingbery

Finally my thanks must go to my good friends and family who have been incredibly patient and supportive during my research.

List of Abbreviations and Terms

Cable Materials:

- LSOH refers to Low Smoke Zero Halogen cable composition
- 1x2.5 mm² LSOH may be referred to as 125LSOH
- 3x1.5 mm² LSOH may be referred to as 315LSOH
- FR4804 may be referred to as FR
- Melos 1006 ATH may be referred to as Melos 1006 or Melos
- MGN 09005 may be referred to as MGN
- WLS 08006 may be referred to as WLS
- 1x25 mm² PVC may be referred to as 125PVC

Test Methods

- Steady State Tube Furnace may be referred to as SSTF
- Thermogravimetric Analysis may be referred to as TGA or TG

Terms

- ϕ refers may be referred to as equivalence ratio, or phi
- Oxidative pyrolysis may be referred to as smouldering, or non-flaming combustion
- Well-ventilated may be referred to as a developing flaming fire or open ventilation
- Under-ventilated may be referred to as less well-ventilated, vitiated or restricted ventilation

Aims and Objectives.

This study aims to correlate combustion toxicity data of cables between the bench-scale and the large-scale. The test apparatus used at the bench-scale was the

steady state tube furnace (ISO TS 19700) the large-scale test used is the prEN 50399.

In order to correlate the data, it first had to be decided what species were to be used to for the comparison. For the bench to large-scale comparison it was decided that to keep any potential sources of error to a minimum the species to be compared were CO₂, CO, O₂ depletion and smoke (transmission).

The raw data from both scales had to be manipulated such that they could be compared. It was decided that the best way to compare the data would be to express the results in terms of yields (g/g). However this meant that for each large-scale test the mass loss had to be estimated, which was done from photographic observations of the large-scale test, and data from thermogravimetric analysis (TG or TGA) experiments carried out on each cable material

To help establish a correlation the bench-scale tests of each cable were carried out at a range of different ventilation conditions to compare against the large-scale data (of unknown ventilation condition)

The collected data also allowed for a comparison of the combustion toxicity of different cable types in the steady state tube furnace as a function of ventilation conditions, and for a comparison of PVC cable and non-halogenated cable combustion toxicity. The toxicity was assessed using Fractional Effective Dose (FED), and used both the Purser and NIST model.

1. INTRODUCTION

1.1 CABLES

There are many different types of cable, often dependent on their end use. Cables may be defined by the number of conductors they contain: single-core only contain one conductor surrounded by an insulating sheath or multi-core contain multiple conductors, each surrounded by their own insulating material, which are encapsulated by a insulating sheath, sometimes with a bedding material in between¹(Figure 1).

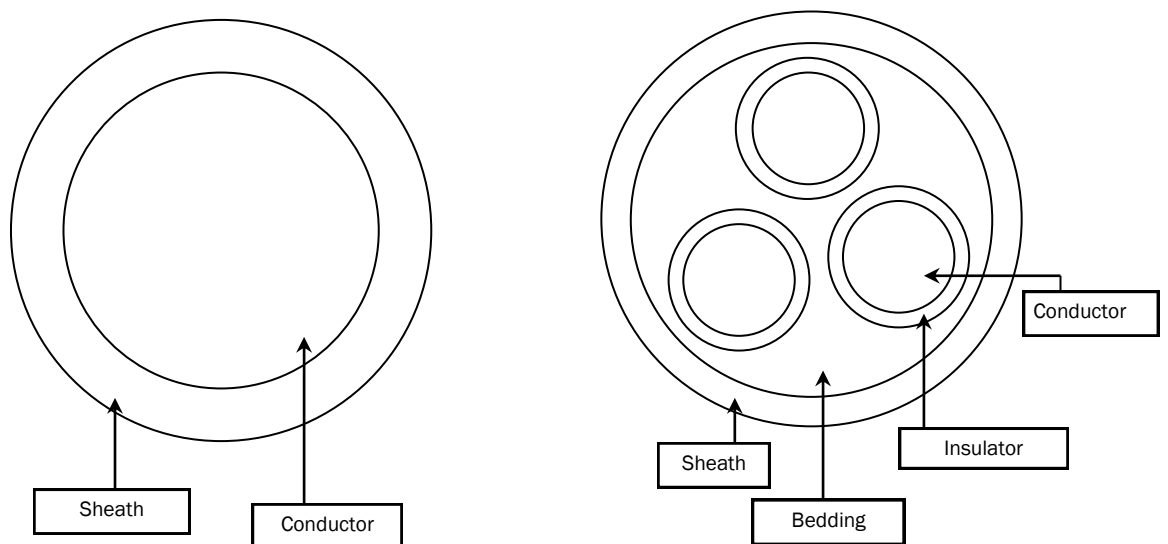


Figure 1 Cable Construction

A Single Core Cable (left) and a Multi core Cable (right)

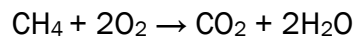
This category can be divided further, based on the material used in the sheath. Traditionally the first division would be whether the sheath is made from a natural or synthetic material; however in modern wiring natural materials have been replaced with synthetic polymers². The next division would be based on the synthetic polymer used in the insulation, whilst the number of formulations possible for synthetic insulation is extensive, synthetic cable materials can be divided into one of two generic categories: halogenated, containing chlorine, bromine or fluorine, and non-halogenated. Poly(vinyl chloride), PVC, is still the dominant

material used for insulating cables¹, accounting for approximately 2/3 of the insulation used in the United States³. PVC is less flammable than hydrocarbon polymers, has low water absorption, good adhesion and oil resistance, good electric strength at low voltages, and is compatible with a large number of plasticisers and other polymers⁴. However, as studies show, the fire toxicity of PVC cables is much greater than their non-halogenated counterparts⁵, so the demand for non-halogenated products is likely to increase.

Cables and their reaction to fire is of interest due to the almost unique type of fire hazard they present, which is a direct result of where they are located within a building. Cables are often located in remote areas, and often within concealed ducts or air passages that circumvent the existing fire compartments. The remoteness allows a fire to progress significantly before becoming evident to the inhabitants, whilst the circumvention of fire compartments allows the fire to spread quickly through the building⁶.

1.2 FREE RADICAL REACTIONS

Whilst the equation:

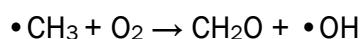


is an accurate representation of a combustion reaction involving methane, it masks the true complexity of chemical processes that take place during the reaction. These processes involve highly reactive molecular fragments (atoms and free-radicals), such as $\text{H}\cdot$, $\cdot\text{OH}$ and $\cdot\text{CH}_3$ ⁷. This radical chain reaction can be separated into three separate stages: initiation, propagation and termination.

Initiation is the step in which the first chain carriers (radicals) are formed, either by a thermolysis or photolysis reaction⁸, where M represents an interacting species.



Propagation is a reaction where the number of free radicals is maintained:



Termination is a reaction where the number of free radicals is reduced via the combination of radicals:



The complexity of these free-radical reactions increases as the size and structure of the fuel molecule increases leading to a much larger number of oxidised species potentially being produced⁹.

1.3 POLYMERS

A polymer is a chain molecule consisting of repeating sub-units known as monomers. There are hundreds of different types of polymers, both natural and synthetic, and the chains may be linear: where the chain is straight; branched: where the chain splits (branches); or cross-linked where bonds are formed between two adjacent polymer chains.

1.3.1 Polymer Synthesis

Polymers are formed by a process of polymerisation. There are two main types of polymerisation: chain-reaction polymerisation and step-reaction polymerisation. A summary of the differences in the two types can be seen in [Table 1](#)¹⁰.

Table 1 Chain-reaction and Step-reaction Polymerisation Comparison

Step Reaction	Chain Reaction
Growth occurs throughout matrix by reaction between monomers, oligomers, and polymers	Growth occurs by successive addition of monomer units to limited number of growing chains
Average degree of polymerisation low to moderate	Average degree of polymerisation can be very high
Monomer consumed rapidly while molecular weight increases slowly	Monomer consumed relatively slowly, but molecular weight increases rapidly
No initiator needed; same reaction mechanism throughout	Initiation and propagation mechanisms different
No termination step; end groups still reactive	Usually chain-terminating step involved
Polymerization rate decreases steadily as functional groups consumed	Polymerisation rate increases initially as initiator units generated; remains relatively constant until monomer depleted.

1.3.1.1 Chain-reaction Polymerisation

The process involves rapid radical chain reactions (Section 1.2) to form the polymer chain¹¹; as such the process involves initiation, propagation and termination steps¹². There are two types of chain reaction mechanism, depending on the initiating species. Anionic chain reactions use initiators that are generators of anions. Cationic chain reactions use initiators that are generators of cations. In both cases an activated monomer reacts very rapidly with successive monomers, forming a long chain very quickly. The formation of polyvinyl chloride (PVC) occurs via chain-reaction polymerisation¹³, as does low-density polyethylene (LDPE) and ethylene vinyl acetate copolymer (EVA) .

1.3.1.2 Step-reaction Polymerisation

The process is fundamentally different to chain-reaction polymerisation as it comprises the sequential coupling of monomeric, dimeric, trimeric units¹⁴, which eventually gives rise to polymer chains with a high molar mass, whereas the chain-reaction process only involves monomers. This process is slower than the chain reaction polymerisation as initially only dimers will be produced in large quantities, towards the end of the reaction the dimers start to react, producing trimers, tetramers etc. Overall this means that long chain polymers are only created very late in the reaction process¹³.

1.3.2 Polymer Decomposition

Thermal decomposition is “a process of extensive chemical species change caused by heat” ¹⁵. Thermal decomposition can also involve oxidative processes, however those involving oxidation are often accelerated and as such the minimum decomposition temperature when an oxidant is involved is much less than a non-oxidative mechanism¹⁷. Whilst the chemical processes that result in the formation of volatiles during thermal decomposition are important, the physical changes that occur concurrently with them are just as important. It is these physical changes that can alter the decomposition and burning characteristics of the decomposing polymer.

1.3.2.1 Physical Changes

The two potential physical changes are melting and charring. Char, whilst formed by a chemical process, is of importance due to its physical properties¹⁸. Char is a low-density, porous material, which ideally prevents the progression of volatiles from the surface of the polymer to the reaction zone, and shields the surface of the polymer from the heat flux being generated by the reaction zone, keeping the remaining polymer below its decomposition temperature¹⁹. Melting, often manifesting as dripping, can have either a positive or negative effect on the materials fire performance, dependent on its orientation. If the material starts to move, or drip, away from the heat source, combustible material is being removed²⁰. However if material starts to flow towards the heat source then combustible material is being introduced at a quicker rate. Another negative effect is the occurrence of flaming drips, which allows a downward spread of flame²¹ not normally possible, as can occur within the large-scale test, causing difficulties with accurate mass-loss calculations as described in [Section 1.9](#).

1.3.2.2 Chemical Changes

There are four general classes of mechanisms associated with thermal decomposition¹⁸:

- Random Chain Scission
- End Chain Scission
- Chain Stripping
- Cross Linking

These can be grouped according to whether the reactions occurring involve the main polymer chain, or the functional groups attached. Both of the chain scission mechanisms and cross-linking affect the main polymer chain, whilst the remaining chain stripping only affects the side groups^{18,22}. Both random and end chain scission of many chain polymerised polymers rely on free radical reactions ([Section 1.2](#)).

1.3.2.2.1 Main Chain Mechanisms

1.3.2.2.1.1 Cross Linking

Cross-linking often occurs after some of the functional groups have been eliminated from the main chain, and comprises of the formation of a bond between two polymer chains. The resulting molecule is of higher molecular weight, and is less easily volatilised, thus cross-linking is an important mechanism in the formation of char¹⁸. Cross-linking is also part of the fire-retardant mechanism employed by FR 4804 cable⁹.

1.3.2.2.1.3 Chain Scission

Chain scission is the most common main chain mechanism and can be one of two types: end-chain scission or random-chain scission¹⁸.

The chain scission mechanism is a free radical reaction involving initiation, propagation and termination processes. Both random and end chain scission are involved in the initiation stage. Both result in the formation of free radicals, but as their name suggests random chain scission involves the breaking of a bond in a random place along the main chain, whereas end chain scission involves the breaking of a bond at the end of the main chain¹⁵. The propagation stage consists of three main types of process, depicted in [Figure 2](#).

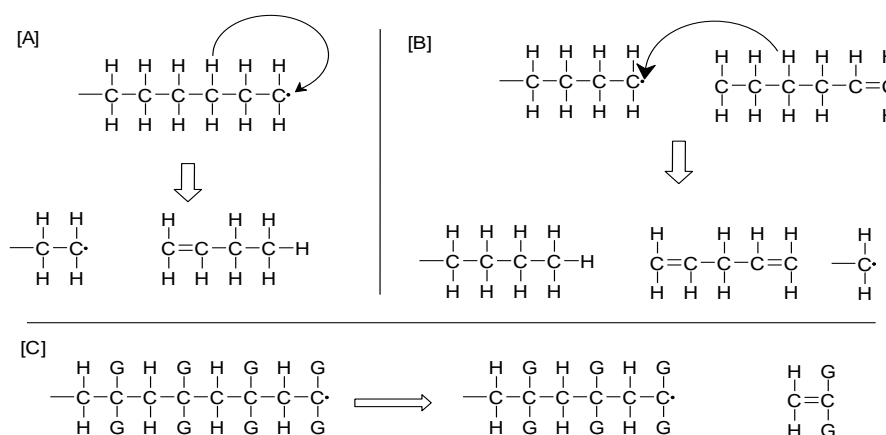


Figure 2 Polymer Decomposition: Propagation Steps

[A] Intra-molecular H Transfer, [B] Inter-molecular H Transfer, [C] Unzipping

(Where G represents any functional group)

Intra-molecular H transfer involves the transfer of a hydrogen atom to an adjacent free radical site within the polymer chain. Whilst adjacent in space the hydrogen atom can be up to four monomer units away, due to the conformation of the polymer¹⁸. Inter-molecular H transfer involves a hydrogen transfer between polymers. The initial free radical removes a hydrogen atom, usually mid-chain, forming a new radical that subsequently breaks up into an unsaturated hydrocarbon and a radical¹⁸. End chain scission, or unzipping, involves no transferring of hydrogen, but is the reverse process of polymerisation, with a radical breaking down to form a radical and a smaller hydrocarbon.

The final stage is termination (Figure 3), of which there are 3 types; unimolecular termination, recombination and disproportionation. The first type of which is generally not possible, as it involves removing a radical site without the adding or removing of a hydrogen atom, whilst still satisfying the valence requirements of the atoms. Recombination is a highly common mechanism by which termination is accomplished, and involves two radicals combining to form a polymer. Disproportionation involves two radicals forming two polymers by the process of one radical donating a hydrogen atom to the other, forming a fully saturated polymer and an unsaturated polymer¹⁵.

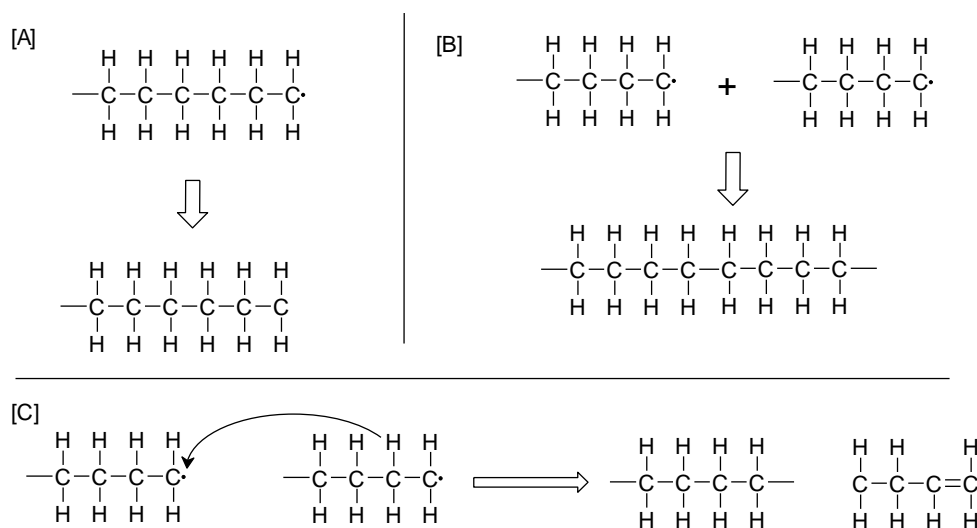


Figure 3 Polymer Decomposition: Termination Processes

[A] Unimolecular termination, [B] Recombination, [C] Disproportionation

1.3.2.2.2 Side Chain Mechanisms

Chain stripping involves the loss of small molecules generated by reactions that strip the main chain of its side groups and form small molecules. Chain stripping occurs via one of two main reaction types: side chain elimination or side chain cyclisation⁹.

1.3.2.2.2.1 Side Chain Elimination

Side chain elimination involves the breaking of the bond between the functional group and the main polymer chain. The eliminated group often reacts with other eliminated functional groups and are often of a small enough size to be considered volatile¹⁸.

1.3.2.2.2.2 Side Chain Cyclisation

Side-chain cyclisation occurs when two functional groups which are adjacent react such that a bond is formed resulting in a cyclic structure. This mechanism is important to char formation, due to the cyclic nature of the resulting group, and the residue being much richer in carbon than prior to the reaction¹⁵. This mechanism is the manner by which PVC decomposes to leave a hydrogenated char¹⁸.

1.4. IGNITION

In order for a flaming fire to start the pyrolysis products need to be ignited. Ignition is defined as the process by which a rapid, exothermic reaction is initiated, which then propagates and causes the material involved to undergo change, producing temperatures greatly in excess of ambient²³. There are two main forms of ignition: Piloted Ignition and Auto-ignition, both of which occur in the steady state tube furnace ([Section 1.7.3.3](#)).

1.4.1 Piloted Ignition

Piloted ignition is where the mixture of gaseous volatiles is ignited by an external source, different to the radiant heat flux responsible for the pyrolysis; it can be in the form of a hot-spot, spark or small flame²⁴. In order for sustained piloted

ignition to occur, the mass of fuel vapours must be in excess of the critical mass flux. However there is an exception to this rule, dependent on the source of the heat flux. If the heat flux responsible for generating the pyrolysis products is in the form of a pulse the sustainability of a flame is determined by the heat losses from the flame to the solid's surface, and the rate of heat loss from the surface of the material²⁵ (Figure 4).

1.4.2 Auto-ignition

Auto-ignition by contrast is the ignition of the fuel vapours in the absence of a pilot source. It occurs when somewhere within the plume the volatile air mixture reaches a sufficiently high temperature²⁶, usually due to an increase in the number of exothermic, non-flaming oxidation reactions. As with piloted ignition the mass of fuel vapours must be in excess of the critical value, and the heat flux from the flame back to the surface of the solid must be sufficient to continue the pyrolysis process (Figure 4).

It has been shown, using wood, that the temperatures required for auto-ignition are higher than those required for piloted ignition (Table 2)²⁶.

Table 2 Comparative Temperatures for Different Ignition Modes

Mode of Heat Transfer	Surface Temperature of wood for:	
	Auto Ignition	Piloted Ignition
Radiation	600 °C	300-410 °C
Convection	490 °C	450 °C

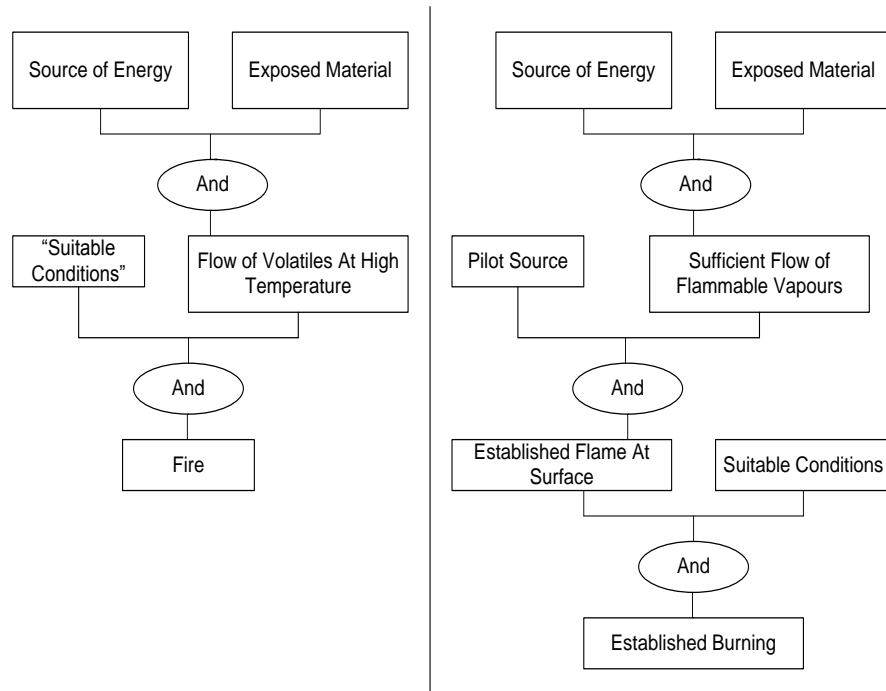


Figure 4 Scheme for Auto Ignition (left) and Piloted Ignition (right)

1.5 FIRE

Fire can be defined as a chemical reaction that involves a combustible species and an oxidising agent²⁷, usually air, which is not particularly useful, thus an alternate, more useful definition has been recorded: “an uncontrolled chemical reaction producing light and energy sufficient to damage the skin”²⁸.

A fire has been recognised to pass through different stages⁹. According to ISO 19706 three of the most important stages are considered to be:

- Non-flaming
 - ◆ Smouldering
 - ◆ Oxidative pyrolysis from externally applied radiation
 - ◆ Anaerobic pyrolysis from externally applied radiation
- Well-ventilated Flaming
- Under-ventilated Flaming
 - ◆ Small localised fire, generally in a poorly ventilated compartment
 - ◆ Post-flashover fire

1.5.1 Oxidative Pyrolysis

Material in the solid phase can only burn by smouldering. Only materials in the gas phase burn with flames. As such a solid fuel must undergo thermal degradation to be changed into the gaseous phase. Oxidative pyrolysis is a complicated process, the mechanisms of which are the same as thermal decomposition in the presence of an oxidant as discussed in [Section 1.3.2](#).

1.5.2 Well-ventilated Flaming

For a fire to develop, two conditions must be satisfied; the concentration of volatiles at the surface of the solid should be greater than the lower flammability limit in order to allow a flame to develop, and the heat flux back to the solid from the flame should be sufficient to sustain the pyrolysis process such that the flame is not starved of fuel. A developing flaming fire is often unaffected by the enclosure in which it starts and is said to be fuel-controlled³⁰. The growth rate of a developing flaming fire is often rapid, as the flame spreads across the fuel source. It is dependent on access to oxygen and other fuel sources, if there is plenty of fuel in close proximity and sufficient oxygen to support well-ventilated flaming then the growth can be swift³⁰. If a fire proceeds and continues to grow it may eventually reach a state of flashover, whereby all of the fuel available in the compartment becomes involved³¹. As the ventilation becomes limited then the fire is termed ventilation controlled³².

1.5.3 Under-ventilated Flaming

If a fire occurs in a closed compartment it will reach a point where the growth of the fire has consumed most of the available oxygen in the compartment³³. The oxygen being entrained into the combustion zone is often minimal due to the hot layer descending below the flame region, which may lead to the fire extinguishing due to oxygen starvation³⁰. This stage of fire growth is the most dangerous in terms of toxicological effects³⁴, as the high temperatures drive forward combustion reactions in the absence of adequate oxygen forming incomplete-combustion products.

1.5.4 Comparing between Fire Stages

In order to compare these stages between different experiments, such as would be necessary when comparing across different scales of testing, more stringent, scientific parameters have been established as shown in Table 3. Of these methods of classifying fire stages, extensive work by Pitts³⁵ has shown the importance of the equivalence ratio (ϕ) in defining fire stages.

$$\phi = \frac{\text{Actual Fuel/Air Ratio}}{\text{Stoichiometric Fuel/Air Ratio}}$$

Equation 1 Equivalence Ratio

Actual fuel/air ratio is measured during the test run and is a measure of the mass of fuel consumed during the test divided by the mass of oxygen present to support combustion. The stoichiometric fuel/air ratio is the mass of fuel consumed during the test divided by the mass of oxygen that would be required for complete combustion. ISO 19703³⁶ details multiple methods for determining ϕ , including guidance for calculating ϕ dependent on what class of test apparatus is being used (Section 1.7).

Table 3 Parameters for Different Fire Stages, based on ISO 19706³⁷

Fire Stage	Heat /kW m ⁻²	Max Temp / °C		Oxygen %		Equiv- alence ratio ϕ	$\frac{V_{CO}}{V_{CO_2}}$	Comb- ustion Efficiency %
		Fuel	Smoke	In	Out			
Non-flaming								
1a. Self sustained smouldering	n.a.	450 - 800	25 - 85	20	0 - 20	-	0.1 - 1	50-90
1b. Oxidative, external radiation	-	300 - 600		20	20	-		
1c. Anaerobic external radiation	-	100 - 500		0	0	-		
Well-ventilated flaming								
2. Well-ventilated flaming	0 to 60	350 - 650	50 - 500	~20	0 - 20	<1	<0.05	>95
Under-ventilated Flaming								
3a. Low vent. room fire	0 to 30	300 - 600	50-500	15 - 20	5 - 10	> 1	0.2 - 0.4	70 - 80
3b. Post flashover	50 to 150	350 - 650	>600	<15	<5	> 1	0.1 - 0.4	70 - 90

1.6 FIRE TOXICITY

Fire toxicity has long been considered the major cause of deaths in fires³⁸, yet outside of the mass transport sector only China and Japan have integrated fire toxicity testing as part of the construction product requirements³⁹. Within the United Kingdom between 1996 and 2006, 40% of all fire deaths were attributed to people being overcome by gas or smoke, with another 20% being attributed to burns and overcome by gas or smoke³⁸. Carbon monoxide is considered to be the most toxicologically significant component in fire gases⁴⁰, but other gases within the effluent also contribute: such as CO₂ which causes hyperventilation, resulting in greater volumes of effluent to be inhaled; HCl, an irritant which, amongst others, attacks the eyes, causing a person to become disorientated and preventing their escape from a fire. A list of the most important fire gases is given in ISO 13344⁴¹. HCl is of particular importance concerning cable fires as PVC, from which HCl is evolved during combustion, is the primary polymer used for cable insulation¹.

Fire toxicity is not only dependent on the composition of the polymer, but also on the fire scenario itself⁴². Well-ventilated fires occur in an excess of oxygen allowing complete combustion, the main products of which are CO₂ and H₂O, along with low yields of all carbon and nitrogen based toxic compounds, with the exception of nitrogen oxides (NO)_x⁴³. However recent research has shown that in some cases the contributions of isocyanates and HCN to the toxicity of a fire gas need to be considered⁴⁴. Materials containing halogens also generate higher yields of toxic species than would be expected under well-ventilated conditions, due to their gas phase interactions that result in inefficient combustion, increasing the yield of toxic carbon and nitrogen compounds⁴⁵. Under-ventilated fires occur in oxygen depleted environments thus combustion is incomplete and the yields of toxic products such as CO, organic irritants and phenols are much higher⁴⁶. [Figure 5](#) illustrates the differences that each fire stage has on toxic gas production; non-flaming is equivalent to oxidative pyrolysis, open ventilation is the same as well-ventilated flaming and restricted ventilation is akin to under-ventilated flaming.

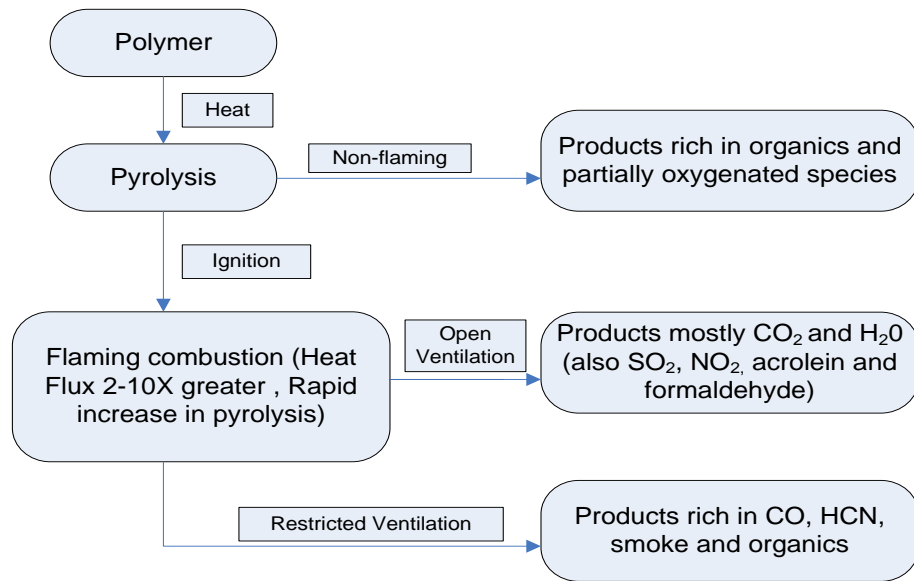


Figure 5 Effect of Fire Stage on Toxic Gas Production⁴⁷

1.6.1 Determining Toxicity

When only one toxicant is being considered the method by which its toxicity is assessed is its LC₅₀ value. LC₅₀ is the concentration of a toxicant at which 50% of test subjects exposed die, within a specified exposure, and post-exposure time⁴¹.

If more than one toxicant is being considered then additive behaviour of individual toxicants is generally assumed⁴⁸. The method by which they are assessed is fractional effective dose (FED). If the FED value is equal or greater than 1 then the combination of toxicants is deemed to be fatal to 50% of the population⁴⁹.

There are two FED related equations that can be used. The N-Gas model, and the Purser model. The difference being the N-Gas model assumes that only the main toxicant, CO, is affected by the increase of respiration rate caused by high CO₂ concentrations, whereas the Purser model utilises a multiplication factor for the increase in respiration rate due to CO₂ that is applied to all the toxic species being considered⁴⁰.

$$FED = \frac{m[CO]}{[CO_2] - b} + \frac{[HCN]}{LC_{50}(HCN)} + \frac{21 - [O_2]}{21 - LC_{50}(O_2)} + \frac{[HCl]}{LC_{50}(HCl)} + \frac{[HBr]}{LC_{50}(HBr)}$$

Equation 2 N-Gas FED Model

In Equation 2 the square brackets indicate fire effluent concentrations (%), whilst the LC₅₀ values are for a 30 minute exposure period and a 14 day post exposure

period. The constants m and b refer to slope and intercept, respectively of the fitted curve depicting the interaction between CO and CO₂⁵⁰. More gases can be added as required.

$$FED = \left(\frac{[CO]}{LC_{50,CO}} + \frac{[CN]}{LC_{50,HCN}} + \frac{[X]}{LC_{50,X}} + \frac{[Y]}{LC_{50,Y}} \right) \times V_{CO_2} + Z_A + \frac{21 - [O_2]}{21 - 5.4}$$

Equation 3 Purser FED Model

In Equation 3 [CO] is the CO concentration, expressed in percent by volume; [CN] is the HCN concentration in microlitres per litre, corrected for the presence of other nitriles and the protective effect of NO₂; [X] and [Y] are concentrations in microlitres per litre, of each acid gas and organic irritant respectively; LC_{50,CO}, LC_{50,HCN}, LC_{50,X}, and LC_{50,Y} are the LC₅₀ concentrations, expressed in microlitres per litre, for CO, HCN, each acid gas, and each organic irritant respectively. V_{CO2} is the multiplication factor for CO₂ driven hyperventilation; Z_A is the acidosis factor; and [O₂] is the concentration of oxygen, expressed in microlitres per litre⁵⁰.

1.7 BENCH SCALE TESTS

Bench scale testing is preferable to large-scale testing as they are more easily replicated, more reproducible and much less expensive than their larger counterparts²⁰. However the value of bench scale toxicity assessment is dependent on its ability to accurately replicate the large-scale test²⁰. For toxicity assessment there are a number of bench scale methods available, of the standard methods used there are three general groups: well-ventilated or open tests, closed-box and flow through or tube furnace tests⁴⁰.

1.7.1 Open Tests

Open tests account for the majority of bench-scale fire tests, such as ISO 5660^{51,52} Cone Calorimeter, however whilst being the main type of bench scale tests, open tests are generally unsuitable for use in toxic product yield estimation. This is because the results from toxicity testing using an open test method can be

misleading: open test methods are well-ventilated and it is this high degree of ventilation coupled with the resultant rapid quenching of the fire gases that gives a high yield of incomplete combustion products through premature flame quenching rather than through vitiation⁵³.

1.7.1.1 Cone Calorimeter

The cone calorimeter was originally designed as a measure of heat release and effective heat of combustion for building materials: ISO 5660-1⁵². It was later adapted⁴⁰ such that the cone could provide data on smoke generation, CO and CO₂ yields (ISO 5660-2⁵¹). The specimen being tested can be mounted in either a horizontal or vertical orientation, but must be 10 cm x 10 cm and no thicker than 50mm⁹. The sample is placed on a load cell and zeroed, such that mass loss can be measured continuously throughout the test. The sample is mounted in such a way that only one surface is exposed to the conical radiator, which can be set from 10 – 100 kW/m². In order to ignite the pyrolysis products a spark igniter is used⁹. The smoke and gases produced are removed through an exhaust hood into exhaust ducting where a sample of effluent is cooled, to remove water, and analysed using a paramagnetic O₂ analyser and NDIR CO and CO₂ analysers, which are required by the ISO 5660 standard to ensure the accuracy of the oxygen depletion calorimetry. Heat release is determined through oxygen depletion calorimetry rather than using temperature measurements. Whilst the cone calorimeter is capable of calculation yields for CO and CO₂ its drawback, in terms of toxicity assessment, is that it is only capable of replicating well-ventilated fire stages⁵⁴. Experiments trying to replicate vitiated conditions have been carried out, but have met with limited success⁴⁰.

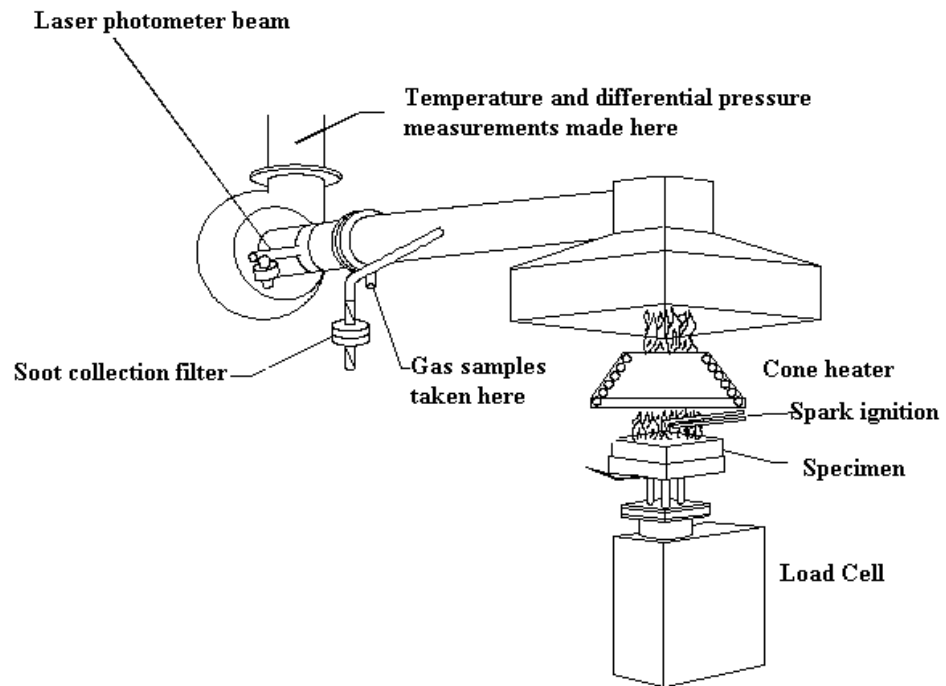


Figure 6 Cone Calorimeter Schematic⁵⁵

1.7.2 Closed-Box Tests

Closed cabinet tests involve a sample being decomposed by a heat source and the effluent generated accumulating within the cabinet⁴⁰. With the effluent being accumulated the resulting gas analysis will give a complete product yield from well-ventilated conditions through to under-ventilated conditions, but with no indication of how toxic yields vary with fire conditions. If there are no mixing fans used during the test then the effluent may become stratified, which if occurs means any sampling of gases carried out is unrepresentative⁴⁰. On the other hand if fans are used, providing an effluent that is uniformly distributed, then the gas flowing into the fire zone may well contain recycled fire gases, altering the toxic product yields. Another potential source of error is the deposition of “stickier” components of the fire effluent, such as HCl, onto the walls of the test cabinet⁵³.

1.7.3 Flow through Tests

Flow through tests involve the sample being thermally decomposed, with or without flaming, in a furnace with air flowing over the sample driving the effluent to the gas determining or sampling systems. There are two kinds of flow-through tests: simple tube furnaces, and the steady state tube furnace.

1.7.3.1 Simple Tube Furnace

The Simple Tube Furnace, NF X 70-100⁵⁶, is a bench scale method created to assess the toxicity of materials used in railway vehicles, initially in France. A sample is placed into a crucible and pushed into the middle of the furnace, where it will thermally decompose. Samples are typically 1 g, or 0.1 g, for low density materials. The sample can be decomposed at a range of temperatures, commonly one of either 400°C, 600°C or 800°C. Air is introduced from one end of the furnace at 2 lmin⁻¹, passing over the sample; the fire gases are passed through detection systems or collected in bubblers for off-line analysis, such as spectrophotometry and chromatographic methods¹⁷. The test method is relatively simple to use, with simple equipment and specified operating conditions. However its main limitation is the need for repeat tests to generate a full gas analysis of a sample⁴⁰.

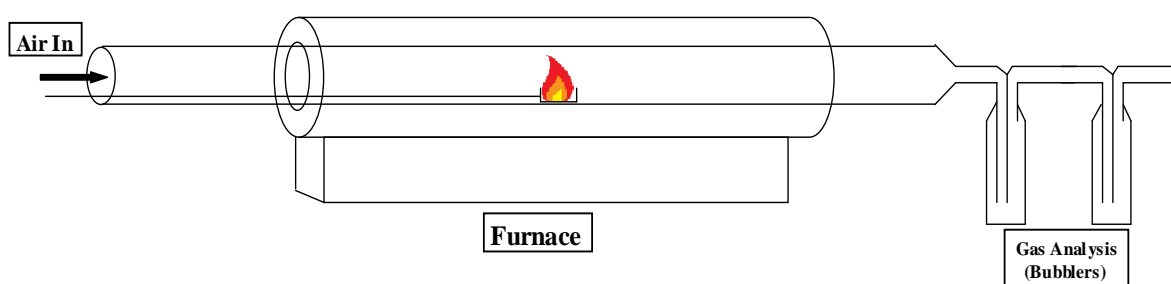


Figure 7 NFX 70-100 Schematic

1.7.3.2 Steady State Tube Furnace

The Steady State Tube Furnace (SSTF, ISO TS 19700³⁷, BS 7990⁵⁷), is a bench scale method designed to assess the toxicity of materials. Its main advantage over other toxicity tests is its ability to closely replicate the conditions of each ISO defined fire stage⁴² (Section 1.5.4). It can achieve this through its

controllable furnace temperature, as well as its controllable primary and secondary air flows. The ability to custom-set the air flows for each test allows the ϕ (Section 1.5.4) to be controlled. The Steady State Tube Furnace is also able to test a variety of different materials due to its variable driving mechanism and “variable” heat flux. This allows both flammable and less flammable materials to be tested. As the sample is driven into the increasing heat flux it will reach the point where the heat flux is enough to support auto ignition; the resultant flame then impinges on the sample directly behind it, acting as a pilot flame for further piloted ignition. The flame then propagates backwards along the sample until it stabilises, which becomes the start of the steady state period. The driving mechanism allows control of the rate at which the sample is moved into the furnace, meaning that a dense material fed at a slower speed can be compared to a less dense material fed in at a faster speed. The toxicity analysis is carried out by chemical analysis, with CO₂, CO and O₂ analysers in-line, and smoke using optical density performed by a horizontally mounted laser in the mixing chamber. Analysis of other species, such as HCl, HCN, NO_x can be carried out by drawing effluent through bubbler solutions and performing analyses off-line, such as High Performance Ion Chromatography (HPIC) or spectrophotometry⁵⁸.

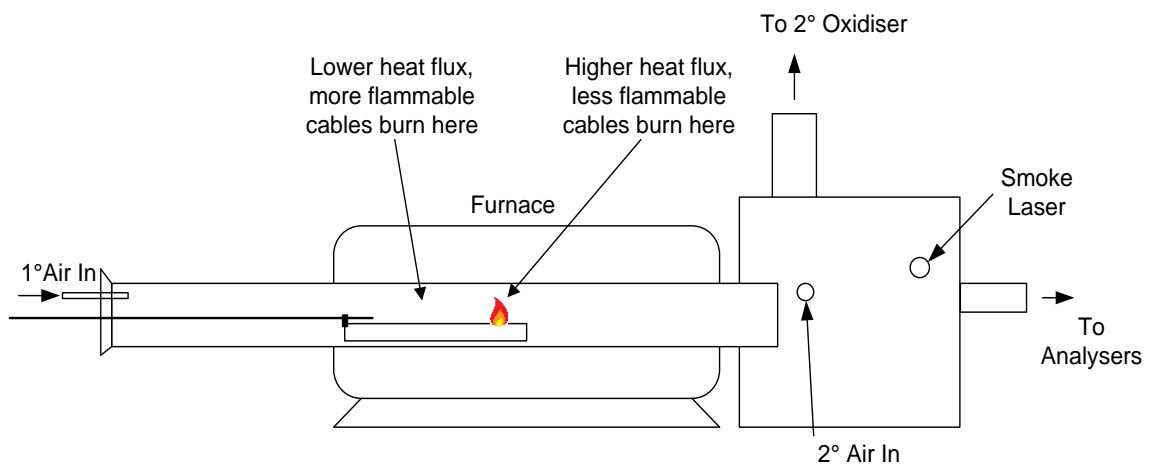


Figure 8 ISO TS 19700 Schematic

1.7.4 Micro Scale Tests

1.7.4.1 Thermogravimetry

Thermogravimetry (TG), (ISO 11358⁵⁹), formally known as thermogravimetric analysis (TGA) is a method of thermal analysis that concerns itself with how a

material's mass changes with increasing temperature⁶⁰. TG equipment consists of two main components: the furnace and the balance (Figure 9). The furnace must conform to a certain number of parameters to ensure that accurate data is produced. These include temperature, air flow and heating rate, these parameters must be the same between any tests to be compared. Typically balances have a maximum load of 1 g with sensitivities in the order of $1\mu\text{g}$ ^{9,61}.

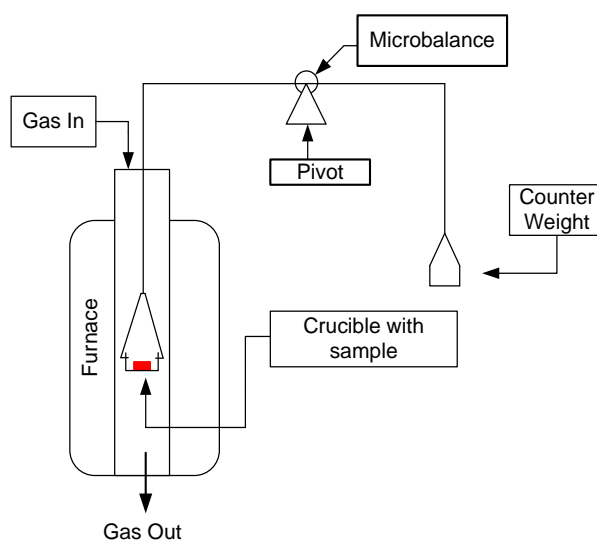


Figure 9 TGA Schematic

Samples can be analysed in either an air or nitrogen atmosphere. In air the curves generated will be that of oxidative pyrolysis whilst if run in a nitrogen atmosphere the decomposition curve will be representative of how the material would behave directly under a flame²².

Often materials have characteristic decomposition curves, with the changes in the curve being linked to particular thermal events. PVC which has a characteristic 2 stage decomposition curve, where the first step is the loss of HCl and the second being the breakdown of the remaining conjugated chain into unsaturated and aromatic molecules⁶². It is characteristic as it is the decomposition curve does not display the characteristics associated generic two step decomposition. PVC is unusual in being autocatalytic, resulting in the decomposition steps differing in magnitude and the steps themselves often not being vertical. Figure 10 displays the differences between a generic two step decomposition and a PVC two step decomposition.

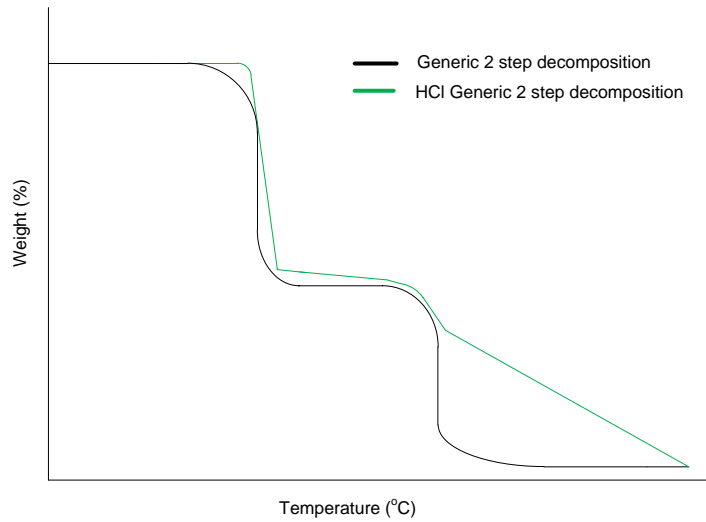


Figure 10 Generic Two Step Decomposition

1.8 LARGE-SCALE TEST

The large-scale method used in this study is a modified bunched vertical wire test (IEC 60332-3⁶³) adapted to undertake heat release measurements as prEN 50399-2-1⁶⁴. Cables are mounted onto a ladder attached to a wall of the test chamber. Cables are ignited using a 20kW propane primary burner, with a secondary burner located further up in the test chamber. Both burners are on for the full duration of the test⁴⁸.

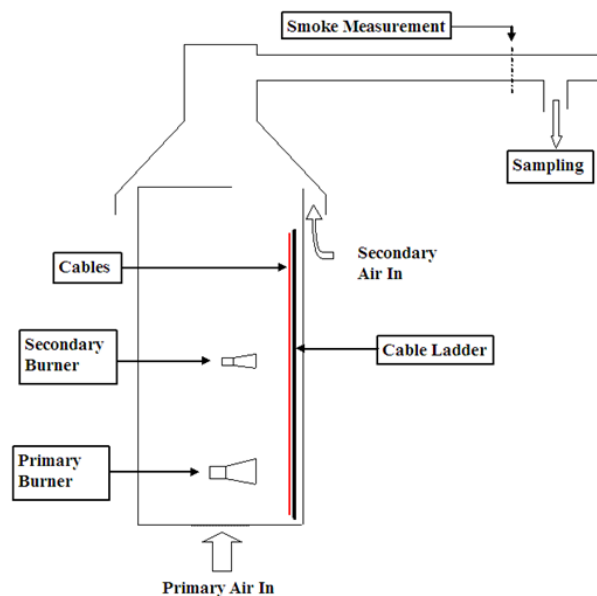


Figure 11 prEN 50399-2-1 Schematic

Air ingresses into the test rig through a perforated base plate in the floor, at a rate of between 0.7 and 1 m³s⁻¹. Such a high volume is used to ensure that there is always an excess of air, forcing combustion, meaning that the fire stage represented is well-ventilated, although attempts have been made to perform under-ventilated tests using a modified protocol. Secondary air is introduced into the duct at a rate that ensures a correct Reynolds number (a dimensionless number used to describe the flow of a fluid as either turbulent or laminar⁶⁵) within the duct. Smoke opacity is measured using a laser further down the duct. The apparatus has been further adapted for fire toxicity with gas analysis is carried out using an FTIR which is sampled from a point in the duct just beyond the smoke laser⁴⁸.

1.9 PROBLEMS SCALING FROM BENCH TO LARGE-SCALE TEST

The problem of trying to replicate large-scale tests on a small-scale is the accurate replication of fire conditions^{40,48}. These include temperature, residence time in the fire plume, radiation from the flame to the material, ventilation to the fire plume and reactions occurring outside the fire plume⁶⁶. Crucially it is these that dictate both the rate and the extent of burning. With respect to the large-scale test being used in this work (prEN 50399-2-1⁶⁴), there are some more specific problems that may be encountered. The large amount of air used in the test, means that a large portion of that air will pass around the fire plume, resulting in two problems: firstly the air that has not passed through the fire plume will be cooler, which results in a quenching of fire gases⁶⁶; secondly the large volume of air will cause dilution of the fire gases within the effluent, making detection and analysis more difficult. Another set of problems is associated with the incomplete burning of the entire cable. Observations made by the technicians who carried out the large-scale testing revealed that some of the cable was either un-burnt or only partially burnt, making mass-loss analysis difficult as the extent of burning is directly related to the amount of mass lost. Hence if the extent of burning is not accurately known the mass loss estimation will be less accurate. Another problem involving mass loss in the large-scale test stems from the samples being mounted vertically which poses problems if the sample being tested melts and subsequently drips. If this dripping is flaming then it may result in the downwards propagation of the flame not experienced by other experiments. If dripping causes loss of material to the test rig floor the mass

loss for the experiment will be inaccurate: the mass loss for the experiment is calculated by weighing the cable ladder before and after a test, so if any material is on the test rig floor it won't be weighed.

In the areas that were only partially burnt the fire temperature may have only reached values of approximately 300°C – 400°C, which posed a problem with cables containing hydrated fillers. At this temperature the fillers would decompose, leaving water, giving a mass loss, yet a high proportion of un-burnt polymer would remain. This low temperature on parts of the cable also affects CO₂ yields, as below 500°C the gas phase conversion of CO to CO₂ is negligible. A final problem with the large-scale test is with regards to HCl analysis. HCl is a polar compound and as such is 'sticky', meaning that it will readily adsorb onto the sides of the test chamber and onto soot particles, the IEC 60332-3⁶³ uses a large exhaust duct, allowing the generation of large soot particles, onto which greater quantities of HCl can be adsorbed⁶⁶. These absorbed HCl particles will not be collected for analysis, resulting in an inaccurate measurement of HCl present, and thus an inaccurate yield value.

2. BENCH SCALE INVESTIGATION

As the work undertaken during the course of this research project was based on comparing results between two scales, part of the study was concerned with that conducted at the bench-scale. The bench-scale method chosen to generate data for the comparison was the steady state tube furnace ([Section 1.7.3.2](#)) due to its ability to accurately produce numerous different fire conditions, and its suitability for testing axially symmetric products such as cables.

2.1 MATERIALS

Most cable materials tend to follow similar patterns as regards their composition. PVC cable, both sheathing and insulation, contain roughly equal amounts of PVC polymer, plasticiser (di-iso octyl phthalate is common), and chalk. For non-halogenated products, the most common polymer used is polyethylene (PE), combined with either alumina trihydrate (ATH) or magnesium hydroxide (MH or MGH) which form the fire retardant component of the cable sheath. The compositions of non-halogenated products are also generally the same; with the sheath comprising of approximately 30% PE and 70% fire retardant filler (ATH or MGH). A list of the cables that were tested can be seen in [Table 4](#).

[Table 4 List of Materials](#)

Cable Name	Type	Composition
1 x 2.5 mm ² LSOH	Non-halogenated	Unknown
3 x 1.5 mm ² LSOH	Non-halogenated	Unknown
FR 4804	Non-halogenated	Polyethylene (PE) based commercial CASICO grade with 30% chalk
Melos 1006 ATH	Non-halogenated	commercial Ethylene Vinyl Acetate (EVA)/ Alumina Trihydrate (ATH) commercial grade
MGN 09006	Non-halogenated	36% chalk, 51.5% Ethylene-Methacrylic Acid (EMAA), 5% Polydimethylsiloxane (PDMS) and 7,5% Low-density Polyethylene (LDPE).
WLS 08005	Non-halogenated	Ethylene methacrylate (EMA)/ Alumina Trihydrate (ATH) commercial grade
1 x 25 mm ² PVC	Halogenated	Unknown

2.2 STEADY STATE TUBE FURNACE

As previously mentioned in [Section 1.7.3.2](#) the steady state tube furnace is capable of accurately controlling ventilation conditions under which a sample is tested. This feature of the method makes the steady state tube furnace ideal for attempting to replicate ventilations conditions found in the large-scale test apparatus.

2.2.1 Preliminary Work

Prior to any practical investigation parts of the steady state tube furnace had to be calibrated to ensure that accurate, reliable results would be obtained. There was also some preliminary work carried out on the cable materials themselves to ensure the correct sample loading was chosen.

2.2.1.1 Air Flow Calibration

Different fire conditions will generate different yields of products, and in the SSTF the fire condition is directly affected by the amount of air flowing over the specimen. When using the steady state tube furnace the flow set on the flow meter is not the same as the flow that enters into the furnace. Thus a calibration curve is necessary in order to be able know what value to set on the flow meter to obtain the required air flow into the furnace. The air flows were calibrated using a domestic gas meter. The gas meter was attached to the primary air inlet tube on one side, and open to atmosphere on the other. It was attached at the primary air inlet tube as the flow ingresses into the furnace from here, so the flow measured here will be an accurate representation of the actual flow. The other side was open to atmosphere simply to avoid any back pressure ([Figure 12](#)).

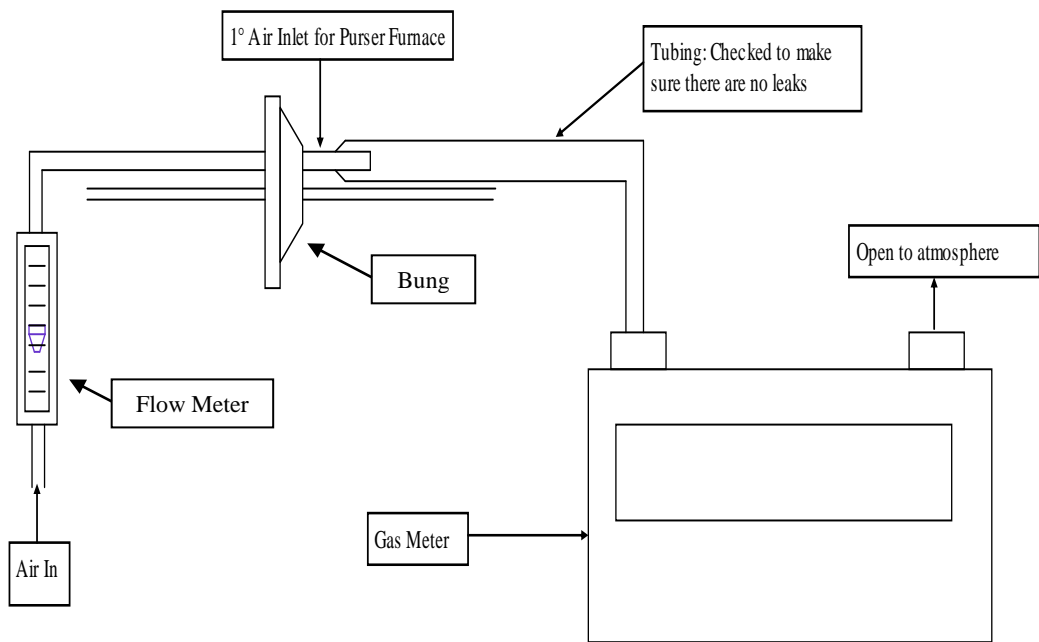


Figure 12 Primary Air Flow Calibration Set-up

When recording the actual flow the air is initially turned on in order to set the flow meter to the set-flow, once done the air is turned off. The reading on the gas meter is recorded as the start point, the air is then turned back on again and simultaneously timing is started. The air is left on for approximately three minutes; the air is then turned off as the timing is stopped.

The calibration of the secondary air flow is undertaken in exactly the same manner as the primary air flow, the only difference being the gas meter is attached to the secondary air inlet (Figure 13).

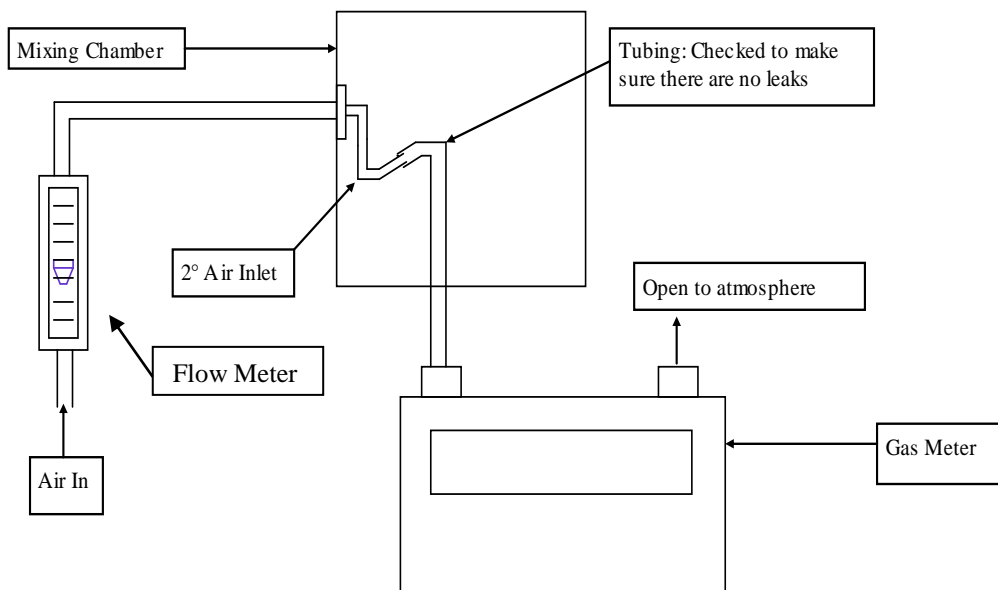


Figure 13 Secondary Air Flow Calibration Set-up

2.2.1.1.1 Calibration Results

Table 5, Table 6, and Table 7 show the raw results from the calibration undertaken on all three air flows; two primary and one secondary. The calibrations were done in duplicate, run 1 and run 2. The set flow column is the value that was set on the flow meter and is the same across both runs. The start and end column display the values recorded from the gas meter, the difference between the two giving the total flow, which was then converted from m³ to L and displayed in the volume column. The volume was then divided by the time to give the flow which is recorded in the flow column. After duplicate runs had been carried out the average actual flow was calculated by averaging the values for actual flow from the two runs. It is the set flow and average actual flow values that are used to generate the calibration curves for the air flows.

Table 5 0.6 – 5 L/min Primary Air Flow Calibration

0.6 - 5 L/min	Run 1					Run 2					Avg
Set Flow (L/min)	Start (m ³)	End (m ³)	Volume (L)	Time (min)	Flow (L/min)	Start (m ³)	End (m ³)	Volume (L)	Time (min)	Flow (L/min)	Flow (L/min)
0.98	19.770	19.773	3.60	3.03	1.19	19.212	19.216	3.70	3.10	1.19	1.19
1.98	19.775	19.783	7.40	3.05	2.43	19.721	19.729	7.40	3.03	2.44	2.43
2.98	19.787	19.798	11.40	3.07	3.72	19.733	19.744	11.20	3.00	3.73	3.73
3.98	19.749	19.764	15.00	3.07	4.89	19.803	19.818	15.00	3.05	4.92	4.91

Table 6 2 - 25 L/min Primary Air Flow Calibration

2 - 25 L/min	Run 1					Run 2					Avg
Set Flow (L/min)	Start (m ³)	End (m ³)	Volume (L)	Time (min)	Flow (L/min)	Start (m ³)	End (m ³)	Volume (L)	Time (min)	Flow (L/min)	Flow (L/min)
2	15.833	15.845	11.70	4.20	2.78	17.014	17.026	11.60	4.15	2.79	2.79
5	15.850	15.877	27.20	4.25	6.40	17.03	17.056	26.10	4.07	6.41	6.40
10	15.884	15.936	51.70	4.06	12.72	15.944	15.999	55.50	4.36	12.72	12.72
15	16.018	16.094	76.40	4.06	18.81	16.098	16.174	76.20	4.05	18.81	18.81
20	16.516	16.618	101.40	4.05	25.03	16.623	16.725	102.20	4.08	25.03	25.03
25	16.737	16.864	127.40	4.14	30.78	16.876	17.006	129.40	4.20	30.78	30.78

Table 7 6 – 50 L/min Secondary Air Flow Calibration

6 - 50 L/min	Run 1					Run 2					Avg
Set Flow (L/min)	Start (m³)	End (m³)	Volume (L)	Time (min)	Flow (L/min)	Start (m³)	End (m³)	Volume (L)	Time (min)	Flow (L/min)	Flow (L/min)
6	17.104	17.143	38.80	4.07	9.54	17.158	17.198	39.70	4.17	9.53	9.53
10	17.257	17.316	59.30	4.08	14.55	17.328	17.387	58.80	4.04	14.56	14.55
20	17.430	17.560	129.90	4.81	26.98	17.577	17.686	108.80	4.03	26.98	26.98
30	17.712	17.869	157.30	4.05	38.86	18.058	18.215	157.00	4.04	38.86	38.86
40	18.738	18.943	204.90	4.03	50.79	19.225	19.431	206.40	4.06	50.79	50.79

2.2.1.2 Air flow Validation

To ensure the calibration generated results that were accurate, a validation procedure was carried out. This involved using a controlled flow of nitrogen as the primary “air”, using the secondary air flow, set with the recently acquired calibration results, to make the total volume up to 50 lmin⁻¹. The procedure is based on the principle that 100% air contains 20.95% oxygen and that if nitrogen is used to replace some of that air then the oxygen concentration, in percent, can be calculated according to Equation 4:

$$Expected O_2 (\%) = 20.95 \times \frac{50 - N_2 Flow Rate}{50}$$

Equation 4 Expected O₂%

Nitrogen was introduced at a series of different flows using a mass flow controller to ensure an accurate flow. At each flow rate the oxygen analysers were allowed to stabilise and maintain that level for a couple of minutes before the flow rates were changed to the next values in the series.

The mass flow controller used to control the nitrogen flow rate was downstream of the primary inlet into the furnace, in much the same way the air flow meters that had just been calibrated were, as such it was necessary to calibrate the mass flow controller. This is because the flow rate which the mass flow controller had set, whilst correct at that point in the system, would not be that value by the time it was entering the furnace due to the amount of pipe work as well as the flow meters the nitrogen would have to pass through before reaching the furnace.

Table 8 Mass Flow Controller Validation

Mass Flow Controller	
Set Flow (L/min)	Actual Flow (L/min)
2	1.06
4	1.92
6	2.93
8	4.04
10	5.16

Table 8 shows the results for the mass flow controller calibration. The table shows a large difference in values between the set and actual flows. With the actual flow being approximately half of the set flow across the entire range. Whilst the actual flow may be distinctly different from the value set on the mass flow controller this does not make the flow any less controlled, the actual flow would still be a consistent value throughout the duration of the test, as long as the actual value is known the validation is still correct.

2.2.1.2.1 Validation Results

Figure 14 shows the comparison between the measured and expected values for O₂ % in the furnace. The measured values, represented by blue diamonds, are those recorded from the steady state tube furnace using nitrogen as a primary gas, whereas the expected values, represented by red squares, are those calculated using Equation 4. If the calibration method is accurate the measured values should be the same as the calculated (red) values. In terms of the validity of the calibration method, it shows clearly that the method is indeed valid, for each of the primary flow rates the two markers are either completely over-lapped or very nearly over-lapped. In terms of percentages, all the measured values are within 1% of the expected values, as can be seen in Table 9.

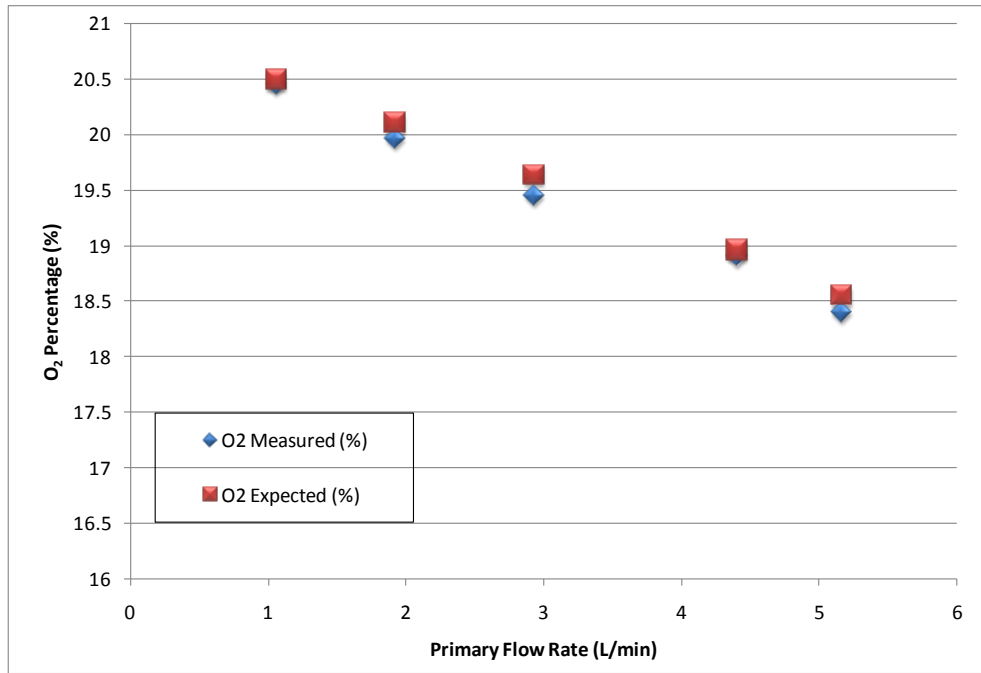


Figure 14 N₂ Validation Results

Table 9 Comparison of Measured and Expected O₂ Results

O₂ Measured (%)	20.46	19.97	19.45	18.91	18.40
O₂ Expected (%)	20.50	20.11	19.64	18.96	18.56
Expected/Measured (%)	99.80	99.28	99.05	99.71	99.16

The raw calibration data could then be turned into the final, end-use, tables of set flow (L/min) versus actual flow (L/min).

Table 10 0.6 - 5 L/min Calibration Table

Actual Flow (L/min)	Set Flow (L/min)	Actual Flow (L/min)	Set Flow (L/min)
0.60	0.50	3.50	2.83
0.70	0.58	3.60	2.91
0.80	0.66	3.70	2.99
0.90	0.74	3.80	3.07
1.00	0.82	3.90	3.15
1.10	0.90	4.00	3.23
1.20	0.98	4.10	3.31
1.30	1.06	4.20	3.39
1.40	1.14	4.30	3.47
1.50	1.22	4.40	3.55
1.60	1.30	4.50	3.63
1.70	1.39	4.60	3.71
1.80	1.47	4.70	3.80
1.90	1.55	4.80	3.88
2.00	1.63	4.90	3.96
2.10	1.71	5.00	4.04
2.20	1.79		
2.30	1.87		
2.40	1.95		
2.50	2.03		
2.60	2.11		
2.70	2.19		
2.80	2.27		
2.90	2.35		
3.00	2.43		
3.10	2.51		
3.20	2.59		
3.30	2.67		
3.40	2.75		

Table 11 2 - 25 L/min Calibration Table

Actual Flow (L/min)	Set Flow (L/min)	Actual Flow (L/min)	Set Flow (L/min)
2.00	1.32	16.50	13.17
2.50	1.73	17.00	13.58
3.00	2.14	17.50	13.99
3.50	2.54	18.00	14.40
4.00	2.95	18.50	14.80
4.50	3.36	19.00	15.21
5.00	3.77	19.50	15.62
5.50	4.18	20.00	16.03
6.00	4.59	20.50	16.44
6.50	5.00	21.00	16.85
7.00	5.41	21.50	17.26
7.50	5.81	22.00	17.66
8.00	6.22	22.50	18.07
8.50	6.63	23.00	18.48
9.00	7.04	23.50	18.89
9.50	7.45	24.00	19.30
10.00	7.86	24.50	19.71
10.50	8.27	25.00	20.12
11.00	8.67		
11.50	9.08		
12.00	9.49		
12.50	9.90		
13.00	10.31		
13.50	10.72		
14.00	11.13		
14.50	11.53		
15.00	11.94		
15.50	12.35		
16.00	12.76		

Table 12 6 - 50 L/min Calibration Table

Set Flow (L/min)	Actual Flow (L/min)	Set Flow (L/min)	Actual Flow (L/min)
1.00	3.43	20.50	27.28
1.50	4.04	21.00	27.89
2.00	4.66	21.50	28.49
2.50	5.28	22.00	29.10
3.00	5.89	22.50	29.70
3.50	6.51	23.00	30.30
4.00	7.13	23.50	30.91
4.50	7.74	24.00	31.51
5.00	8.36	24.50	32.12
5.50	8.97	25.00	32.72
6.00	9.59	25.50	33.32
6.50	10.20	26.00	33.92
7.00	10.82	26.50	34.53
7.50	11.43	27.00	35.13
8.00	12.04	27.50	35.73
8.50	12.66	28.00	36.33
9.00	13.27	28.50	36.93
9.50	13.88	29.00	37.53
10.00	14.49	29.50	38.13
10.50	15.10	30.00	38.73
11.00	15.72	30.50	39.33
11.50	16.33	31.00	39.93
12.00	16.94	31.50	40.53
12.50	17.55	32.00	41.13
13.00	18.16	32.50	41.73
13.50	18.77	33.00	42.33
14.00	19.38	33.50	42.93
14.50	19.99	34.00	43.53
15.00	20.60	34.50	44.12
15.50	21.21	35.00	44.72
16.00	21.82	35.50	45.32
16.50	22.42	36.00	45.91
17.00	23.03	36.50	46.51
17.50	23.64	37.00	47.11
18.00	24.25	37.50	47.70
18.50	24.85	38.00	48.30
19.00	25.46	38.50	48.89
19.50	26.07	39.00	49.49
20.00	26.67	39.50	50.08

2.2.1.3 Driving Mechanism Speed Calibration

According to ISO TS 19700²⁹ the steady state tube furnace requires a fuel feed rate of 1 g/min. For pelleted samples, such as manufactured polymers, it is easy to obtain a loading of 1 g/min. However for cables the drive speed must be adjusted to match the linear density of the non-metallic cable components. A drive speed was selected, and the driving mechanism allowed to move the boat for 5 minutes, the start and end points of the boat were recorded thus giving the distance and speed of the boat.

2.2.1.3.1 Setting the Driving Mechanism Speed

The driving mechanism used with the Purser furnace in this study utilises a frequency generator and a stepper motor. On one circuit board are 8 switches, which can either be off (0) or on (1), the arrangement of which dictates the frequency at which a pulse is sent to the motor to tell it to move (Table 13), the less frequent the pulse the slower the driving mechanism will move. Speeds are set with the knowledge that 15 Hz gives a nominal 35 mm/min, and that the relationship is linear.

Even though 8 switches are present the last two are redundant, and are left in the on position.

Table 13 Setting the Driving Mechanism Speed

Set Terminal		4	0	0	0	0	1	1	1	1
		5	0	0	1	1	0	0	1	1
1	2	3 \ 6	0	1	0	1	0	1	0	1
0	0	0	600K	60K	6K	600	60	6	0.6	0.06
0	0	1	60K	6K	600	60	6	0.6	0.06	0.01
0	1	0	600K	30K	3K	300	30	3	0.3	0.03
0	1	1	500K	20K	2K	200	20	2	0.2	0.02
1	0	0	150K	15K	1.5K	150	15	1.5	0.15	0.02
1	0	1	120K	12K	1.2K	120	12	1.2	0.12	0.01
1	1	0	100K	10K	1K	100	10	1	0.1	0.01
1	1	1	50K	5K	500	50	5	0.5	0.05	0.01

To generate a speed of 35 mm/min, the required frequency is 15, so from the table the setting on the circuit board would be 10010011. If a speed of approximately 10

mm/min was required then the closest frequency would be 5 Hz, as $10 \approx$ a third of 35. Again reading off the table a frequency of 5 Hz, thus a speed of approximately 10 mm/min, would require the circuit board to be set to 11110011.

The four standard speeds that have been set and calibrated for the steady state tube furnace are given in Table 14.

Table 14 Driving Mechanism Speed Settings

Set Speed (mm/min)	Frequency (Hz)	Switch Number Setting							
		1	2	3	4	5	6	7	8
11.66	5	1	1	1	1	0	0	1	1
23.3	10	1	1	0	1	0	0	1	1
35	15	1	0	0	1	0	0	1	1
46.66	20	0	1	1	1	0	0	1	1

2.2.1.3.2 Driving Mechanism Calibration Results

The results in Table 15 to Table 18 all show that the weight of the boat being moved has a negligible effect on the speed. They also show that there is indeed a difference between the speed that is selected and the actual speed that it corresponds to. This difference between set and actual speeds appears to widen with the increases in speed. Whilst the differences in set and actual speed are not vast amounts, over long testing periods, such as those encountered in cable testing, the effect of that difference would be ever increasing.

Table 15 11.6 mm/min Speed Calibration

Set Speed	11.6 mm/min			
Mass (g)	Start (cm)	End (cm)	Time (min)	Speed (mm/min)
20	10.0	15.9	5.0	11.8
40	10.0	15.8	5.0	11.6
60	10.0	16.0	5.0	12.0
80	10.1	16.0	5.0	11.8
100	10.0	16.0	5.0	12.0
120	58.1	64.1	5.0	12.0
140	14.1	19.8	4.8	11.8
Average Speed:				11.9

Table 16 23.3 mm/min Speed Calibration

Set Speed	23.3 mm/min			
Mass (g)	Start (cm)	End (cm)	Time (min)	Speed (mm/min)
20	10.2	22.2	5.0	24.0
40	15.8	27.8	5.0	24.0
60	16.0	28.0	5.0	24.0
80	16.0	28.0	5.0	24.0
100	22.2	34.1	5.0	23.8
120	15.4	27.3	5.0	23.8
140	19.8	31.8	5.0	24.0
Average Speed:				23.9

Table 17 35.0 mm/min Speed Calibration

Set Speed	35.0 mm/min			
Mass (g)	Start (cm)	End (cm)	Time (min)	Speed (mm/min)
20	27.7	45.8	5.0	36.2
40	27.8	45.9	5.0	36.2
60	28.0	46.0	5.0	36.0
80	28.0	49.7	6.0	36.2
100	27.9	45.9	5.0	36.0
120	64.1	82.1	5.0	36.0
140	31.8	49.9	5.0	36.2
Average Speed				36.1

Table 18 46.6 mm/min Speed Calibration

Set Speed	46.6 mm/min			
Mass (g)	Start (cm)	End (cm)	Time (min)	Speed (mm/min)
20	45.8	69.9	5.0	48.2
40	45.9	69.9	5.0	48.0
60	46.0	70.0	5.0	48.0
80	49.7	73.6	5.0	47.8
100	34.1	58.1	5.0	48.0
120	45.3	69.4	5.0	48.2
140	49.9	73.8	5.0	47.8
Average Speed				48.0

2.2.1.4 Cable Sample Preparation

Cables contain both polymeric compound, a collective name for any sheathing, insulating and bedding material present, and a copper conductor. Only the polymeric material burns, but both the polymeric material and copper conductor contribute to the mass of sample. Thus it is necessary to know the amount of both polymeric material and copper conductor in terms of percentage by mass. This is calculated for each cable sample by taking a 10 cm section and weighing its constituents. The linear density was then combined with the driving mechanism speed to calculate the feed rate of that cable type for each speed setting (Table 19).

Table 19 Calculating Feed Rate

Cable Name	Speed (mm/min)	Length (mm)	Total Weight (g)	% Cable Compound	% Copper	Linear Density (Complete) (g/mm)	Linear Density (cable compound) (g/mm)	Feed Rate (g/min)
3 x 1.5mm ² LSOH	11.86	700	90.34	74.92	25.02	0.13	0.09	1.05
	23.94	700	90.34			0.13	0.09	2.11
	36.11	700	90.34			0.13	0.09	4.23
	48.00	700	90.34			0.13	0.09	4.64

Table 19 shows all the different feed rates attainable using the possible speed selections, the aim is to determine what speed will give a feed rate closest to 1, as can be seen in Table 19 for the cable type 3x1.5 mm² LSOH, this is a feed rate of 1.05 g/min, using a speed of 11.86. Percentage by mass and feed rate data for all cables tested is available in Appendix A

2.2.2 Methodology

Once the Purser furnace calibrations have been completed then it is ready for testing. Testing falls into three main sections:

- Setup and calibration
- Test
- Post-Test

2.2.2.1 Setup and Calibration

Prior to calibrating the analysers both the primary and secondary furnaces were turned on and allowed to warm-up, the desired temperature for the primary furnace depends on what tests are being run, whilst the secondary furnace is set at 900 °C. The on-line analysers (CO₂, O₂, CO and Smoke Optical Density) were calibrated before each test. These analysers need to be protected from corrosive gases, water, etc. using a combination of filters, silica gel, soda lime and various liquids/solutions as shown in [Figure 15](#).

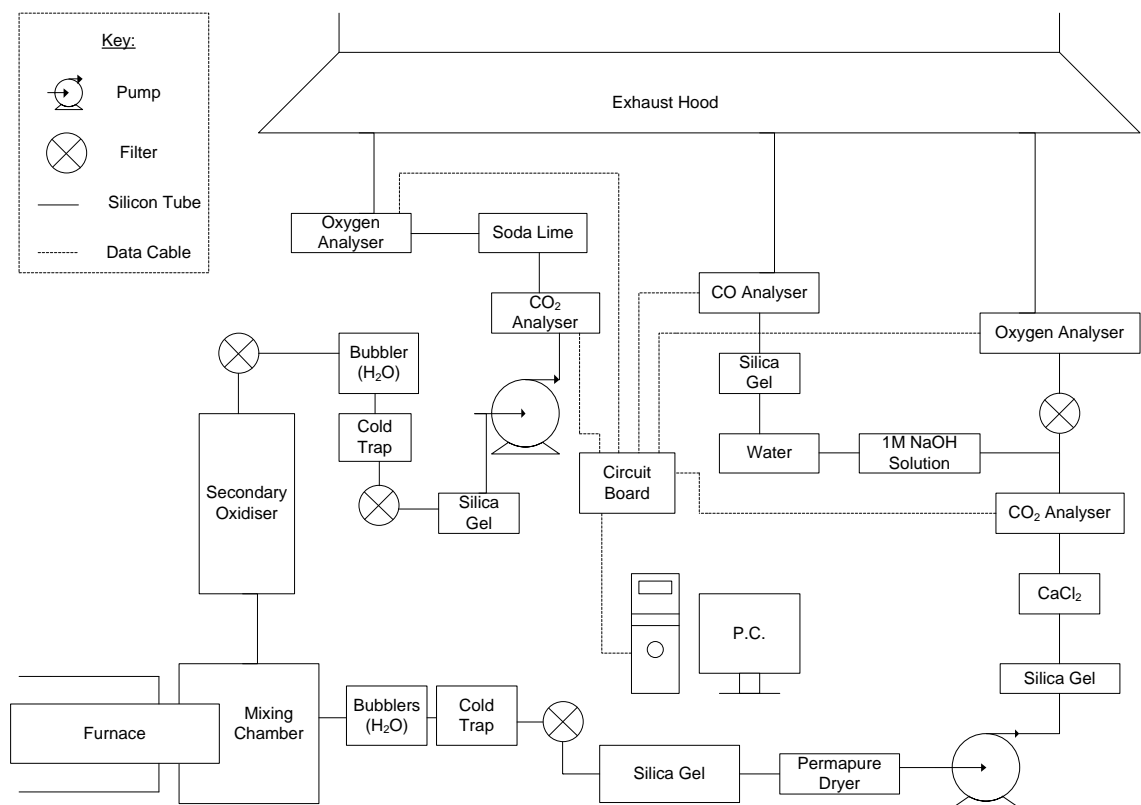


Figure 15 Layout of SSTF Analyser Chain

The two bubblers were filled with water to remove any acid gases, the cold traps with ice in order to condense any water in the effluent. Drying tubes are filled with silica gel. Sodium hydroxide scrubs any CO₂ from the effluent that would interfere with the CO reading, it needs to be 1 M concentration to be effective and as such has to be checked to ensure it hasn't been neutralised with the aid of methyl orange indicator in the solution. The CaCl₂ acts as a further desiccant to make sure there is no moisture in the effluent passing through the CO₂ analyser. Finally the receptacles for both the silica gel and the CaCl₂ contain glass wool, which act to trap any particulates in the effluent, these plugs of glass wool need to be checked at regular intervals to make sure that they haven't trapped so many particulates as to block the flow of effluent through the analyser chain.

The analysers were calibrated in a three stage process. In the first stage the analysers were connected to a nitrogen line, which acts as a zero-gas for the CO₂, CO and O₂ analysers, and the optical density laser is completely blocked using an opaque object. The second stage has the analysers all connected to a 4% CO₂, 6000 ppm CO mix, which acts as a span gas for the CO₂ and CO analysers, whilst acting as a second zero-gas for the oxygen analysers, the optical density laser is covered with a filter of absorbance 0.3 . Finally the third stage sees the analyser chain connected up as it would be a test and has air passed through the CO₂, CO and O₂ analysers, acting as a zero gas for the first two, and a span gas for the latter; the optical density laser is covered with a 0.8 filter. For all three stages the analysers have to show stable readings for two minutes before the calibration data is collected for that stage.

After calibration the sample was prepared in accordance with parameters of that test (length, mass, etc.). An empty boat was weighed and recorded, the sample was placed into the boat to give a mass for the boat and sample, and by subtracting the former from the latter the mass of sample was given. If the sample is of granular or similar nature, then it was spread out evenly over the length required to ensure uniform linear density, according to ISO TS 19700⁵⁸.

Once the sample is prepared and loaded into the outer tube, the primary and secondary air flows are set using the relevant calibration table ([Section 2.2.1.2.1](#))

2.2.2.2 Test

As the sample moves into the furnace the time to ignite was recorded and readings of the CO₂ and O₂ analysers were taken. Any sampling to be done for total soot, samples being trapped in bubblers, or desorption tubes for hydrocarbon analysis was done during steady-state conditions, typically for 5 minutes in the central part of the run. At all times during the test it was necessary to constantly check the air flows to ensure they have not lost pressure or flow rate; the flow-rate through the analysers (which has to be above one litre/minute) and the driving mechanism.

2.2.2.3 Post-test.

The test was deemed to be over once the analysers have returned to baseline values. Once the test had finished the time and stop-point were recorded, the recording software stopped and the data saved. The sample was then removed slowly from the furnace, to prevent a forced re-ignition, once removed the sample and boat were allowed to cool. Then the mixing chamber and connecting pipes were cleaned, and if necessary the water in the bubblers replaced, the silica gel is checked to see if that needs replacing (it is self-indicating), CaCl₂ was also checked and replaced. The sample residue's weight and length were both recorded.

2.2.3 Steady State Tube Furnace Results

For all products listed in [Table 20](#) the ϕ range was chosen to cover the estimated range of ventilation conditions within the large-scale test, approximately $0.3 < \phi < 1$. The results presented for the steady state tube furnace are done so in accordance with BS ISO 19703³⁶, and are calculated on a mass charge basis.

Table 20 List of Small-scale Tests and Conditions used

Cable Type	Test Name	Temp (°C)	1° Air (l/min)	ϕ
1 x 2.5 mm ² LSOH	125LSOH 1	825	25	0.14
	125LSOH2	825	10	0.37
	125LSOH3	825	5	0.71
3 x 1.5 mm ² LSOH	315LSOH 1	825	25	0.23
	315LSOH 2	825	15	0.42
	315LSOH 3	825	10	0.59
	315LSOH 4	825	7.9	0.69
	315LSOH 5	825	5.5	0.93
Melos 1006F (ATH)	Melos 1	800	15	0.3
	Melos 2	825	10	0.44
	Melos 3	825	6.25	0.75
	Melos 4	825	4.5	0.85
FR 4804	FR 1	900	15	0.4
	FR 2	900	10	0.67
	FR 3	900	5.5	0.87
	FR 4	900	3.8	1.23
MGN 09005	Man 1	800	10	0.53
	Man 2	825	7	0.71
	Man 3	825	5	0.74
	Man 4	825	3.5	0.97
WLS 08006	WLS 1	800	25	0.36
	WLS 2	825	15	0.58
	WLS 3	825	10	0.74
	WLS 4	825	7	0.86
1 x 25 mm ² PVC	PVC 1	825	10	0.35
	PVC 2	825	5.1	0.70
	PVC 3	825	3.6	0.93

2.2.3.1 Yield Results

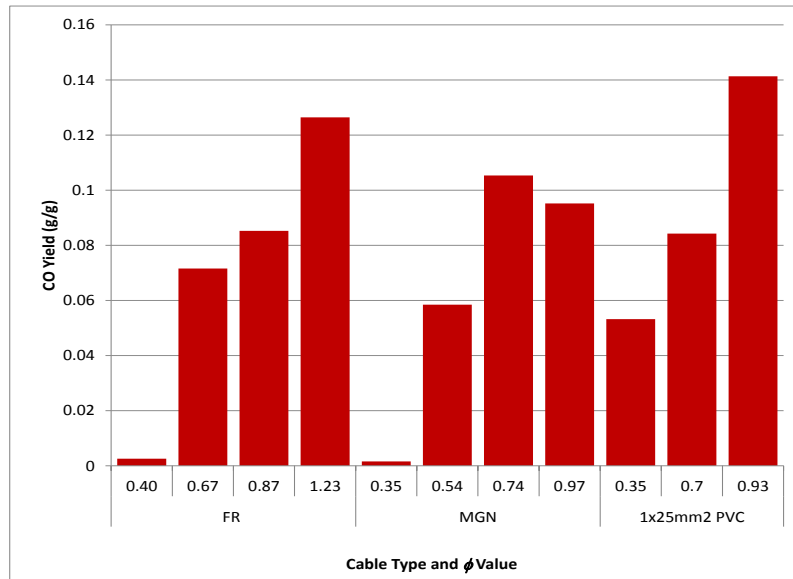


Figure 16 SSTF CO Yields 1

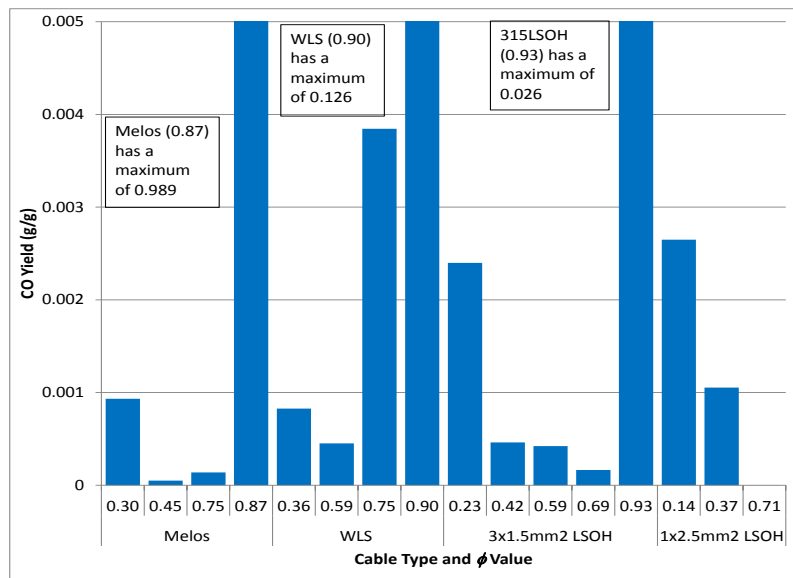


Figure 17 SSTF CO Yields 2

For CO yields the expected trend is an increase in yield with in increasing ϕ as shown in Hull et al⁶⁷. Figure 16 and Figure 17 show the CO yield results for all cable types, only FR and 125PVC display this expected trend across the entire ϕ range, however previous work has shown that for rigid PVC CO yields are expected to be roughly constant across ventilation conditions due to the gas phase interactions of HCl. Owing to this only the FR cable type fits with the expected trend, thus the CO data for all cable types except FR was investigated (Section 2.2.3).

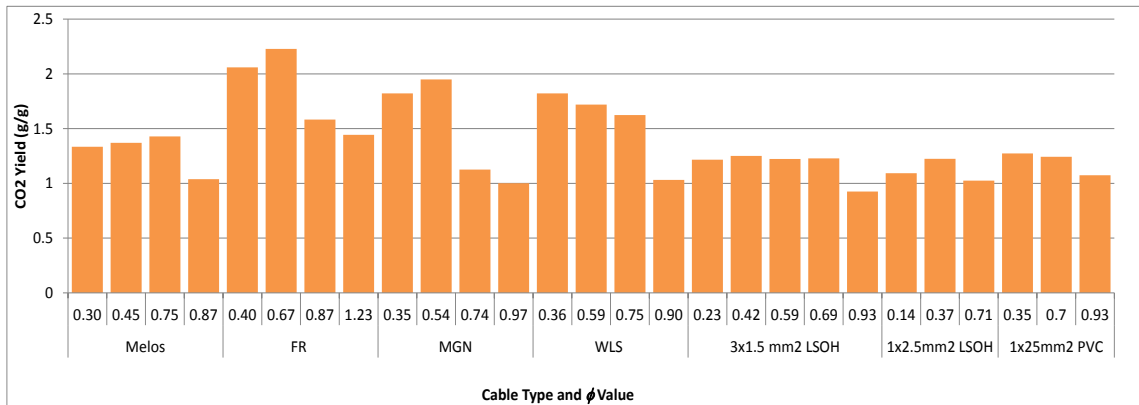


Figure 18 SSTF CO₂ Yields

The CO₂ data (Figure 18) shows a fairly consistent trend across the cable types to increase from a $\phi = 0.3$ towards a $\phi \approx 0.75$. After this point the general trend is for the CO₂ yield to decrease as the value of ϕ increases. However there are exceptions to this trend, those exceptions being WLS and 125PVC. In both cases the highest CO₂ yield is associated with the lowest ϕ , and displays the trend of a decreasing yield of CO₂ with an increasing value of ϕ . The general trend shown by Melos, FR, MGN, 315LSOH, and 125LSOH, fits with the accepted rule that the trends for yield of CO₂ versus ϕ follows an inverse trend to that of CO₄₃

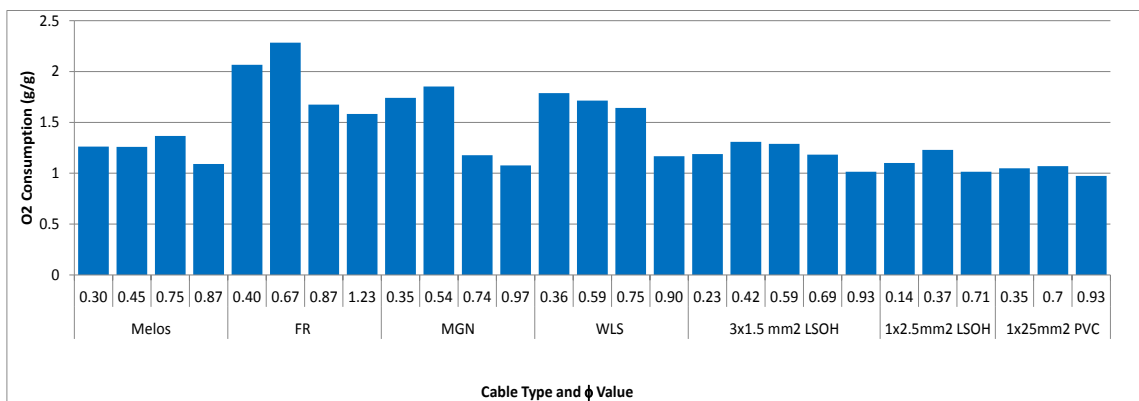


Figure 19 SSTF O₂ Consumed

O₂ consumption data presented in Figure 19 shows the same trends as those displayed by the small-scale CO₂ data shown in Figure 18, with the exception of 125PVC. For O₂ consumed the highest value is at $\phi = 0.7$, whereas for CO₂ yield the highest value is at $\phi = 0.35$. This means that for O₂ consumed all the cable types, except WLS, follow the same trend, yields rise from $\phi = 0.3$ to $\phi \approx 0.75$, before falling as the value of ϕ continues to increase.

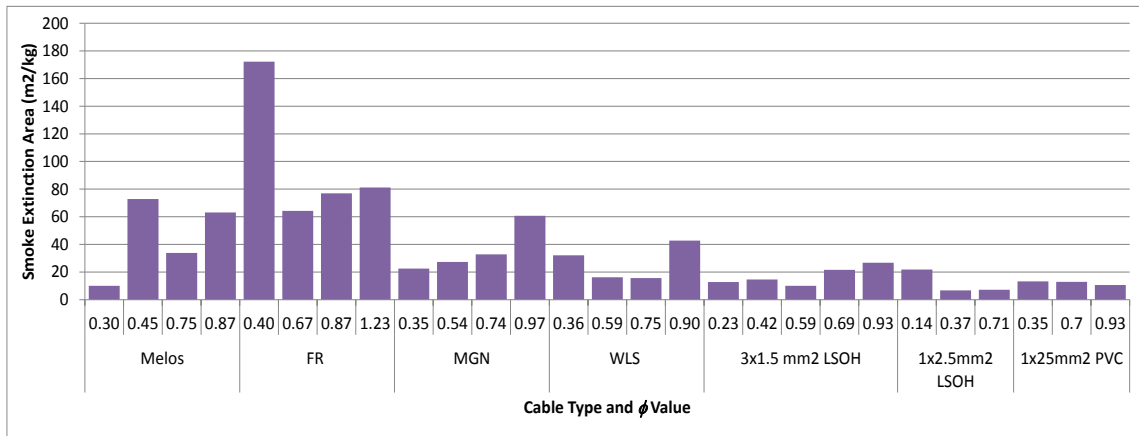


Figure 20 SSTF Smoke Extinction Area

The smoke data (Figure 20) shows a general trend for the smoke extinction area (SEA), to increase with ϕ value across the cable types, although there are some exceptions such as Melos $\phi = 0.45$, FR $\phi = 0.4$, and WLS $\phi = 0.36$. The cable 125PVC goes completely against this trend: showing an overall decrease in SEA value with increasing values of ϕ . Figure 20 also shows that the LSOH cables appear to show a higher smoke production than the PVC cable.

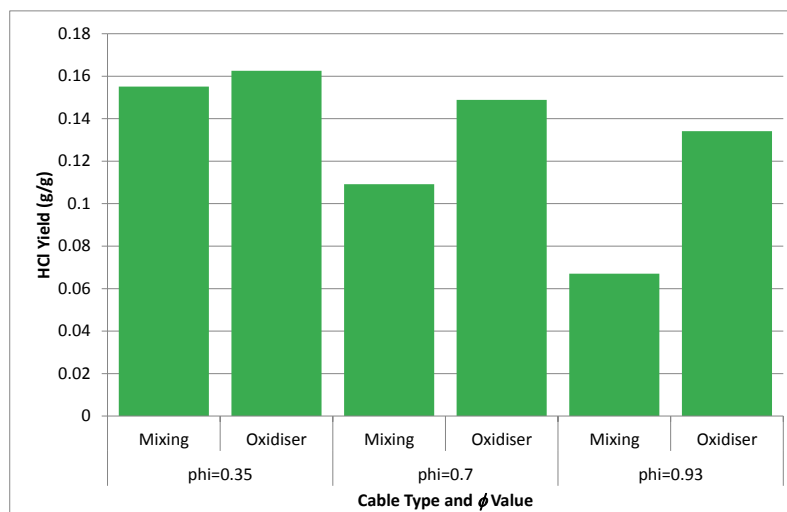


Figure 21 SSTF HCl Yield for 1x25 mm² PVC

Figure 21 shows the HCl yield results from the 125 PVC cable. It shows that across all ventilation conditions there is more HCl found in the bubblers sampling the effluent downstream of the secondary oxidiser, than the bubblers downstream of the mixing chamber. This implies that more than 50% of the total HCl given off during combustion ends up forming a stable molecule, such as an organochlorine, only re-released when oxidised at a very high temperatures (900 °C) to HCl and

Chlorine. The second thing of note is that the HCl yields show an overall decrease with an increasing ϕ , which is unusual as HCl yield is largely assumed to be independent of ventilation conditions⁴⁸.

2.2.3.2 Further CO Analysis

Due to the CO yields presented in (Section 2.2.3.1) deviating from the expected trend the raw data was investigated for possible reasons.

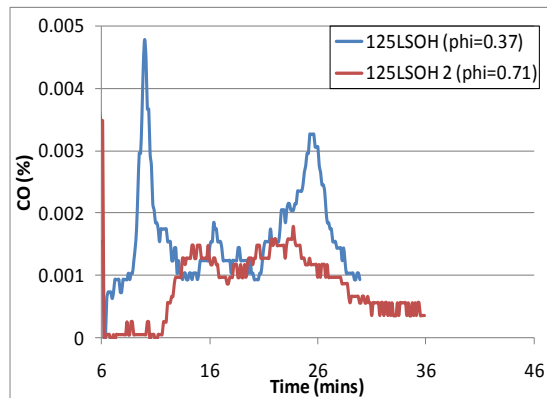


Figure 22 1x2.5 mm² LSOH CO (%)

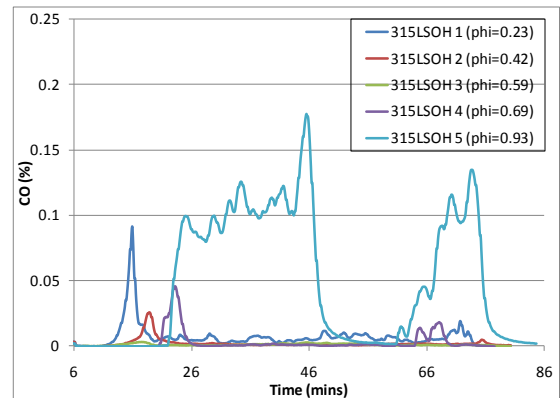


Figure 23 3x1.5 mm² LSOH CO (%)

In Figure 22 neither of the two CO traces have a steady state region, where the line is horizontal. In Figure 23 315LSOH 1 through to 315LSOH 4 all have large relatively stable regions. Whereas 315LSOH 5 has a trough near the middle of the test interrupting a relatively flat line, which could create an erroneous value for the CO average (%), which would then be carried through to the yield calculations.

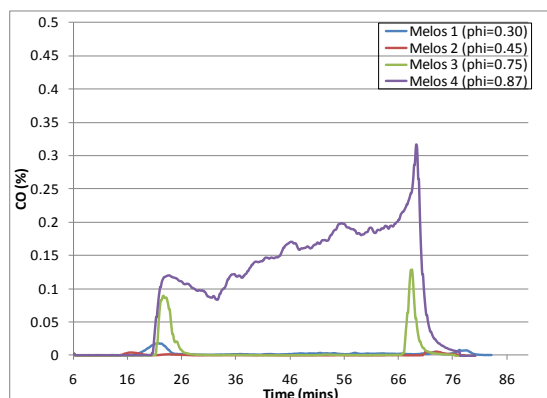


Figure 24 Melos CO (%)

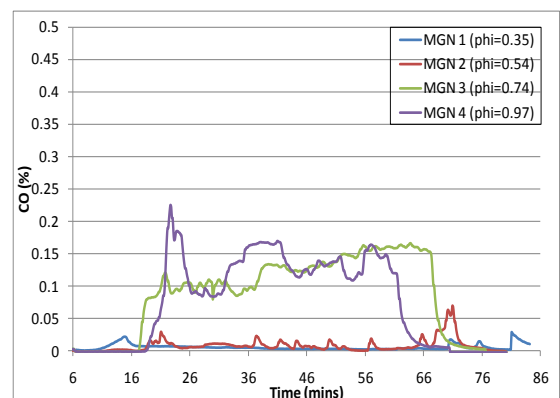


Figure 25 MGN CO (%)

The Melos cable CO results, (Figure 24), are similar to the 3x1.5 mm² LSOH, except for $\phi \approx 0.9$, where the CO trace is near zero and flat. Melos 4 lacks a stable flat area as the CO continues to rise from approximately 30 minutes, all the way to the end of the test. Figure 25 shows the CO trace for MGN, the first two tests are both close to zero and show relatively stable regions, whilst the last two, MGN 3 and 4, have higher values, but are not as stable.

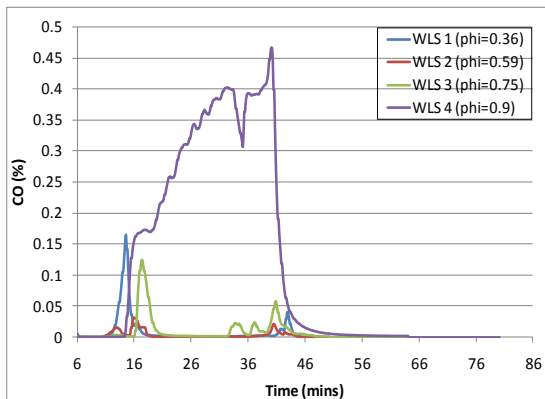


Figure 26 WLS CO (%)

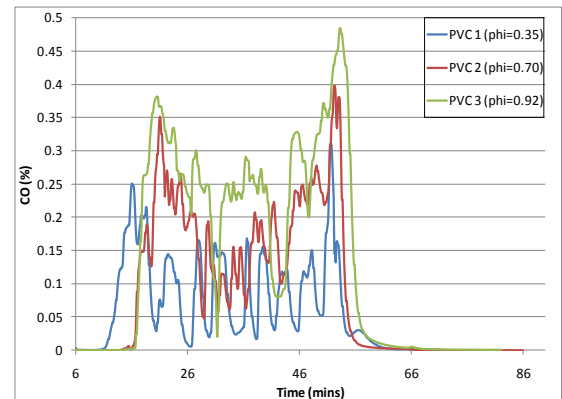


Figure 27 PVC CO (%)

Figure 26 again shows the first 3 tests all having a CO trace close to zero, whilst the last test again shows an increasing yield of CO from near the beginning, all the way to the end of the test. Figure 27 shows an oscillating CO trace for all three ϕ conditions. The unstableness of the traces is not due to a problem with the analyser but is caused by the unsteady burning of the cable which cycled between ignition followed by flaming combustion and extinction followed by non-flaming combustion.

The above figures do display a possible reason for the CO yields not matching the expected trends. The CO yields were calculated in accordance with ISO 19703, which uses the average recorded percentage volume of CO during the test. The established methodology uses a simple arithmetic mean on the data values across the time during which the average was taken. A by-product of which is that this methodology works best on a set of data where the trace has a period where the line is stable, or almost stable. With data that lacks a steady state period the results from the arithmetic mean will vary dependent on the time period taken to be representative, leading to questions over which period is the correct period to use.

In order to try and generate a more accurate value for the average CO (%) each test was integrated using the trapezium rule across the entire test, from beginning to

end (ignoring any spikes at the beginning or the end of the test if present). [Figure 28](#) and [Figure 29](#) display the results of this comparison; [Figure 28](#) displays all of the results for all cable types, whereas [Figure 29](#) displays those results whose magnitudes are too small to clearly be seen in [Figure 28](#). In both figures SSTF Average represents the yield value generated from the arithmetic mean, and the Whole Test Average value represents that generated by integrating over the entire test time.

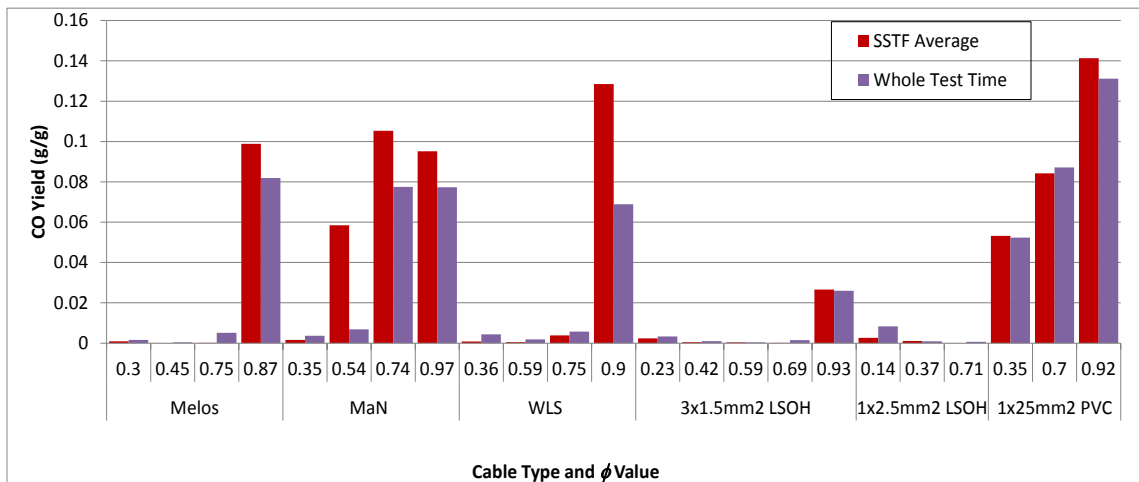


Figure 28 Comparison of CO Yields generated from either the Arithmetic Mean or Integral of the CO data

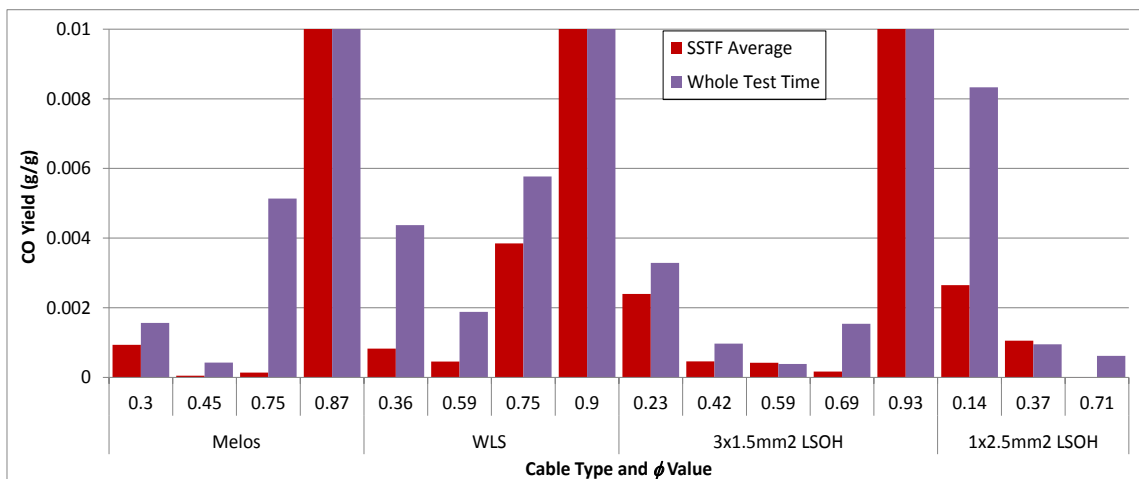


Figure 29 Comparison of CO Yields generated from either the Arithmetic Mean or Integral of the CO data (Y-axis has a smaller scale)

There is a rather large disparity between the two methods for most of the cable types, except 3x1.5 mm² LSOH, 1x2.5 mm² LSOH and PVC cables where data shows good agreement. We believe that the latter method will produce results most reliable to be used when comparing against the large-scale data, as it takes the entire test into account not just an arbitrary time period subjectively chosen by the

analyst, furthermore the large-scale data uses the same integration method to calculate average per cent, thus when comparing between two scales using the same method for calculation yields will be likely to help in establishing a correlation.

However, whilst analysis of the raw CO data may have highlighted a problem with averaging over a fixed time period and the use of integrals may have solved it, the overall trend patterns failed to improve, especially for the cable types Melos and WLS, where the CO yield values increased dramatically between $\phi = 0.75$ and $\phi = 0.9$.

2.2.3.3 Melos and WLS Repeat Tests.

When analysing the yield results for the arithmetic mean based results and the integration based results, both the Melos and WLS cable types show a large increase in the yield between $\phi = 0.75$ and $\phi \approx 0.9$ that does not fit with the results from the other tests carried out on those cable types. With such a large disparity between the values the most likely cause seemed to be either a leak in the analyser line during the first 3 tests, leading to an ingress of air, resulting in a dilution of CO, giving the very low yield values, or some other fault causing the high value of CO in the last test. Therefore the solution was to check the analyser chain for any leaks and carry out repeats of all the tests for the two cable types.

The original tests for both cables are numbered 1-4, whilst the repeats are 5-8.

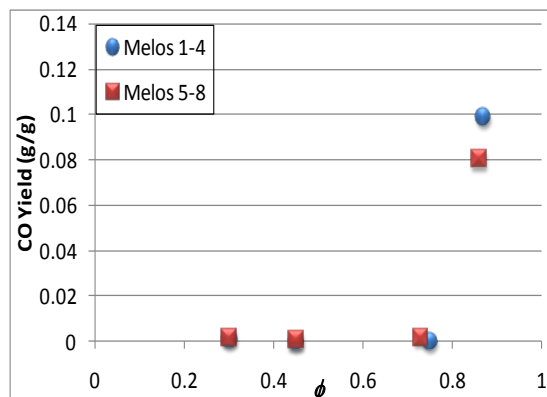


Figure 30 Melos Repeat Tests vs. Original Tests CO Yields

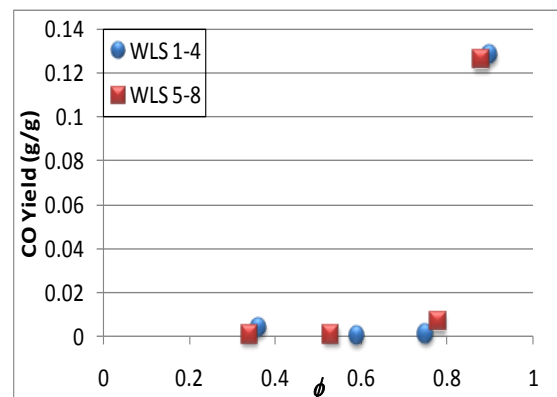


Figure 31 WLS Repeat Tests vs. Original Tests CO Yields

The repeat tests for both Melos (Figure 30) and WLS (Figure 31) match both the low and the high CO values, which rules out the possibility of an error or a leak causing the large increase between $\phi = 0.75$ and $\phi \approx 0.9$. In order to gain a better idea of what was happening in the narrow ϕ value window between the third and fourth tests, an extra test was carried out to place a data point within that empty window. The results of which are shown in Figure 32 for Melos and Figure 33 for WLS.

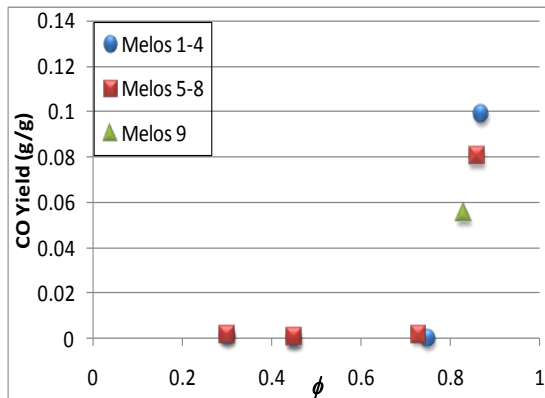


Figure 32 Melos Complete CO Yield Data

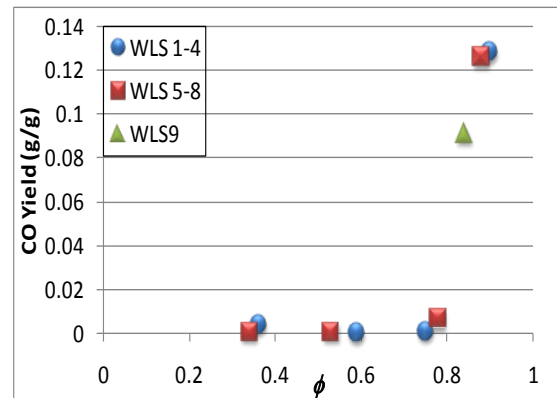


Figure 33 WLS Complete CO Yield Data

These results show that when $\phi > 0.75$ both Melos and WLS show a dramatic increase in CO yield. Thus for these two cables the toxicological impact of CO will increase dramatically as the fire conditions move from well-ventilated to under-ventilated.

3 LARGE-SCALE TESTING

Unlike the data generated from the Purser furnace, the data generated from the large-scale test method does not involve a steady-state period of burning. This meant that in the absence of such a steady-state period the large-scale data required integrating to calculate an average for each species before yields could be calculated.

3.1 CALCULATING AVERAGES

When calculating the average concentration of a particular species the method used to do so depended on what species was being analysed. Both the oxygen and smoke, measured using transmission, calculation use the same methodology, whilst CO₂ and CO use separate methodologies that whilst very similar to each other, are very different to the one used for the oxygen and smoke calculations.

3.1.1 CO₂ and CO averages.

In order to calculate the area under the curve, the Trapezium Rule of integration was applied to the raw data, giving the total amount of gas (%) evolved during the test. [Figure 34](#) shows the sequence of how the raw CO₂ data was handled to generate an average percentage value for the large-scale test. In graph A the raw data is plotted, and that data is integrated to give a total CO₂ (%). Next in graph B the baseline is plotted, the baseline value is taken to be the value of CO₂ (%) at Time=0. The baseline values are integrated to give the total CO₂ (%) contributed by atmospheric levels. The total atmospheric CO₂ (%) is then subtracted from the total CO₂ (%) to give the total CO₂ (%) generated by the cables during the test. It is this value that is divided by the time across which it was integrated to give the average CO₂ (%), as shown in graph C.

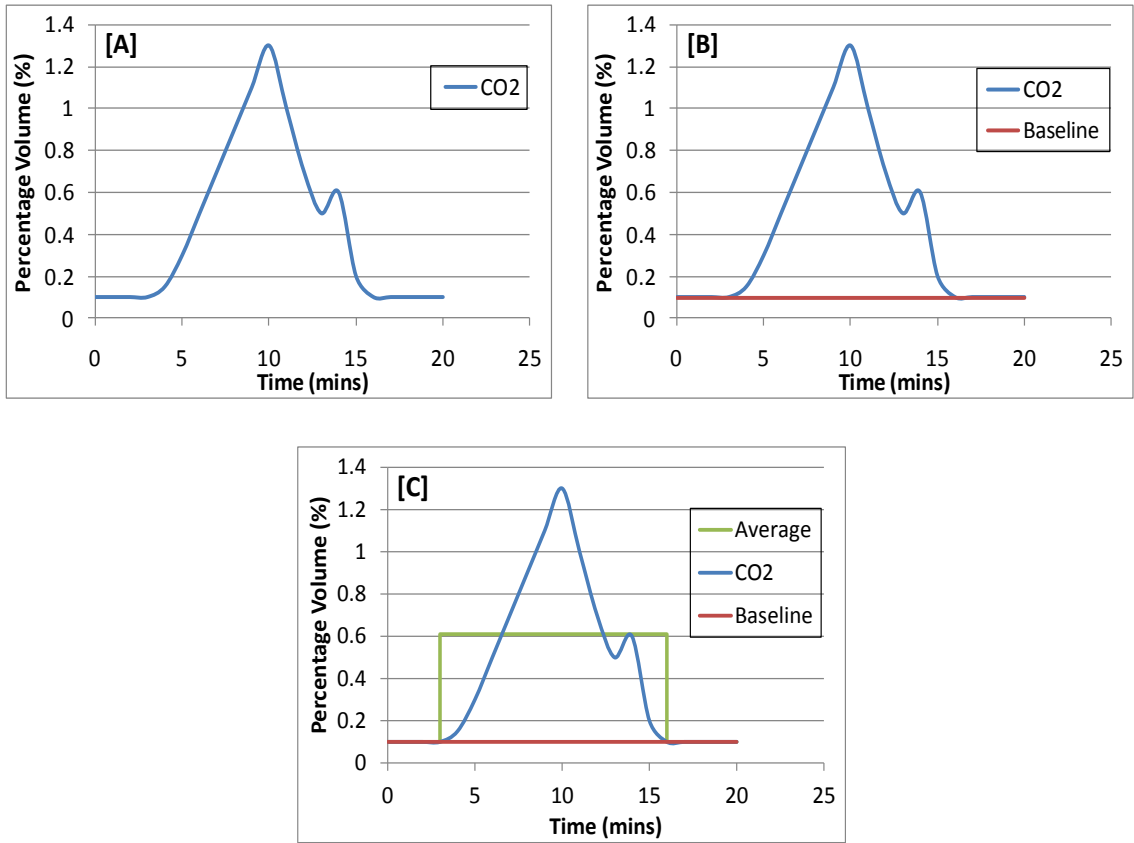


Figure 34 Calculating CO₂ Average (%)

For the CO data, the process is virtually identical, except there is no atmospheric CO, which means that the raw data is plotted and integrated to give the total CO (%) value, Graph A. Graph B shows the average CO (%), which is calculated by dividing the total CO (%) by the time (mins) over which the total CO (%) was calculated. (Figure 35).

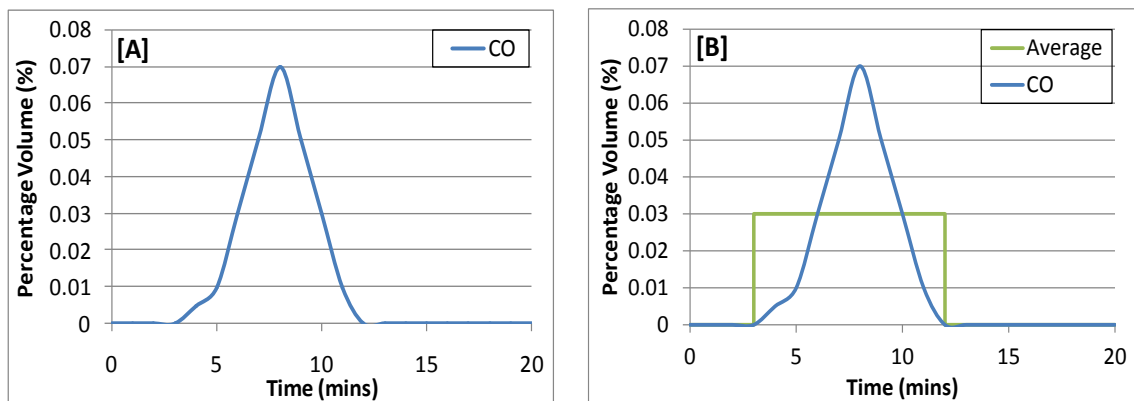


Figure 35 Calculating CO Average (%)

3.1.2 O₂ and Smoke averages.

For O₂ and smoke the methodology differs from those above because the O₂ and smoke measurements are recorded as a decrease in values from their baselines, rather than a rise. As such the value for total amount depleted would require integrating above the curve, which is not possible, thus a work around is required. In [Figure 36](#) graph A shows the raw data being plotted. Graph B shows the raw data and the baseline, the baseline value is set at time=0. Now the area of interest in graph B is now the area between the raw data curve and the baseline curve. Therefore if we subtract the integral of the raw data from the integral of the baseline the resultant value would be that of the area between the curves, which is the value for total O₂ depletion or total transmission, dependent on what data was being analysed. The average is once again calculated by dividing the total area value by the time over which it was integrated, shown in graph C.

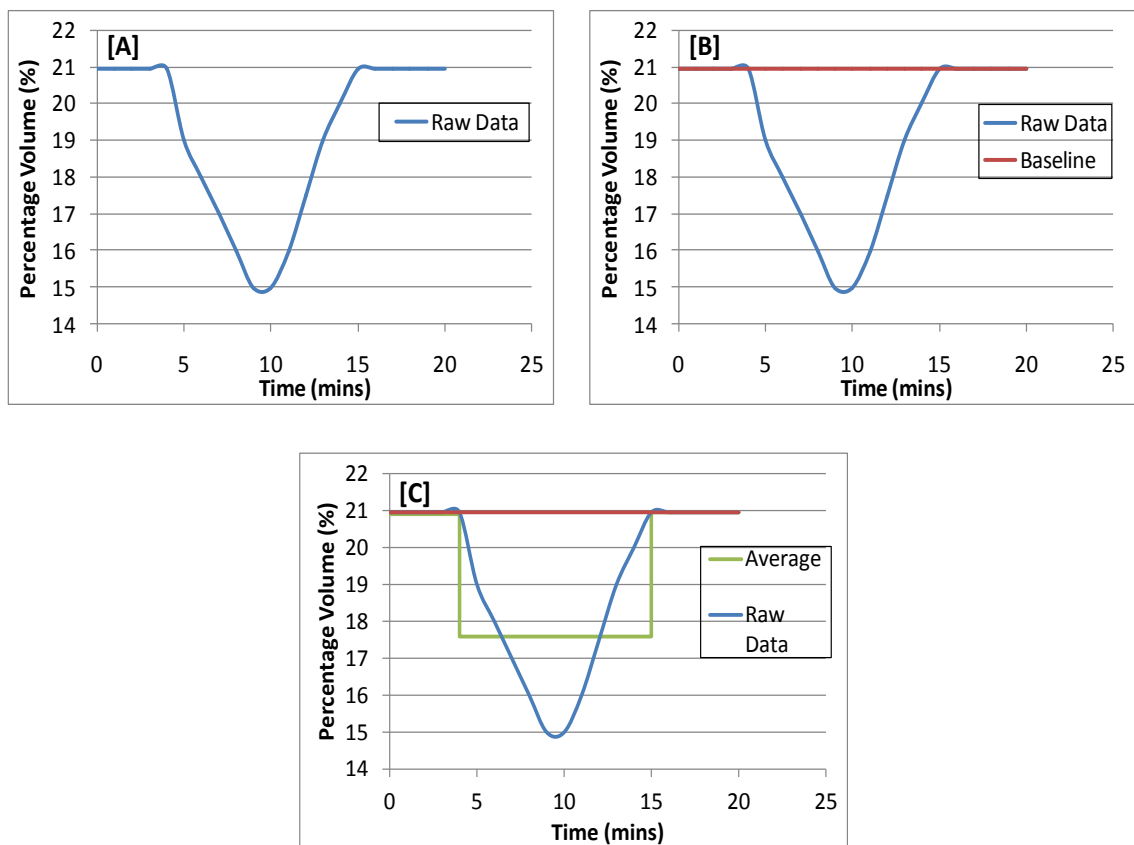


Figure 36 Calculating O₂ and Transmission Values (%)

3.2 CALCULATING MASS LOSS

Even with the average percent for each species in the large-scale test having been calculated, yields for the large-scale data are still not possible to calculate. This was due to the lack of mass-loss data in the large-scale test. For estimating mass loss in the large-scale two methods were employed. The first used the TGA data from [Section 3.4.5](#) however this assumes complete combustion across the entire area of cable exposed to the fire. The second method uses carbon balancing to estimate the mass of cable compound burnt based on the mass of CO₂ produced during the test.

3.2.1 TGA Based Mass Loss

For the cable materials 1 x 2.5 mm² LSOH, and 3 x 1.5 mm² LSOH, data on the length of cable damaged during the burn was provided, and as such the total mass loss was calculated as follows: (using values for 3 x 1.5 mm² LSOH)

Burn length = 1.99 m, Total number of cables = 15

From cable sample preparation the weight of 10.7 cm equals 16.11 g; therefore 1.99 m would weigh 299.62 g, but as there are 15 cables the total weight of cable in the test equals 4494.24 g.

Next we know the percentage by mass of the cables constituent components:

Sheath = 52.7% = 2368.34 g

Bedding = 14.59% = 655.67 g

Insulator = 7.64% = 343.34 g

From the TGA we know the percentage mass loss of each of these components:

Sheath = 50.48% = 1196 g lost

Bedding = 36.66% = 240 g lost

Insulator = 96.16% = 330 g lost

Therefore the total mass loss for the cable during the large-scale test is 1766 g.

However for some samples the length of cable burned during the test was not recorded, so instead the burn length was estimated using photographs taken at the end of the test. In the large-scale test photos both markings along the cable ladder (Figure 37) and a measurement ruler laid alongside (Figure 38) aided in this burn length estimation.



Figure 37 Large-scale Measurement Ruler



Figure 38 Large-scale Ladder Markings

3.2.2 CO₂ Based Mass Loss

For this method neither a burn length nor a photograph of the cable ladder after the test were needed to aid mass loss estimated. The only information needed was the total mass of CO₂ produced during the test, the calculations for which can be seen in a worked example in the first part of [Appendix C](#). [Appendix D](#) outlines the calculations for turning the mass of CO₂ produced into a mass loss value. However in doing so the assumption has to be made that the main polymeric content is poly ethylene (for the LSOH cables) and polyvinyl chloride (for the PVC cables) and that only these two compounds contribute to the production of CO₂, neglecting bedding materials such as CaCO₃. Also assumed is the mass loading, in percent, of the organic and inorganic components.

3.3 CALCULATING YIELDS

To calculate the yield for a given species the percentage fraction has to be converted into a mass. This is done by first converting the percentage into a volume (L) by the equation:

$$\text{Volume of Gas (L)} = \frac{\text{Average Volume (percent)}}{100} \times \text{Total Air (L)} \times \text{Time (s)}$$

Where total air is assumed to 833 L/sec and time represents the time over which the average volume percent was calculated.

Once expressed as a volume the mass of the species can be calculated thus:

$$\text{Mass (g)} = \text{Volume (L)} \times \frac{\text{Molar Mass (g)}}{\text{Molar Volume (L}^{-1}\text{)}}$$

Where molar volume assumes a temperature of 20 °C, a pressure of 101 kPa and that the gas behaves as an ideal gas.

Once obtained, the mass of the gas is divided by the mass loss of the respective cable to give the yield in g/g. A fully worked example for all the species can be seen in [Appendix C](#).

3.4 LARGE-SCALE TEST RESULTS

The results presented in this section are the raw data for all of the different cable types that were testing on the prEN50399-2-1 test rig, also visible on the graphs are the calculated average (%) and the baseline values (%) where appropriate.

3.4.1 prEN50399-2-1 Results

3.4.1.1 1 x 2.5 mm² LSOH

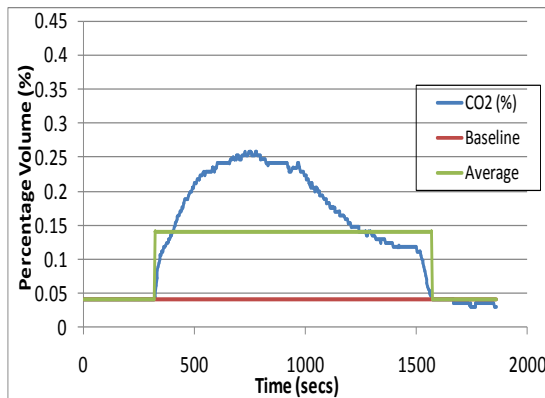


Figure 39 125LSOH Large-scale CO₂ Data

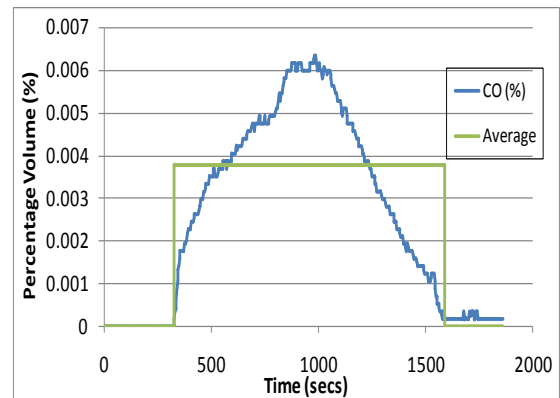


Figure 40 125 LSOH Large-scale CO Data

Figure 39 shows the large-scale data for CO₂. It initially rises steeply to a value of 0.1% after which the rate of increase slows to a value of roughly 0.25%, where it remains fairly steady until around 1000 seconds before it starts to decline, although at a slower pace than it rose until roughly 1500 seconds where it sharply falls off, back to baseline.

Figure 40 shows the CO data from the large-scale test. Like the CO₂ data it rises very quickly to a peak, around 0.006%, where it remains steady, but for less time compared to the CO₂ data. Also it falls quicker, but still experiences a drop off back to baseline around 1500 seconds.

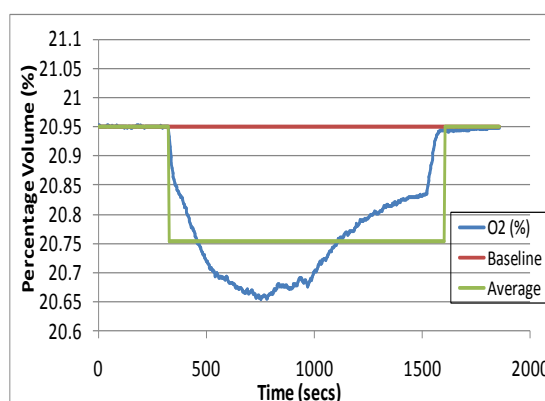


Figure 41 125LSOH Large-scale O₂ Data

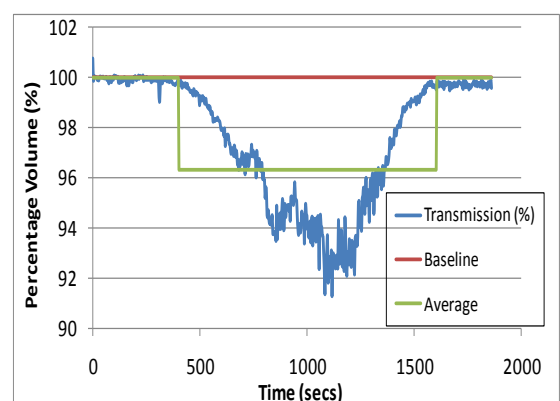


Figure 42 125LOSH Large-scale Transmission Data

Figure 41 shows the large-scale O₂ data. The O₂ drops to a minimum value at approximately 750 seconds, with a value of approximately 20.65%, which is a depletion of 0.3%, matching the combined value of 0.25% CO₂ and 0.06% CO.

Figure 42 shows the transmission data, which shows an overall decreasing trend to a minimum of approximately 92% at roughly 1100 seconds after which it rises back to baseline, at a quicker pace than it fell. The transmission peak coincides with the very end of the CO peak values.

3.4.1.2 3 x 1.5 mm² LSOH

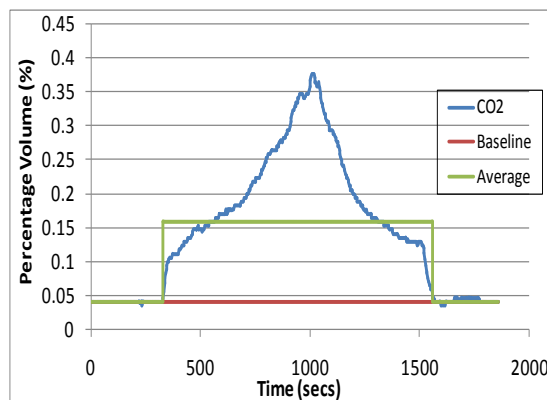


Figure 43 315LSOH Large-scale CO₂ Data

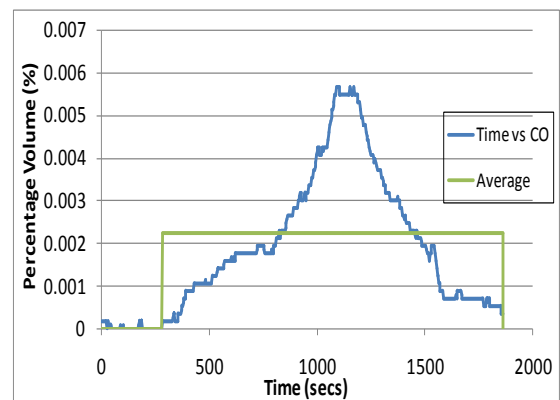


Figure 44 315LSOH Large-scale CO Data

Figure 43 shows the large-scale CO₂ data, the profile of which is almost symmetrical. It rises sharply at first, before continuing to rise, but at a slower rate, it reaches a peak of approximately 0.38% where it immediately starts falling, at a rate similar to that at which it climbed, before sharply falling off to baseline, at roughly 1500 seconds.

The CO data in Figure 44 has a similar profile to that of the CO₂ data, except that after the sharp increase at the beginning, the rate slows down until at approximately 800 seconds the rate increases again. The CO peaks at around 0.00575%, where it levels off briefly, before falling. Again at 1500 seconds the data experiences a sharp decline, except the values don't return to base line but instead level off at around 0.0008%.

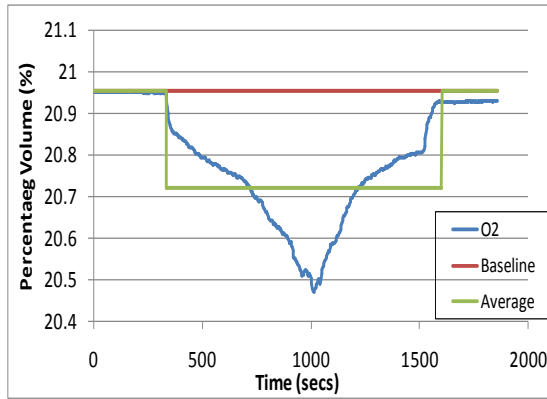


Figure 45 315LSOH Large-scale O₂ Data

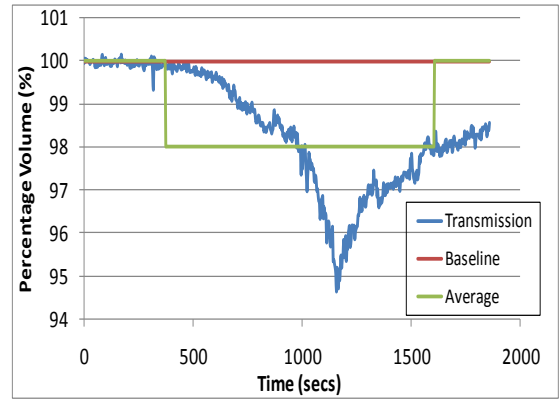


Figure 46 315LSOH Large-scale Transmission Data

Figure 45 shows the O₂ data from the large-scale test, which once again mirrors the profile of the CO₂ data. The O₂ reaches a minimum of 20.45%, giving a peak O₂ depletion of 0.5%, however the addition of the peak CO₂ and CO values only give a total of 0.39%, which would imply that O₂ is being used in some other reaction other than the conversion of the burning cable compound to CO and CO₂. The O₂ data fails to return to baseline, instead levelling off at 20.93%.

Figure 46 shows the transmissions data which starts to fall at around 400 seconds, and continues to fall at an ever increasing rate until it reaches a peak at approximately 94.5% at 1200 seconds before starting to rise again. However the test is ended before the values return back to baseline.

3.4.1.3 FR 4804

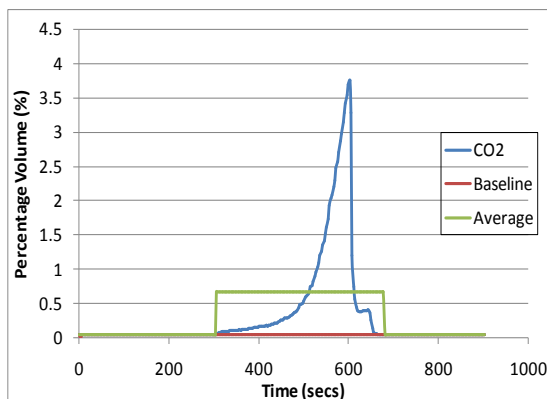


Figure 47 FR 4804 Large-scale CO₂ Data

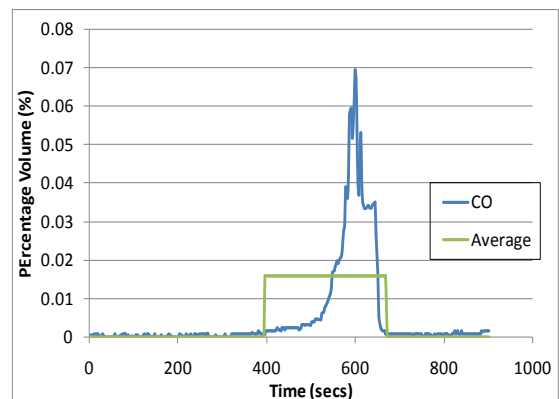


Figure 48 FR 4804 Large-scale CO Data

In Figure 47 the CO₂ data shows almost exponential growth from 300 seconds until its peak of 3.75% at 600 seconds. After which the values plummet, reaching baseline by 680 seconds. The CO₂ data from FR4804 differs markedly from all of the previous CO₂ plots, due to the short length of time it takes to rise to its peak and return to baseline. This results in an almost needle like profile.

The CO data in Figure 48 shows a similar profile to that of the CO₂ data, except that the CO values don't start to really rise until 100 seconds after that of the CO₂. Also when it falls the CO data experiences a small plateau at around 620 seconds, before continuing to fall very rapidly back to baseline. The CO has a peak of 0.07%.

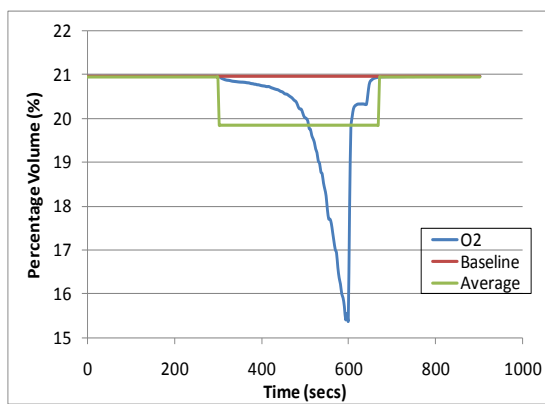


Figure 49 FR 4804 Large-scale O₂ Data

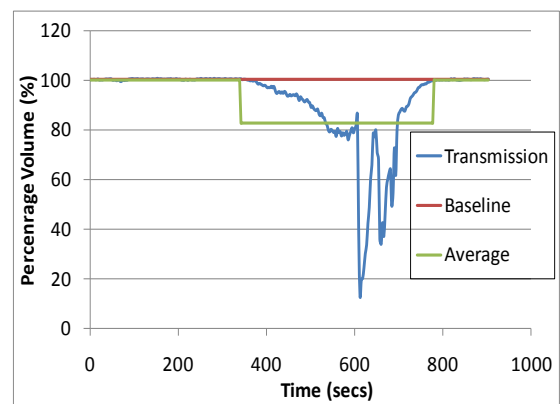


Figure 50 FR 4804 Large-scale Transmission Data

The O₂ data for FR4804 (Figure 49) shows a minimum value of 15.4%. This would give a peak depletion of 5.55%, which once again is more than what is accounted for by the peak CO₂ and CO values combined: a value of 3.82%. The profile of the O₂ data mirrors that of the FR4804 CO₂ data.

Figure 50 shows the transmission data, which starts to fall at around 350 seconds until around 550 seconds where the values briefly level off at around 79%-80% before falling again at 600 seconds at a much increased rate. Such is the rate at which it falls the transmission reaches a minimum of 13% by 612 seconds. It then rises back to 80% just as quickly before dropping to 38%, after which it starts an upwards trend back to baseline.

3.4.1.4 Melos 1006F

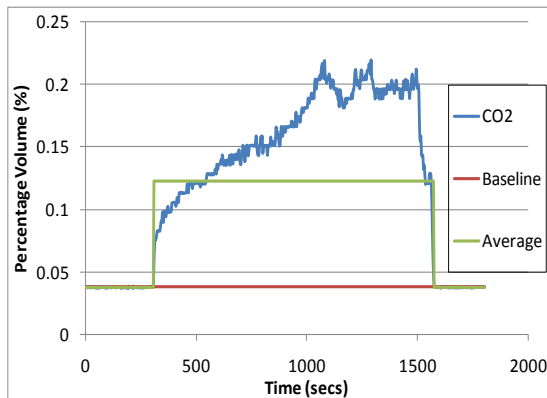


Figure 51 Melos 1006F Large-scale CO₂ Data

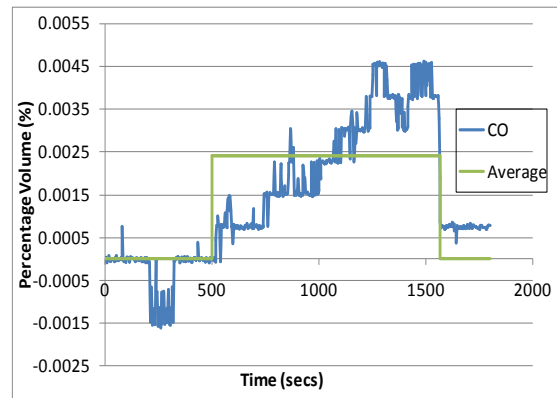


Figure 52 Melos 1006 Large-scale CO Data

When the CO₂ data in [Figure 51](#) begins to rise at 400 seconds and shows an initially sharp increase, before slowing down, but continuing to rise. The rate at which the CO₂ values rise increases at approximately 900 seconds until the CO₂ values reach their peak of 0.22% at just over 1000 seconds. The CO₂ oscillates around the 0.2% mark until 1500 seconds where it drops quickly back to baseline.

The CO data displayed in [Figure 52](#) shows a relative noisy signal line due to the values being so small the instrument used is at the limit of its sensitivity. However the overall trend can still clearly be seen. The CO starts to increase from 500 seconds, steadily rising to its peak of 0.0045%, where it remains briefly before dropping to 0.003% momentarily after which it peaks and troughs rapidly between 0.0045% and 0.004%. The data then falls rapidly at 1550 seconds to 0.0007% where it plateaus and remains until the end of the test.

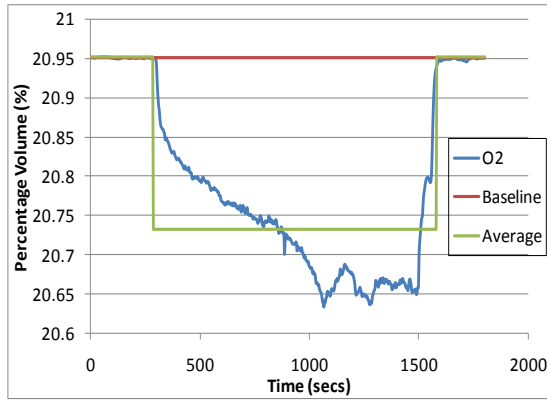


Figure 53 Melos 1006F Large-scale O₂ Data

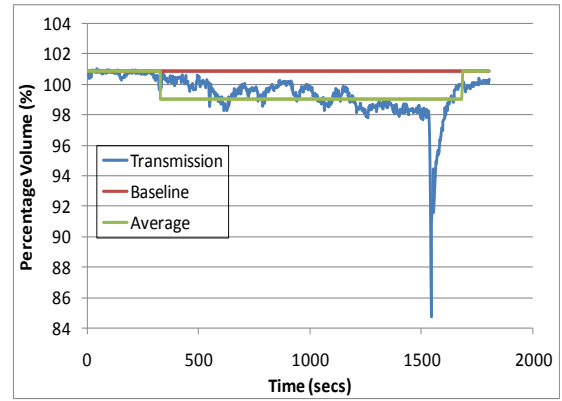


Figure 54 Melos 1006F Large-scale Transmission Data

The O₂ data, (Figure 53), starts to fall at around 400 seconds, falling to a minimum of 20.64% at just over 1000 seconds. The peak O₂ depletion is 0.31%, the combined peaks of CO₂ and CO values give a total percent of 0.2245%, which whilst it does not match, is a lot closer than some of the other cable types.

The transmission data (Figure 54) starts to fall from approximately 400 seconds, and begins a slow decline to a value of 98% at around 1500 seconds, where it dramatically drops to 85% before rising very quickly back to baseline.

3.4.1.5 MGN 09005

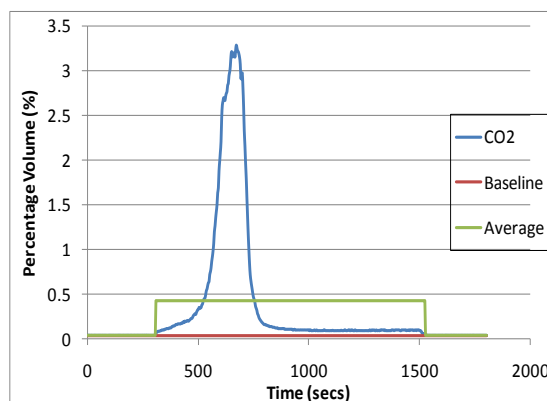


Figure 55 MGN 09005 Large-scale CO₂ Data

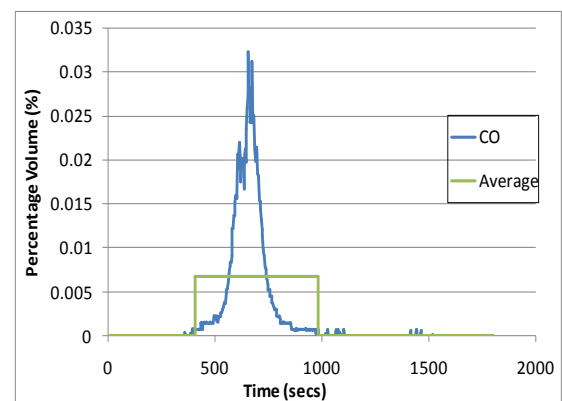


Figure 56 MGN 09005 Large-scale CO Data

The data in Figure 55 shows an almost exponential rise and fall of CO₂. It starts to rise around 300 seconds rapidly increasing to its peak of 3.3% just before 700

seconds. After which it falls before levelling off around 1000 seconds to a value of approximately 0.1%, where it plateaus until 1500 seconds and then falls back to baseline.

The CO data (Figure 56) shows a similar trend to CO₂, rising from around 400 seconds, increasing exponentially to a peak of 0.033% at around 650 seconds, before falling exponentially: returning to zero by 1000 seconds

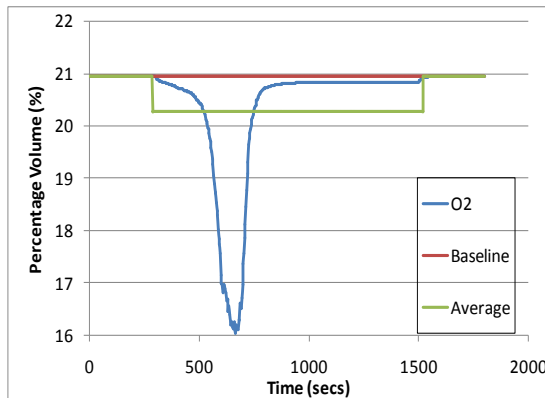


Figure 57 MGN 09005 Large-scale O₂ Data

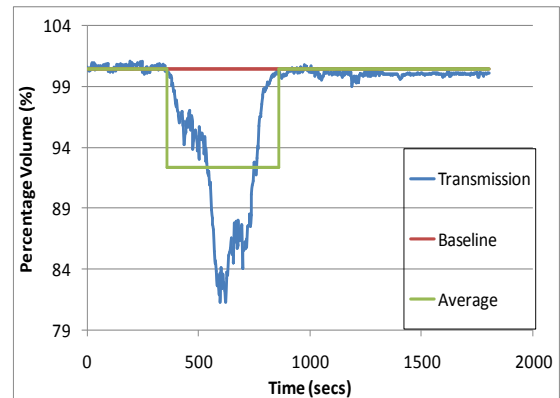


Figure 58 MGN 09005 Large-scale Transmission Data

The O₂ data in Figure 57 starts to decrease at 400 seconds, reaching a minimum of 16% at around 700 seconds, giving a peak depletion of 4.95%. The combined value of the peak CO₂ and CO values is 3.33%, which shows reasonable agreement with the peak O₂ depletion.

Figure 58 shows the transmission data which has a similar profile to that of the O₂ data. The transmission data starts to fall at around 400 seconds, falling to a minimum of approximately 82% around 600 seconds. It then starts to rise, before momentarily decreasing at around 750 seconds, after which it continues to rise back to baseline values.

3.4.1.6 WLS 08006

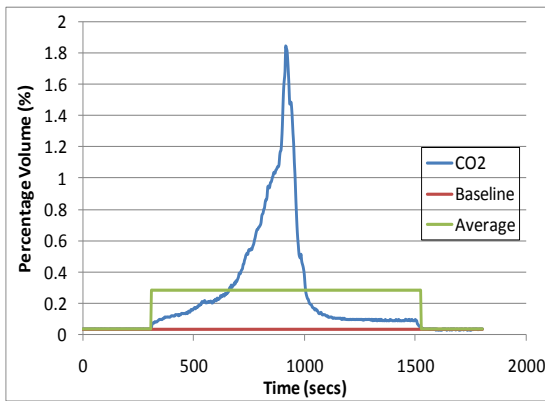


Figure 59 WLS 08006 Large-scale CO₂ Data

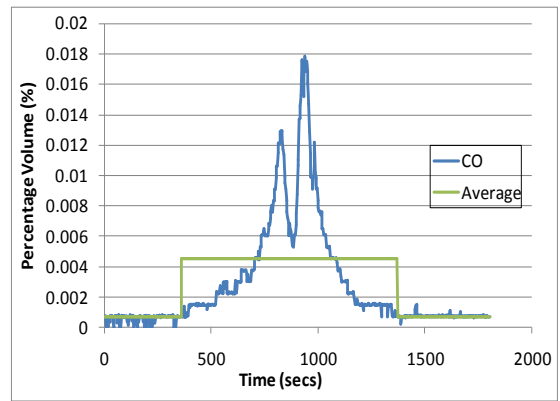


Figure 60 WLS 08006 Large-scale CO Data

The CO₂ as shown in [Figure 59](#) starts to rise at approximately 300 seconds, the rate at which continuously increases, until around 900 seconds where it reaches a peak of 1.85%. It then falls sharply until 1100 seconds where it levels off at a value of approximately 0.1% where it remains steady until 1500 seconds where it falls back to baseline.

[Figure 60](#) shows the CO data, which contains a double peak. The CO starts to rise at around 400 seconds rising to the first peak of 0.013% at around 800 seconds, after which the CO falls to approximately 0.0058% by 880 seconds, before quickly rising to the second, main, peak by 950 seconds with a value of 0.0178%, before sharply falling back to baseline values by 1400 seconds.

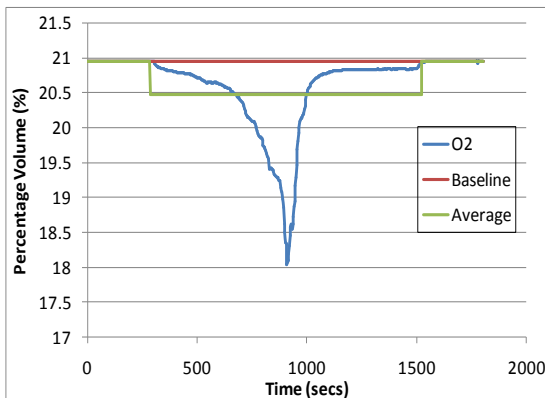


Figure 61 WLS 08006 Large-scale O₂ Data

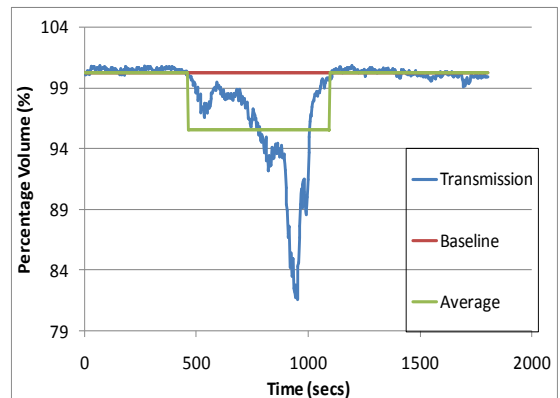
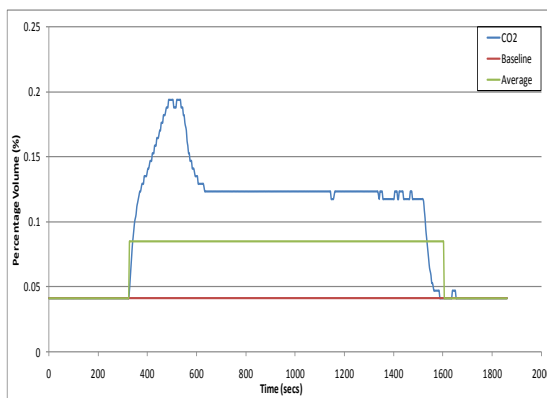


Figure 62 WLS 08006 Large-scale Transmission Data

The O₂ data in [Figure 61](#) matches the profile of the CO₂ data. The O₂ starts to fall at approximately 400 seconds, falling ever quicker until it reaches its minimum of 18% at approximately 900 seconds. It then proceeds to climb quickly until 1100 seconds where it reaches a plateau at a value of approximately 20.8% before returning to baseline values at 1500 seconds. The peak O₂ depletion, 2.95%, shows limited agreement with the sum value of the peak CO₂ and CO values, 1.87%.

[Figure 62](#) shows the transmission data which starts to fall just before 500 seconds, where it falls to a small peak of approximately 97% at 500 seconds before rising to 94% where it follows an overall downwards trend to a minimum of 82% at around 900 seconds, before climbing quickly back to baseline values at around 1100 seconds.

3.4.1.7 1 x 25 mm² PVC



[Figure 63](#) 125PVC Large-scale CO₂ Data

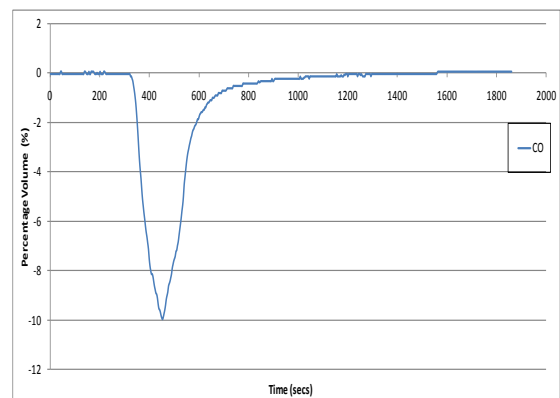


[Figure 64](#) 125PVC Large-scale CO Data

The CO₂ data ([Figure 63](#)) shows the CO₂ rising to a peak 0.19% at approximately 500 seconds, before falling to approximately 0.1075% where it plateaus for the rest of the test before falling back to baseline at approximately 1500 seconds. The large-scale test's profile of a peak at the beginning of a test followed by a region where the value plateaus for CO₂ is exactly what would be expected from a test involving PVC as the conversion of CO₂ is hindered due to the gas phase inhibition caused by the HCl that is evolved from the burning PVC⁴⁵.

[Figure 64](#) shows a very interesting CO graph, as all the values recorded are negative, and of a much greater magnitude that would be expected, the peak being

-10%. Due to these reasons the large-scale CO data can't be used when trying to compare the large-scale data to the small-scale data.

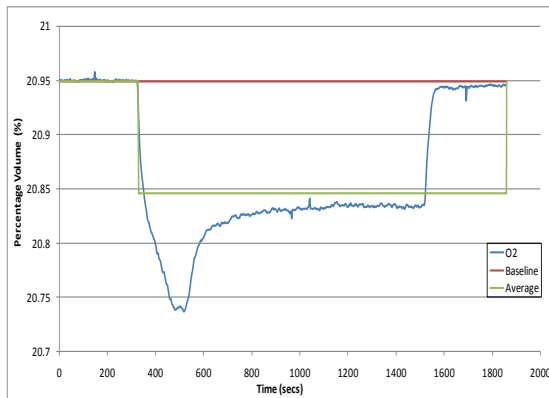


Figure 65 125PVC Large-scale O₂ Data

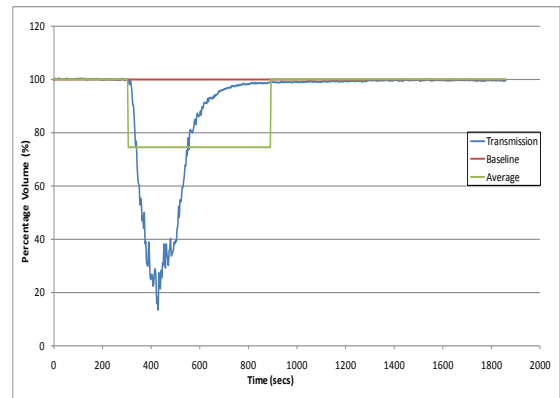


Figure 66 125PVC Large-scale Transmission Data

The O₂ consumed data shown in [Figure 65](#) has a peak value of 20.74%, giving a peak depletion of 0.21%, which concurs with the 0.19% value for the peak CO₂ the only other thing of note about the O₂ data is that when rising back to baseline the values plateau at 20.83% between 880 seconds and 1500 seconds, rather than returning to baseline.

The transmission data ([Figure 66](#)) shows the transmission falling quickly from roughly 300 seconds to a peak of 13% at 430 seconds, before rising equally as quickly back to baseline, until approximately 600 seconds where the rate at which the values rise diminishes until the values do return to baseline at approximately 900 seconds.

Table 21 Large-scale Results Summary

Cable Type	Peak CO ₂ (%)	Avg CO ₂ (%)	Peak CO (%)	Avg CO (%)	Peak O ₂ Depletion (%)	Avg O ₂ Depletion (%)	O ₂ unaccounted for (peak) (%)	O ₂ unaccounted for (Avg) (%)	Peak Smoke (Transmission) (%)	Avg Smoke (Transmission) (%)
125LSOH	0.25	0.14	0.0060	0.0038	0.30	0.22	0.044	0.02	92.0	96.32
315LSOH	0.38	0.16	0.0058	0.0022	0.50	0.23	0.120	0.068	94.5	98.00
FR4804	3.75	0.67	0.0700	0.0158	5.55	1.10	1.730	0.414	13.0	82.73
Melos	0.22	0.12	0.0045	0.0024	0.31	0.22	0.086	0.098	98.0	99.04
MGN	3.30	0.43	0.0330	0.0068	4.95	0.67	1.617	0.233	82.0	92.35
WLS	1.85	0.28	0.0178	0.0045	2.95	0.48	1.082	0.196	82.0	95.50
125PVC	0.19	0.88	n/a	n/a	0.21	0.10	0.02	0.12	13.0	74.39

In [Table 21](#) one of the most noticeable features is how different the results for FR4804, MGN and WLS are from the rest of the cable types. Their CO and CO₂ results are all a power of 10 greater than the rest. The peak O₂ depletion and peak transmission values also differ greatly from the other results. If the CO₂ profiles are examined for FR4804, MGN and WLS, [Figure 47](#) [Figure 55](#) and [Figure 59](#) respectively, they clearly show a similarity between their peak shapes. This would imply that because they all burn in a similar manner that their composition must also be similar.

Examining the profiles for all the large-scale O₂ data shows that they mirror the profile of their respective CO₂ profiles, which is unsurprising given that any O₂ consumed is primarily used to oxidise carbon to either CO or CO₂, and that the amount of CO₂ produced is much greater CO produced.

An interesting comparison would have been that of the peak CO value for the PVC cable compared to those of the non-PVC cables, as the combustion of PVC often produces higher than average amounts of CO under well-ventilated conditions.

3.4.3 TGA

In order to be able to calculate yields from the large-scale data the amount of mass lost during the test has to be estimated and being able to make this estimation requires knowledge of the mass loss of individual components. Micro-scale testing, TGA, was carried out on each component of each cable type. All testing was carried out in an air atmosphere using a heating rate of 10 °C/min up to 900 °C

3.4.4 TGA Results

3.4.4.1 1x2.5 mm² LSOH

The data in [Figure 67](#) shows the three repeat tests for the cable insulating material. It shows that the insulation has a two stage decomposition process. The first decomposition is fairly rapid starting at around 350 °C, and ending approximately 100 °C later. The second decomposition step is much slower,

starting at 450 °C and ending at 700 °C, only losing 3%. From 700 °C onwards the sample becomes stable at 49.3% of the original weight.

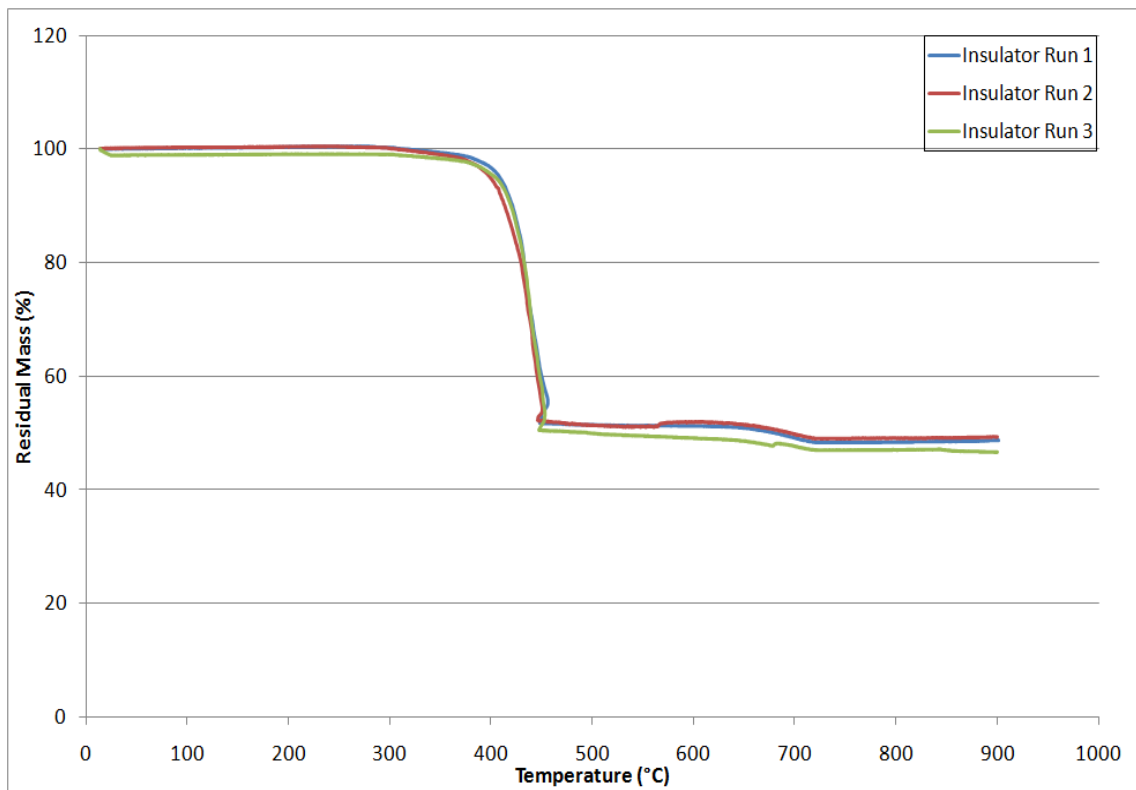


Figure 67 125LSOH TGA Data

3.4.4.2 3x1.5 mm² LSOH:

The TG data shown in Figure 68 differs from the rest of the materials tested as it contains a separate bedding component. Both the sheath and the bedding material show two stage decomposition. The sheathing material starts to decompose at 400 °C, losing approximately 48% of its mass by 470 °C. The second decomposition stage, is much slower than the first, running between 470 °C and 720 °C but losing only a further 2.5% of the total mass. After 720 °C the sheath becomes a stable residue, 49.51% of the original mass. The bedding material follows a similar profile to the sheathing material, but its decomposition starts earlier at roughly 300 °C, with the first stage ending at 450 °C, during which 30.85% of the total mass is lost. The decomposition transitions straight into the second decomposition stage, which progresses at a much slower rate than the initial decomposition, the second decomposition stage ends at approximately 750 °C, during which only a further 1.64% is lost. Once more the decomposition curve

levels out after the third decomposition stage, leaving a residue that is 64.34% of the original mass. The insulator materials each show a three stage decomposition. The first stage starts around 270 °C, losing roughly 4% before transitioning into the second decomposition step, which occurs between 350 °C and 400 °C. The second stage is where the vast majority of mass loss occurs, approximately 92% by the time the temperature reaches 490 °C. The third and final stage occurs between 490 °C and 520 °C where a limited 0.8% of mass is further lost. The residue is stable from 520 °C onwards and accounts for just under 4% of the total mass.

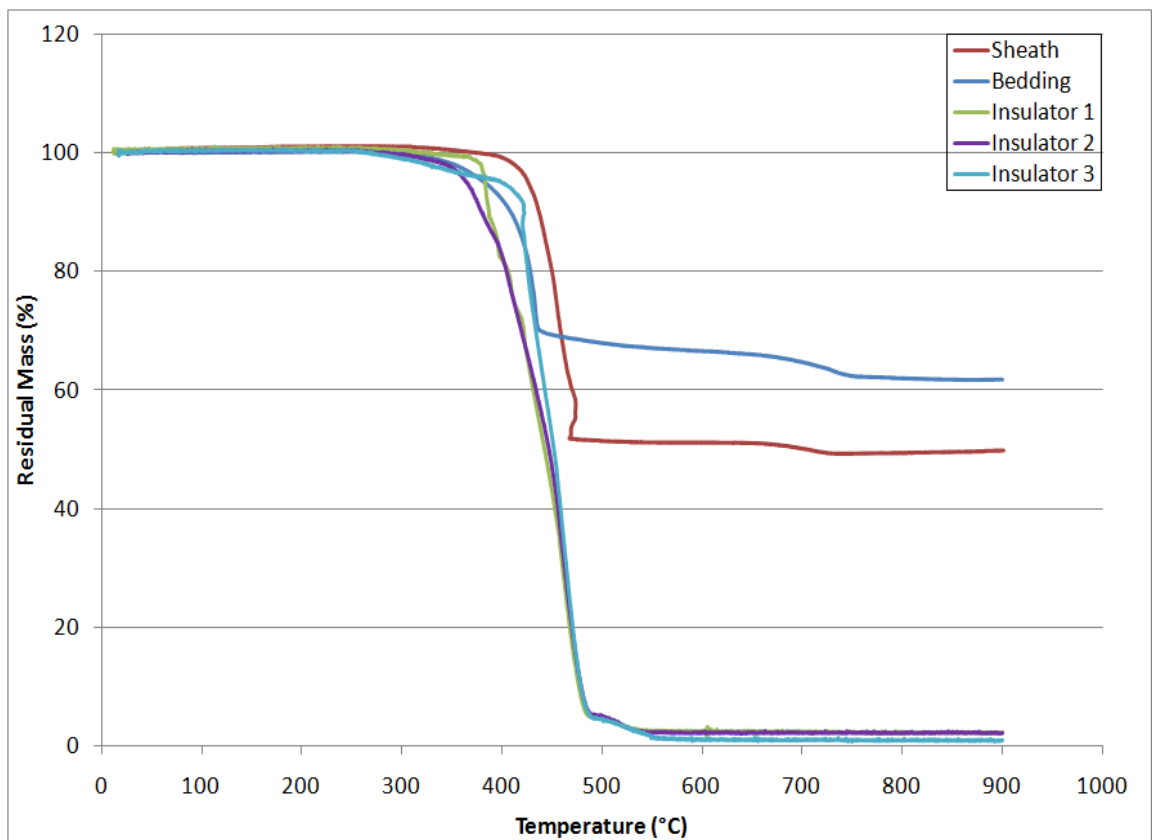


Figure 68 315LSOH TGA Data

3.4.4.3 FR 4804:

Figure 69 shows the decomposition curves for the sheath and all three insulators of FR 4804. All three insulators shows a 3 step decomposition curve, starting at approximately 270 °C, where it loses mass slowly, losing roughly 7% by approximately 400 °C. The second decomposition step is where most of the mass is lost, it occurs roughly between the temperatures of 400 °C and 500 °C, the amount of mass loss that does occur is approximately 87% of the total. The third

decomposition step is a slow mass loss, similar to the first decomposition step, where between the temperatures of 500 °C and 600 °C an approximate further 4% is lost. From 600 °C onwards the insulating material remains stable, leaving behind a residue that is roughly 0.7% of the original mass. The sheathing material shows a 3 stage decomposition process, the first stage occurs between 280 °C and 400 °C, approximately, losing roughly 12% of its mass. The rate of mass loss then increases into the second decomposition step which starts at roughly 400 °C and ends at approximately 490 °C where a further 50% of the total mass is lost. The second decomposition step is where the most mass is lost. Unlike the insulator material the sheath does not transition straight into the third decomposition step from the second, instead the sheath remains stable until roughly 670 °C, after which it starts to lose mass, losing approximately 11% between 670 °C and 750 °C. After 750 °C the material remains stable at a percentage weight of 25.64% that of the original mass.

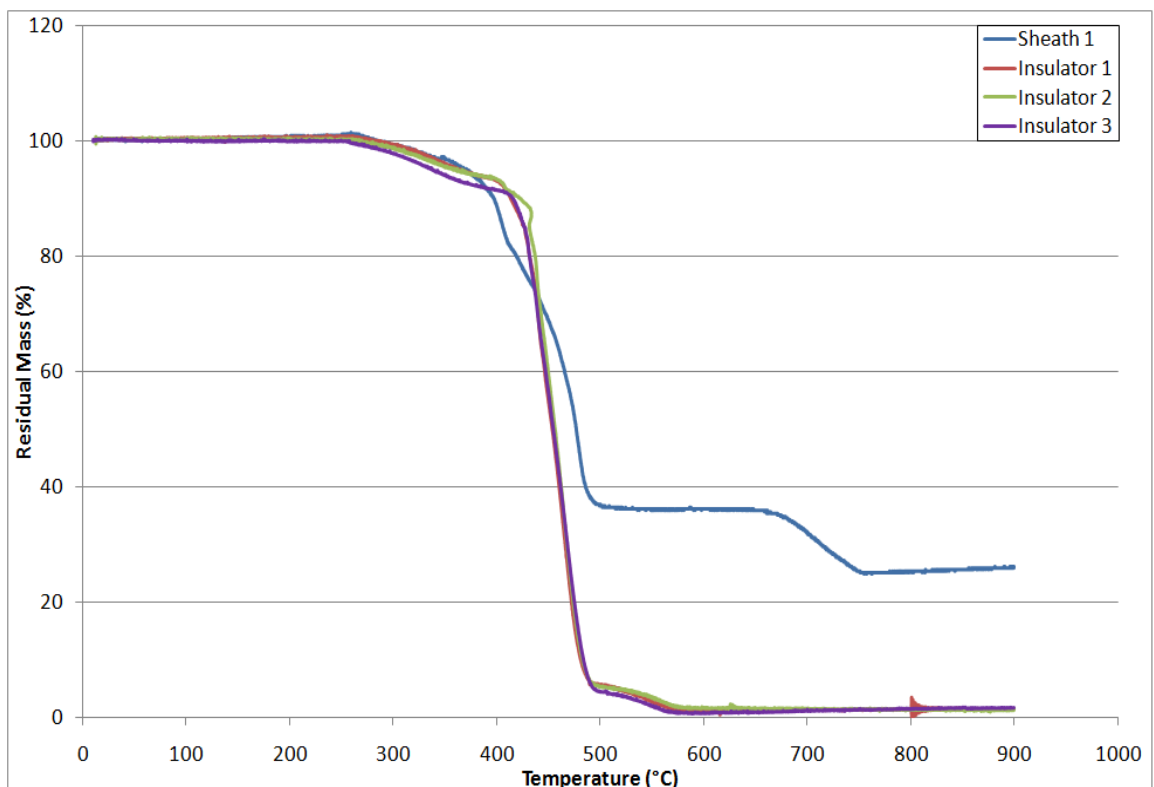


Figure 69 FR 4804 TGA Data

3.4.4.4 MGN 09005

Figure 70 shows the TGA data for the sheath and all three insulators. The sheath shows 3 decomposition steps. The first step starts at approximately 260 °C, losing weight relatively slowly, until 420 °C, where the second decomposition process starts. The second decomposition step is much more rapid than that of the first, losing just over 50% of the sample's total mass by 480 °C. The sample then becomes stable until approximately 620 °C where it starts losing mass until approximately 750 °C, after which it remains stable around 38%. The insulator materials also show 3 step decomposition processes. The first stage starts at approximately 270 °C; lasting till 400 °C losing 8.5% of its mass at a relatively slow rate. At 400 °C the decomposition curve transitions into the second stage where the mass loss rate increases significantly. The second stage is where the majority of the sample's mass is lost; MGN insulators lose roughly 85% of its mass in the second stage. The third stage starts where the second ends at approximately 500 °C, during the third stage approximately 4% mass is lost at a rate similar to that in the first stage. After 570 °C the sample stops decomposing and has a stable residue that is approximately 2% of the original mass.

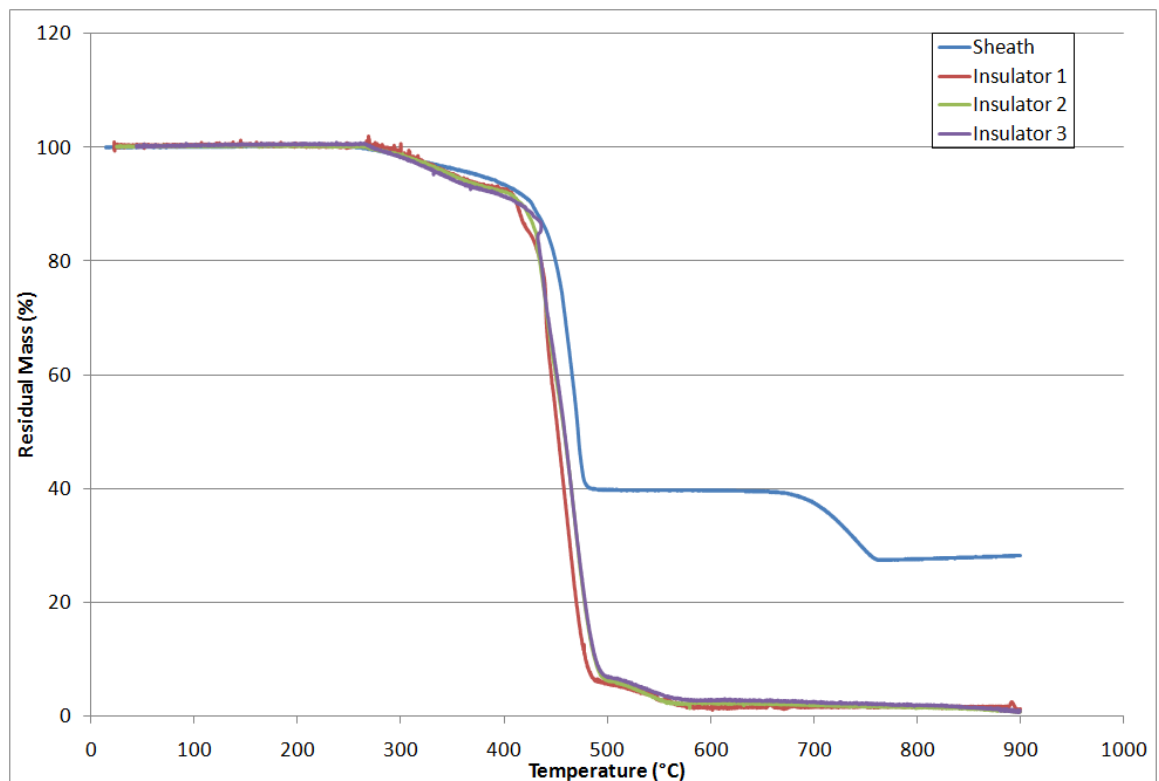


Figure 70 MGN 09005 TGA Data

3.4.4.5 Melos 1006F

The sheath decomposition in [Figure 71](#) shows a two stage decomposition, with no intermediates. The first stage occurs between 250 °C and 380 °C, with an associated mass loss of 41.8%. The decomposition then transitions into the second decomposition step, which ends at roughly 550 °C, with an associated mass loss of roughly 11%. After 550 °C the remaining material is stable at 47.16% of the original mass. The insulator material has similarly has three stages of decomposition for all insulators. Decomposition starts at roughly 250 °C, losing approximately 8 % by 400 °C at which point the decomposition transitions into the second stage, which is between 400 °C and 480 °C and accounts for the largest contribution to mass loss out of the three stages: approximately 78.5%. The third and final decomposition stage occurs between 480 °C and 580 °C and has an associated mass loss of approximately 12%. From 580 °C onwards the insulating material is stable, having a mass that is 1.41% that of the original.

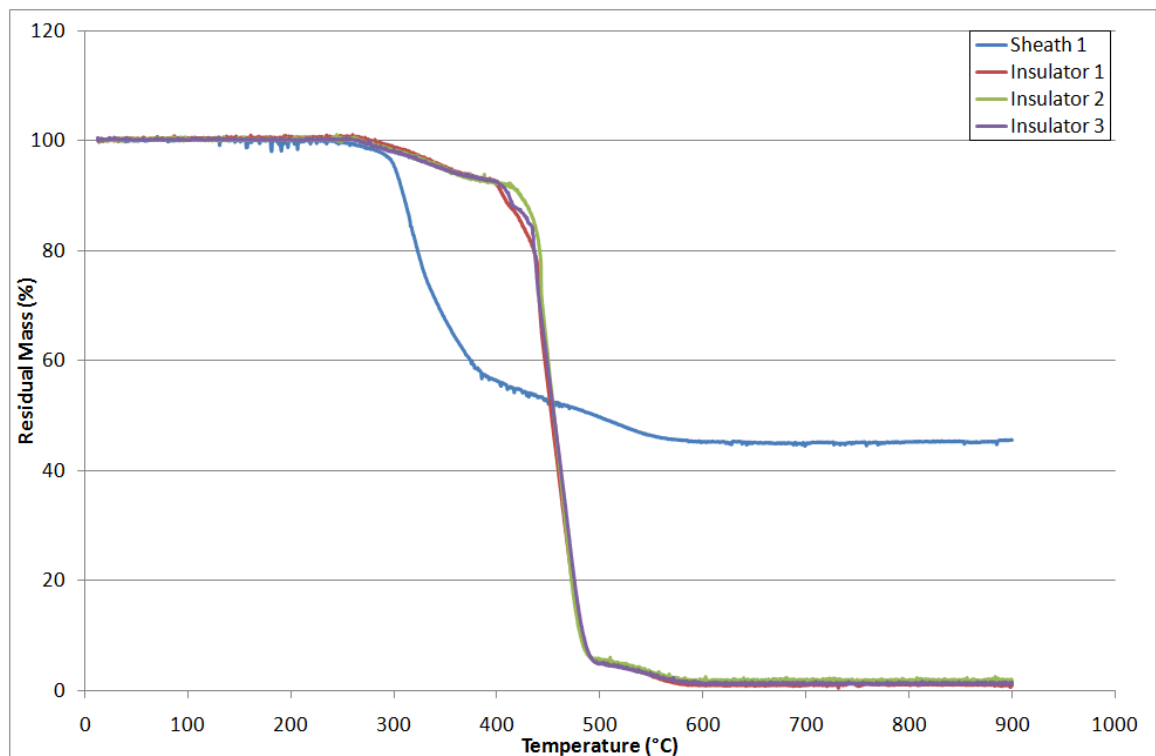


Figure 71 Melos 1006F TGA Data

3.4.4.6 WLS 08006

The TGA data in [Figure 72](#) shows that once again the insulating materials all have three stage decompositions. The insulating materials start to decompose at

280 °C, losing mass slowly, approximately 7%, until 410 °C where the second decomposition step begins and the insulating materials quickly lose mass, losing a further 88.7% of its total by 490 °C, at which the third decomposition step begins where the insulators lose a final 3.15% by approximately 580 °C, after which all that's left is stable residue. The sheath material starts to decompose around 230 °C losing approximately 28.2% of the total mass by approximately 330 °C. The second stage of decomposition occurs roughly between 330 °C and 420 °C where an approximate 24% of mass is lost. The decomposition transitions straight into the third and final stage of decomposition which ends at roughly 550 °C, where the decomposition curve levels out showing the sheath leaves a stable residue that is 44.4% of the original mass.

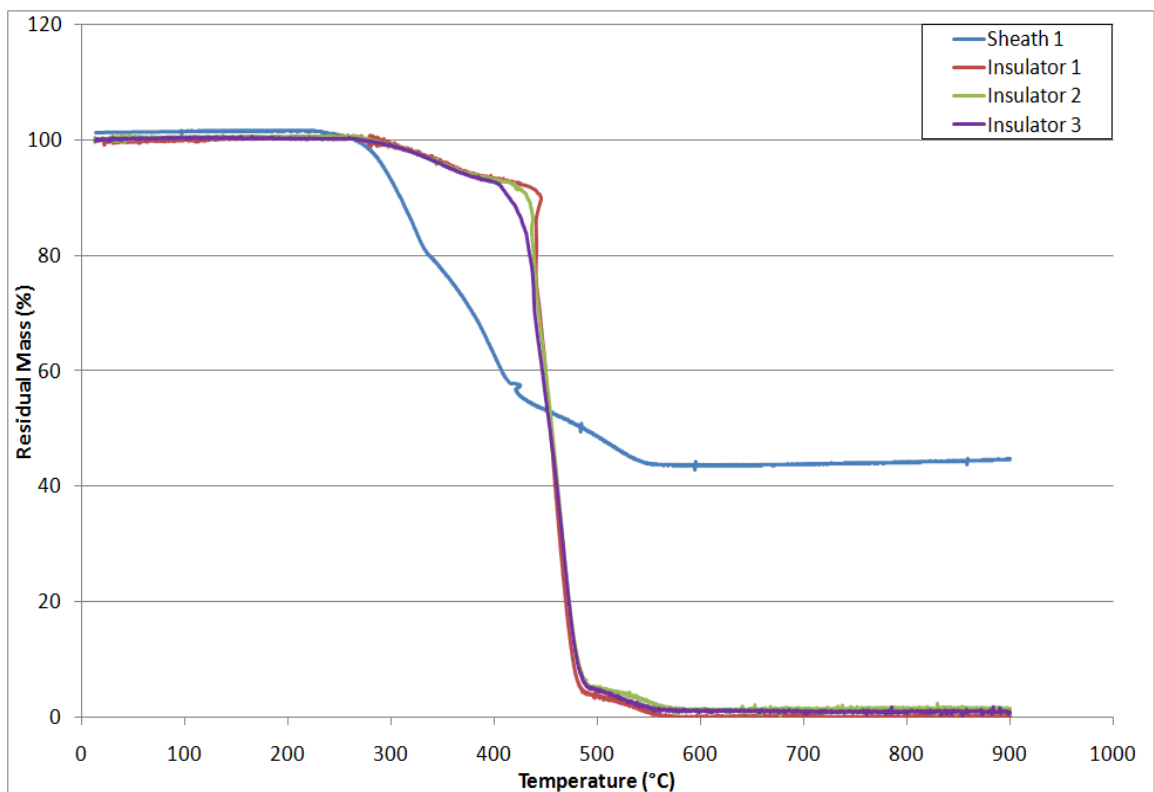


Figure 72 WLS 08006 TGA Data

3.4.4.7 1x25 mm² PVC

The TGA data in Figure 73 shows a decomposition process involving 5 stages. The first stage starts at approximately 200 °C, just under half of the original mass is lost in this stage, which transitions into the second stage at approximately 325 °C. During second stage there is much less mass loss, only 10% of the original

mass, between 325 °C and ≈450 °C. The third stage occurs between approximately 450 °C and 525 °C, and loses roughly another 10% of the total mass, akin to the mass loss in the second stage. The fourth stage lasts the longest, occurring between 525 °C and 700 °C, and again loses approximately 10% of the original mass. The fifth and final stage starts at 700 °C and ends at 775 °C and accounts for a loss of roughly 5% of the original mass. After 775 °C the sample becomes stable at 26.94% of its original mass.

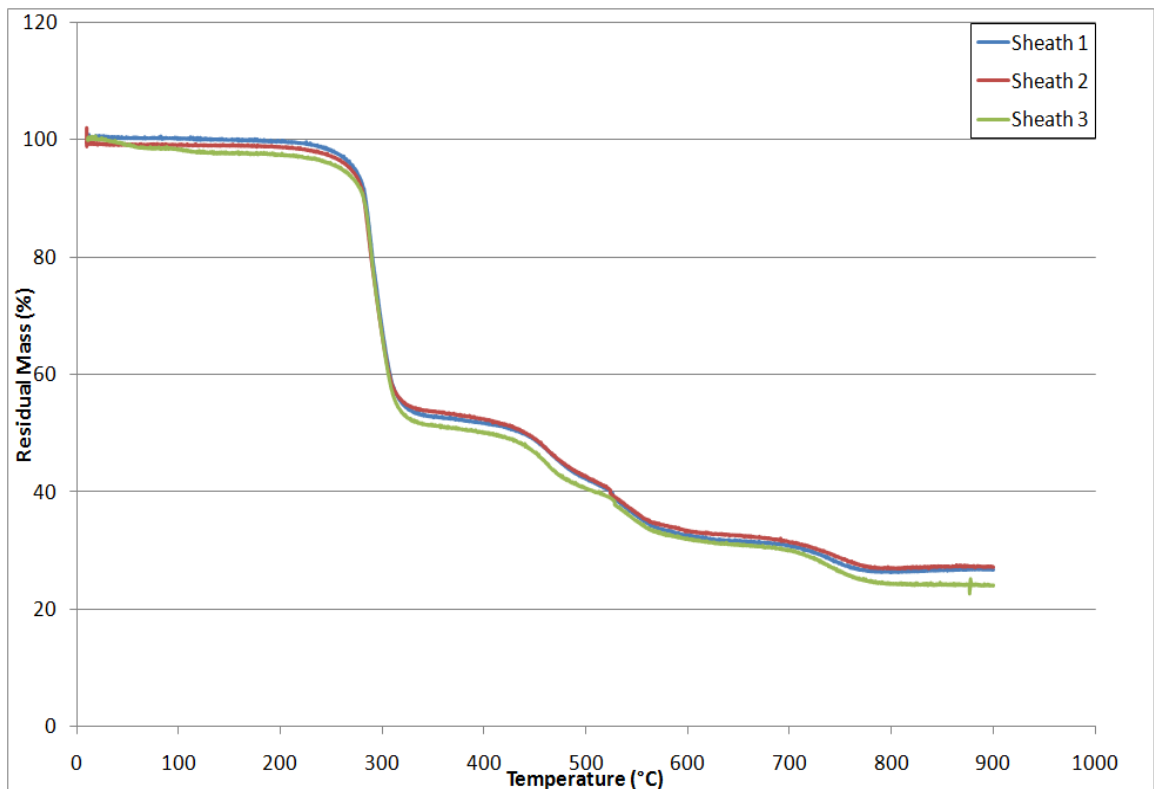


Figure 73 125PVC TGA Data

3.4.5 TGA Summary

The TGA data shows a remarkable similarity between the cable types WLS 08006 and Melos 1006F, and also between MGN 09005 and FR 4804. All of the cables have insulators that decompose in very similar ways, implying that the materials used are very similar if not the same. The sheath materials for WLS and Melos both contain hydrate sheaths, which would explain the similarities between the two, likewise the sheath materials for MGN and FR also share similarities: they

are both polyethylene based and contain approximately the same percentage of chalk.

Table 22 Percentage Mass Loss of Cable Components

Cable Type	Constituent	Percentage Mass Loss
1x2.5 mm ² LSOH	Sheath	51.7
3x1.5 mm ² LSOH	Sheath	50.49
	Bedding	36.66
	Insulator	96.16
MGN 09005	Sheath	28.07
	Insulator	98.52
Melos 1006F	Sheath	54.84
	Insulator	98.59
FR 4804	Sheath	74.36
	Insulator	98.31
WLS 08006	Sheath	55.58
	Insulator	98.85
1x25 mm ² PVC	Sheath	73.06

3.4.6 Burn Length Results

As previously mentioned for the cable materials: FR 4804, Melos 1006F, MGN 09005 and WLS 08006, the large-scale data didn't contain any measurements for mass loss or burn length (Section 3.2). However they did take photographs of the cable ladder before, during and after the test, due to which the burn length damage can be estimated, which combined with the TGA data can be used to estimate mass loss.

3.4.6.1 FR 4804

The large-scale photo (Figure 74) shows the entirety of the cable length was burnt. Unfortunately the scale written on the side of the ladder is not very clear in the photo, which makes it difficult to estimate the length of cable involved. However

the dimensions for the test rig are available in IEC 60332-3⁶³, so combining the photographic data and the dimensions for the test ladder allowed the burn length to be estimated.



Figure 74 FR 4804 Large-scale Test Photo

3.4.6.2 Melos 1006F

The large-scale photo (Figure 75) shows that the damage length for Melos is not the entire length of the cable, nor is it uniform across the cable ladder, making burn length estimation difficult. Thus it was decided that the most accurate way to try and estimate the total burn damage length would be to estimate the burn damage length for each cable and then sum the values. The number of photos provided ensured that all parts of the cable ladder were photographed, and the scale was visible on all photos, enabling relatively precise measurements of burn damage length.

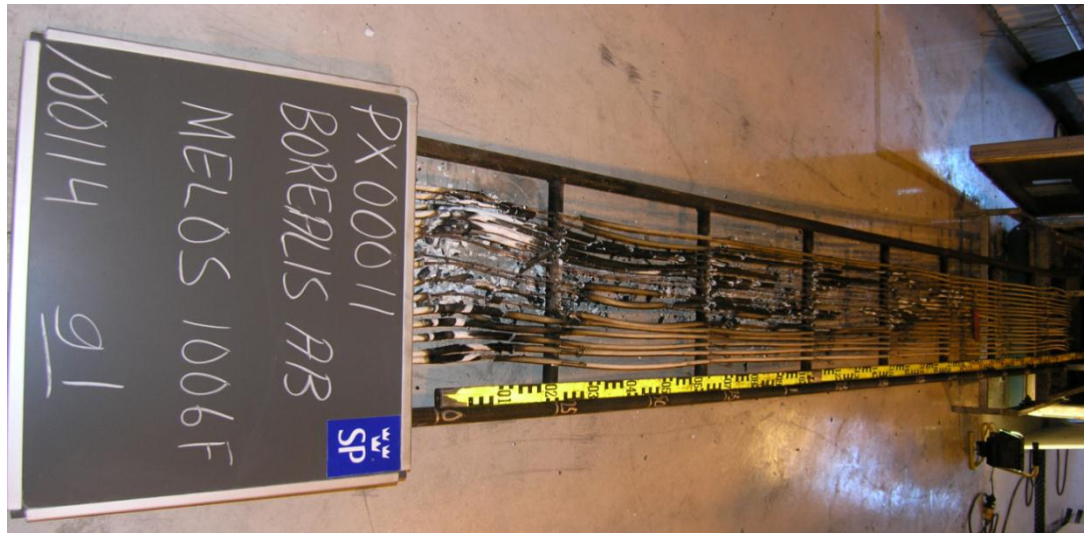


Figure 75 Melos 1006F Large-scale Photo

3.4.6.3 MGN 09005

Figure 76 shows that the MGN cable burnt along its whole length, across the entire cable ladder, as happened with FR 4804. Using the photo and the test rig dimensions the damage length was estimated.



Figure 76 MGN 09005 Large-scale Photo

3.4.6.4 WLS 08006

Figure 77 shows that again all of the cable has been burnt along all of its length. So once more the damage length was calculated using the dimensions of the cable ladder from the rig specifications.



Figure 77 WLS 08006 Large-scale Photo

3.4.7 Burn Length Summary

All of the burn lengths for the different cable types have been recorded in [Table 23](#).

Table 23 Large-scale Total Burn Length

Cable Type	Total Burn Length (m)
1 x 2.5 mm ² LSOH	32.85
3 x 1.5 mm ² LSOH	29.85
MGN 09005	59.50
Melos 1006F	28.00
FR 4804	59.50
WLS 08006	66.50
1 x 25 mm ² PVC	12.90

3.4.8 Estimated Mass Loss in Large-scale Test.

3.4.8.1 TGA Based

The TGA data from [Section 3.4.5](#) was combined with the burn length estimates ([Section 3.4.7](#)) to give the estimated total mass loss in the large-scale test as shown in [Table 26](#).

Table 24 TGA Based Mass Loss Estimation in Large-scale Test

Cable Type	Total Mass Loss in Large-scale Test (g)
1 x 2.5 mm ² LSOH	1509.83
3 x 1.5 mm ² LSOH	1766.30
MGN 09005	3101.34
Melos 1006F	1795.06
FR 4804	3150.14
WLS 08006	2264.65
1 x 25 mm ² PVC	597.19

The table shows similarities between cable types MGN, FR, and WLS, as found previously when analysing large-scale CO₂ results, which reinforces the hypothesis that they have similar compositions. The large differences in the total mass loss between cable types enforce how important normalising the yield data is for obtaining reliable data.

3.4.8.2 CO₂ Based Mass Loss

Table 25 shows the summary for the CO₂ based mass loss calculations.

Table 25 CO₂ Based Mass Loss Estimation in Large-scale Test

Cable Type	Total Mass Loss in Large-scale Test (g)
1 x 2.5 mm ² LSOH	2855.10
3 x 1.5 mm ² LSOH	3165.76
MGN 09005	8364.55
Melos 1006F	2511.47
FR 4804	4026.22
WLS 08006	5596.44
1 x 25 mm ² PVC	6984.39

The mass loss displayed in Table 25 differs greatly from that in Table 24, this shows the potential problems in trying to estimate burn length from photographic evidence

and furthermore from assuming that the cable material in that burn length is all completely burnt. However it should not be forgotten that there were many assumptions made in calculating mass loss from CO₂, not least being that the polymeric material is PE and only the PE content contributes to CO₂ production.

3.4.9 Yield Results

With the estimated mass loss for the large-scale tests calculated the large-scale data provided (Section 3.4.2) could be turned into yields, thus enabling the data between scales to be compared.

3.4.9.1 CO₂ Yields

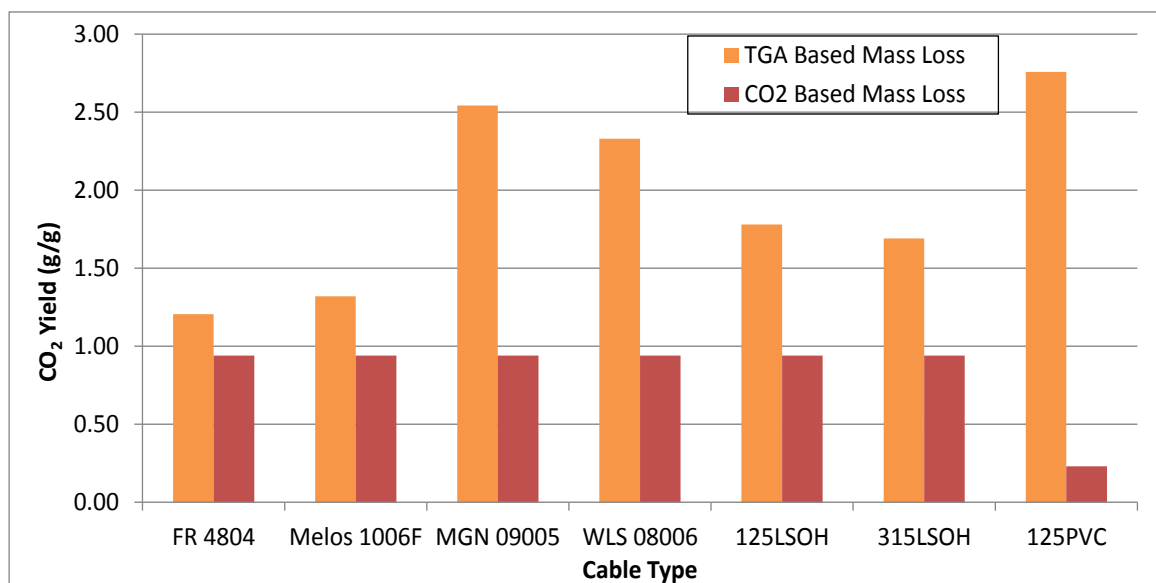


Figure 78 Large-scale CO₂ Yields

For the TGA based mass loss data, aside from the PVC cable, the large-scale CO₂ yields (Figure 78) appear to split into three groups; FR 4804 and Melos 1006F both show similar results, MGN 09005 and WLS 08006 are similar to one another and 125LSOH and 315LSOH are both similar. In terms of magnitude PVC shows the highest yield, whilst FR and Melos have the lowest. Of note is that previous to Figure 78 FR 4804, MGN 09005 and WLS 08006 have all displayed results similar to one another, whereas here the value for FR 4804 is approximately half of that of MGN and WLS. A probable cause of this apparent discrepancy can be traced back to the

large-scale CO₂ data for FR 4804. Whilst the peak values between FR 4804 and MGN may have been similar, the time over which the CO₂ was averaged was not. The time period used to average the results for FR 4804 was under half of that for MGN 09005, hence the yield being approximately half.

The CO₂ based mass loss yields display the same value for all cable types, except for PVC. The PVC yield is different because its main polymer is assumed to be PVC whereas the other cables assumed the main polymer to be PE. All the assumed PE polymers display the same yield due to a by-product of the methodology used to calculate them. The CO₂ based mass loss uses the same calculation to estimate the mass of polymer burnt to generate that mass loss from the mass of CO₂ burnt, thus when dividing the mass of CO₂ by the mass loss a fixed ratio will occur for those cables with the same assumptions.

3.4.9.2 CO Yields

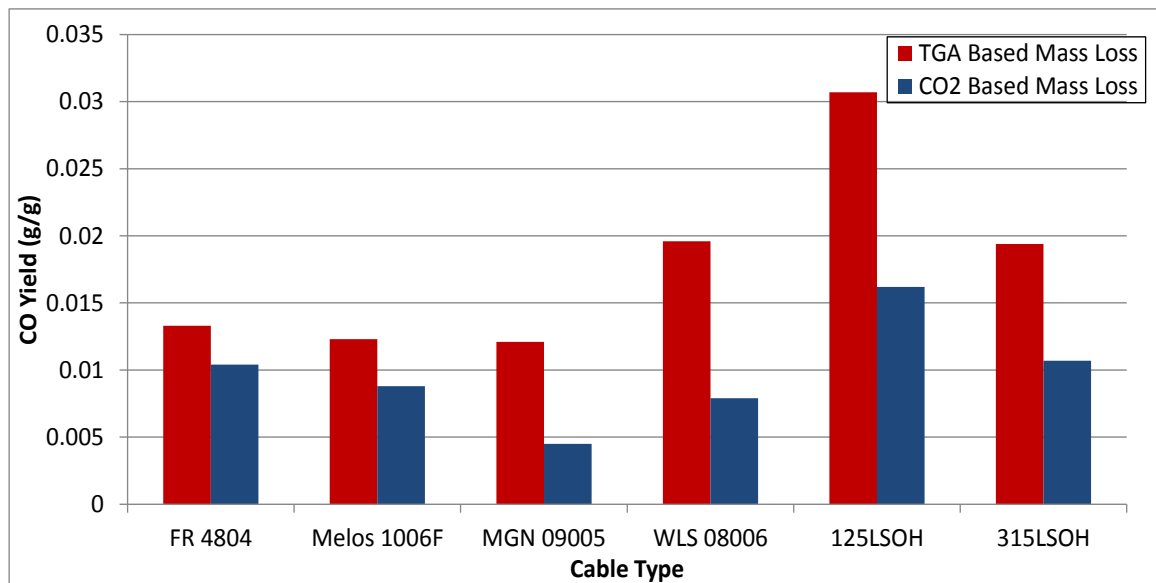


Figure 79 Large-scale CO Yields

The large-scale CO yields (Figure 79) would be expected to mirror those of the large-scale CO₂ yield, which they do to some extent. There is an overall trend that when the CO₂ data increases or decreases from one cable type to the next that the CO data does the opposite, except for 315LSOH. The CO₂ yield of 315LSOH is less than that of 125LSOH therefore the CO value should be higher but it is not. Also the magnitude of change is not mirrored correctly, i.e there is a large difference

between the CO₂ values of Melos and MGN, thus there should be a similarly large change between the CO yields, but there is not. The PVC data is excluded from Figure 79 as the raw PVC data was entirely negative, resulting in an inability to rely on it to calculate a large-scale yield.

The CO₂ mass loss based yields for CO are, unlike the CO₂ yields, usable, they don't suffer from the calculation based problem as the CO₂ yields. The CO₂ based mass loss mirrors the trends displayed by the TGA based mass loss. However the yield values are significantly reduced, in some cases, MGN and WLS, the values are less than half of that for the TGA based mass loss

3.4.9.3 O₂ Consumed Yields

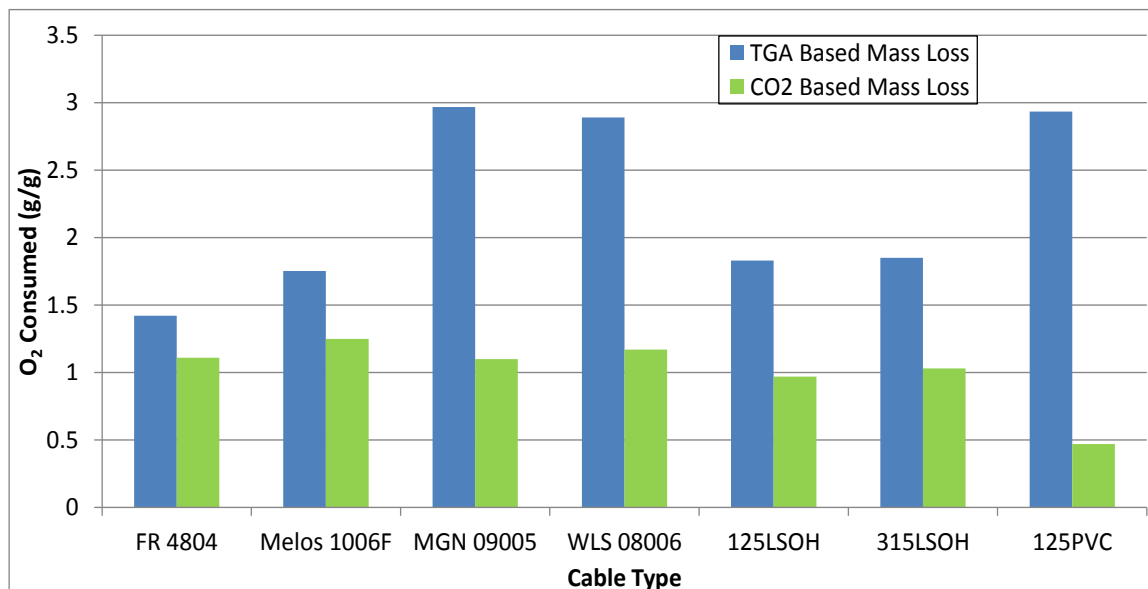


Figure 80 Large-scale O₂ Consumption

The O₂ consumption data (Figure 80) matches the trend patterns of the CO₂ yield data for all except the 125LSOH and 315LSOH, which show a slight deviation. They differ in the fact that the oxygen consumption for 315LSOH is higher than 125LSOH, whereas in terms of CO₂ yields 125LSOH is greater than that of 315LSOH.

Like the CO data the O₂ consumed yields (based on CO₂ mass loss) mirror the trend of the TGA based mass loss with the exception of MGN 09005. Once again the values for the CO₂ based mass loss can be less than half of that of the TGA based mass loss yields, extending to as little as 1/6th of the TGA based mass loss yield for 125PVC.

With both sets of yield and O₂ consumption data calculated, the two were compared to try and seek a correlation between them.

4 COMPARISON OF LARGE AND SMALL-SCALE DATA

With yield results calculated for both scales the results could be compared to one another in order to search for any correlation between the two scales. The comparison between scales was carried out using a variety of different methods to maximise the chances of establishing a correlation.

4.1 EQUIVALENCE RATIO

The testing carried out on the steady state tube furnace was done across a range of ϕ values. This enables the yields for CO, CO₂, and O₂ consumed to be plotted against the ϕ value associated with that test. Equivalence ratio is calculated according to [Equation 5](#), a fully worked example is available in [Appendix B](#).

$$\phi = \frac{m_{loss} \times \Psi_o}{O}$$

[Equation 5 Calculating Equivalence Ratio](#)

The large-scale and small-scale yield data are plotted differently: the small-scale, as mentioned above, was plotted as yield against equivalence ratio; whilst the large-scale yields were plotted as a line because it was a single yield value of unknown ventilation conditions. The large-scale data could then be compared side by side to the small-scale data and a visual comparison made to assess what ventilation condition, or range of conditions best matched the large-scale data. Further to this given the aforementioned problems with CO yields ([Section 2.2.3.2](#)), the recalculated CO yields were also included in the comparison between scales. Within this section the data labelled “SSTF” are the original CO yields calculated using the arithmetic mean, and the data labelled “Whole Test Time” are the recalculated CO yields based on integrating the CO data. For the large-scale yields, “Large-scale” refers to the yields calculated from the TGA based mass loss estimations, whilst “Large-scale CO₂ Based” refers to the yields calculated from the CO₂ based mass loss estimations.

4.1.1.1 1x2.5 mm² LSOH

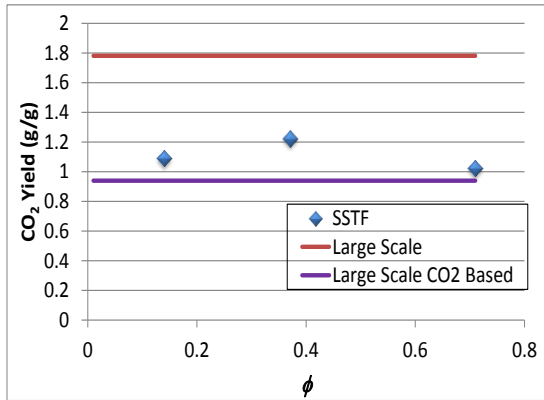


Figure 81 125LSOH CO₂ Comparison

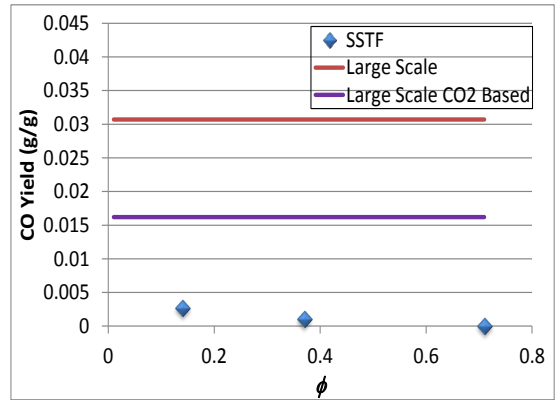


Figure 82 125LSOH 125 CO Comparison

Figure 81 displays the CO₂ comparison between the large and small-scale. It clearly shows that the SSTF results are much closer to the yield calculated using CO₂ based mass loss; the SSTF data point closest to the large-scale yield has an associated ϕ of 0.71. Figure 82 shows the comparison of the CO yields, neither of the two calculated large-scale yields come close to the SSTF data, however the yields calculated with CO₂ based mass loss show much closer agreement than those based on TGA mass loss data.

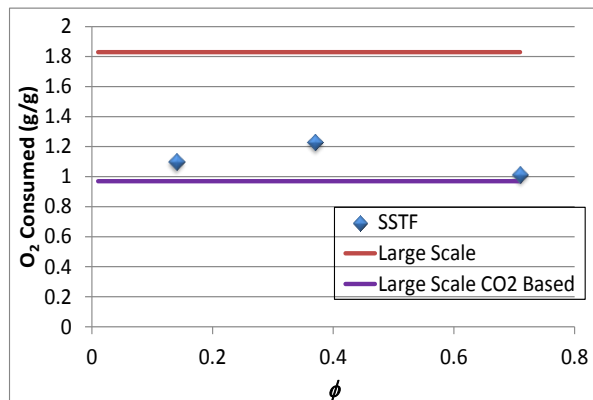


Figure 83 125LSOH O₂ Comparison

Figure 83 shows the O₂ data for the SSTF, which similar to that of the CO₂ data in Figure 81; the large-scale data is also very similar; the SSTF data falls between the two calculated large-scale yields. With the CO₂ based mass loss yields once more

being much closer to the small-scale data than the TGA based mass loss yields. The closest small-scale data point to the large-scale yield is that at $\phi=0.71$.

4.1.1.1 1 x 2.5 mm² LSOH Recalculated Yields

Figure 84 shows that the integrating over the whole test time generated very little change in the CO yields for data at $\phi = 0.37$ and $\phi=0.71$. However it resulted in a large change to the data point at $\phi=0.14$; with the yield increasing almost four fold. However the new yield values still aren't of a magnitude near those of the large-scale yields, meaning the yields derived from integrating over the whole time period only offer a slight improvement over those calculated from the arithmetic mean of the data.

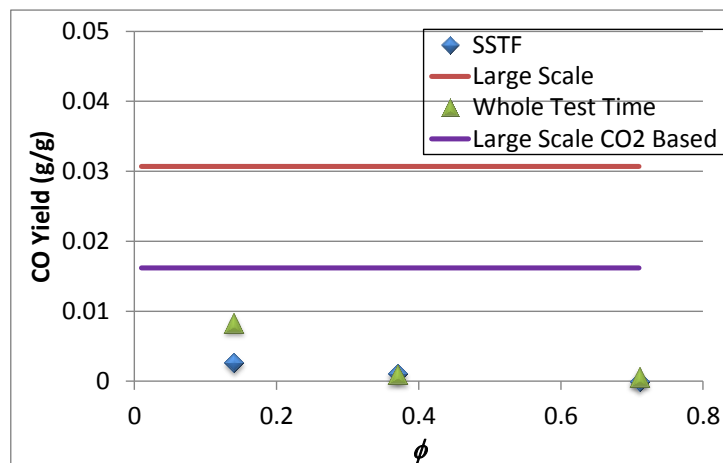


Figure 84 125 LSOH Recalculated CO Yield Comparison

4.1.2 3x1.5 mm² LSOH

Originally this cable material was only tested at three different ϕ values. The data was analysed and compared to the large-scale data and is presented in Figure 85.

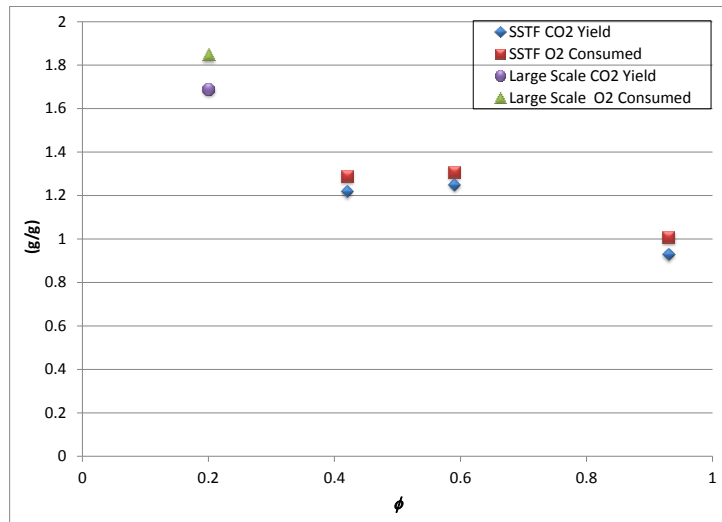


Figure 85 315LSOH Original 3 Tests Comparison

From the data shown in Figure 85 it was decided that further tests needed to be carried out at different ϕ , materials permitted only two more tests. Thus it was decided that one test should be carried out at a $0.6 < \phi < 0.93$ to fill the gap and that one should be $\phi < 0.4$ mainly as there is a complete lack of data points in this window, but also because the large-scale CO₂ yields are greater than those from the SSTF, and typically CO₂ yields rise with an increase in ventilation conditions. The results of adding these two additional data points to those in Figure 85 are shown below in Figure 86 to Figure 88.

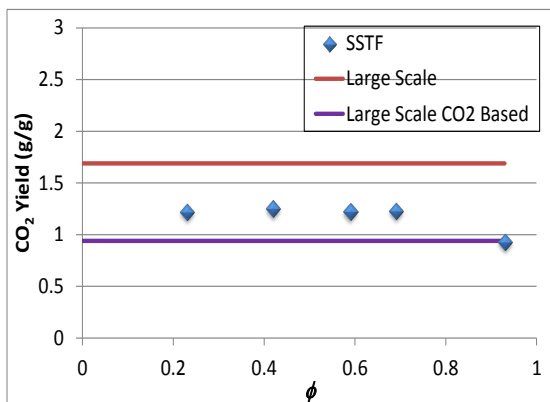


Figure 86 315LSOH CO₂ Comparison

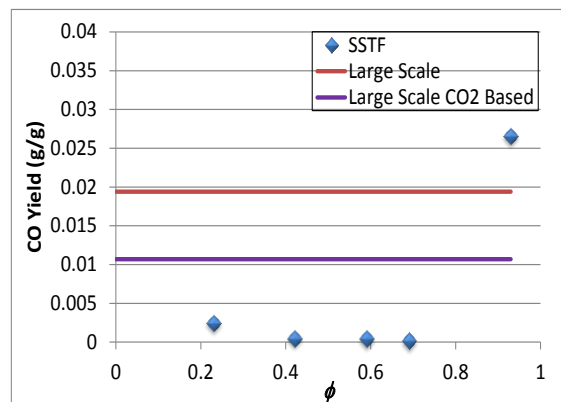


Figure 87 315LSOH CO Comparison

Figure 86 shows that the majority of the SSTF data falls between the two large-scale yields, with the exception of the last data point at $\phi=0.93$, which intersects the CO₂ based mass loss yield, implying that the ventilation conditions at $\phi=0.93$ is representative of the conditions within the large-scale test. The CO data shown in Figure 87 doesn't completely agree this implication; the large-scale yields lie

between the values $0.69 < \phi < 0.93$, what it does achieve is to support the idea that a representative ϕ for the large-scale would be >0.75 . The problem with that idea is $\phi > 0.75$ is associated with under-ventilated conditions and the large-scale test rig is designed to produce well-ventilated conditions.

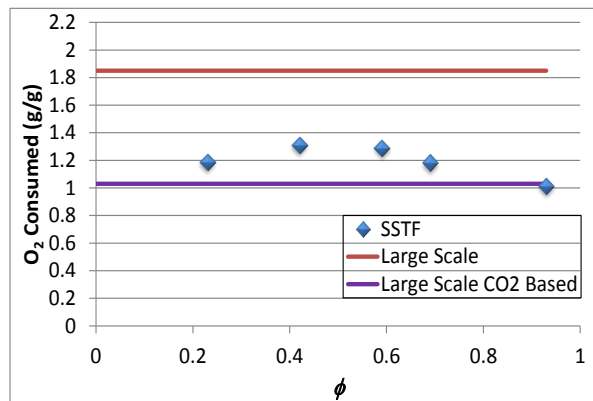


Figure 88 315LSOH O₂ Comparison

The O₂ consumed data shown in Figure 88 mirrors the trends seen in the CO₂ data, with the data point at $\phi=0.93$ intersecting the CO₂ based mass loss yields, adding more evidence to support the counter-intuitive theory that a ϕ associated with under-ventilated conditions is representative of the ventilation conditions within the large-scale test, which are carried out in a test rig designed to give well-ventilated conditions.

4.1.2.1 3 x 1.5 mm² LSOH Recalculated Yields

The difference shown in CO yields in Figure 89 are all but non-existent, showing that for this cable integrating over the whole test period had no overall effect on the yield results.

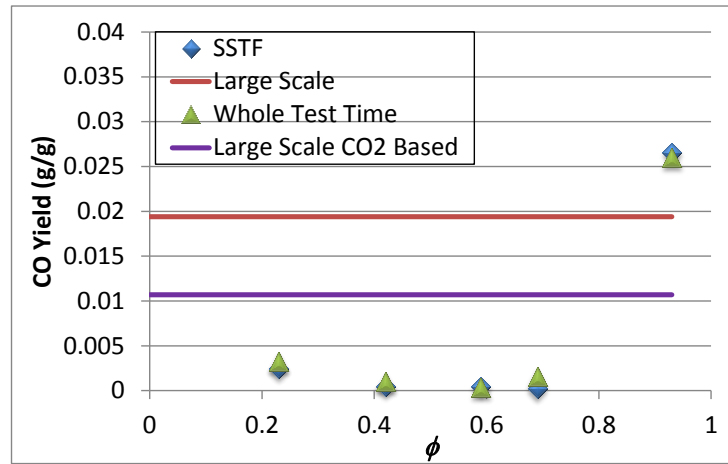


Figure 89 315LSOH Recalculated CO Yield Comparison

4.1.3 FR 4804

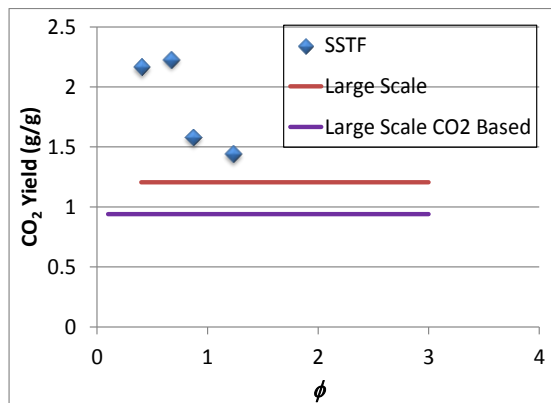


Figure 90 FR 4804 CO₂ Comparison

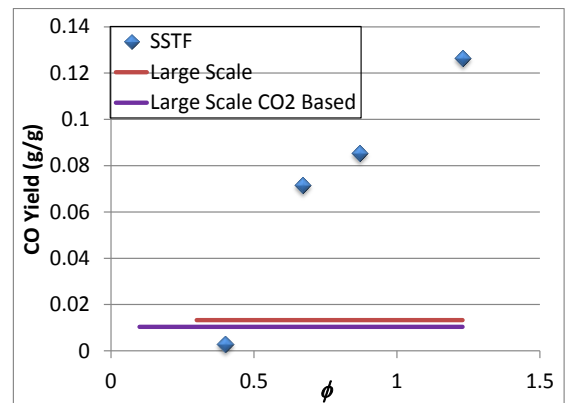


Figure 91 FR 4804 CO Comparison

Figure 90 shows the CO₂ data for FR4804, the SSTF yield data is of a greater magnitude than the large-scale yield data, the trend of the small-scale data would imply that the SSTF data would intersect the large-scale yields at $\phi > 1.23$, the addition of the CO₂ based mass loss yield doesn't help improve the data, in fact it is further from the data than the TGA based mass loss yield. The CO data in Figure 91 shows the large-scale data intersecting the SSTF data line at a more reasonable value of $0.4 < \phi < 0.67$, meaning that the ϕ value representative of the large-scale test is one associated with well-ventilated conditions. Once again the CO₂ based mass loss yield has little effect on estimating a representative ϕ value as it falls

within the same range as the TGA based mass loss data, however does imply a slightly more well-ventilated approximation for ϕ .

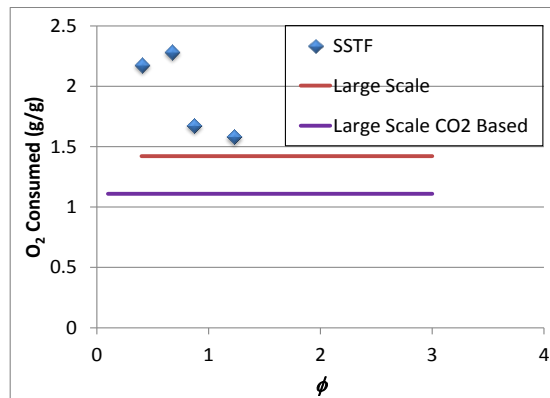


Figure 92 FR 4804 O₂ Comparison

The O₂ data in Figure 92 is very similar to that of the CO₂ data, with the small difference that the value for the large-scale yield is slightly greater for the O₂ consumption data, this change means that the last data point for the SSTF series ($\phi=1.23$) is only marginally above the large-scale yield. The similarity is also reflected by the CO₂ based mass loss yield, in that it is also of lesser value than the TGA based mass loss yield taking it further away from the SSTF data points.

4.1.4 Melos 1006F

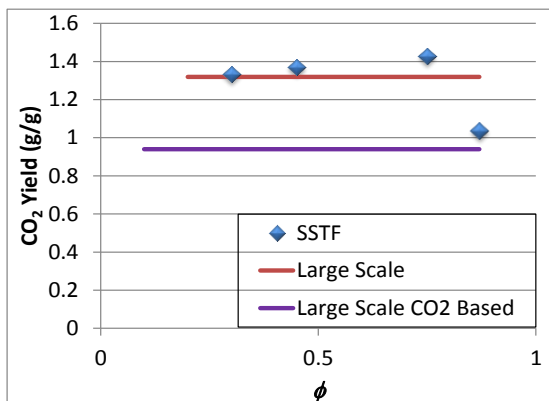


Figure 93 Melos 1006F CO₂ Comparison

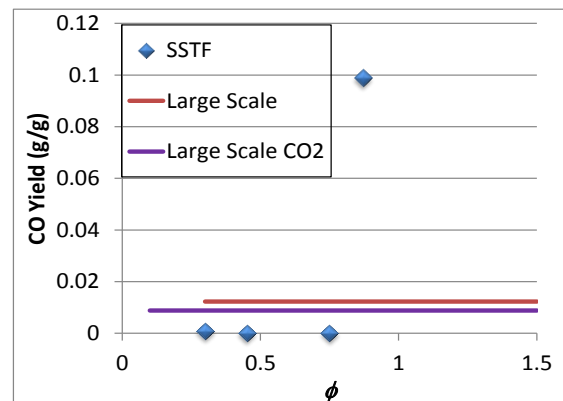


Figure 94 Melos 1006F CO Comparison

The CO₂ data (Figure 93) shows the SSTF data being closest to the TGA based large-scale yields, with the data point at $\phi=0.3$ actually lying on top of the large-scale

data. The fact that the intersecting point is at a ϕ value associated with very well-ventilated fire conditions is encouraging. Though it must be noted that the last data point for ($\phi=0.87$) is of a similar value to the large-scale CO₂ based yield, and it could be this value of ϕ which is close to representing the ventilation conditions within the large-scale test rig. That said it would be both more intuitive and logical to assume that the smaller value of ϕ is most likely to be the correct one. The CO data (Figure 94) shows that the large-scale yields lie between $0.75 < \phi < 0.87$, again implying that the representative ϕ for the large-scale test is that associated with under-ventilated conditions.

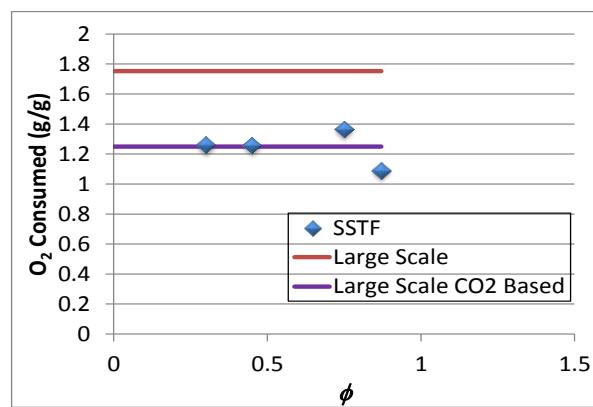


Figure 95 Melos 1006F O₂ Comparison

Figure 95 shows the O₂ data, which once more is very similar to the CO₂ data with respect to the SSTF data, but differs in terms of the large-scale yield. The O₂ consumed data shows the SSTF data clustering around the CO₂ based large-scale yield, with the two data points that have the lowest value of ϕ lying on the large-scale yield line, and the other two positioned just above and below the line. This would imply that the conditions closest to those in the large-scale test are associated with the lower values of ϕ .

4.1.4.1 Melos 1006F Recalculated Yields

In Figure 96 the use of integration over the whole test time has little effect on the approximation of ventilation conditions in the large-scale test. The large-scale values still lie between the points of $\phi=0.75$ and $\phi=0.87$.

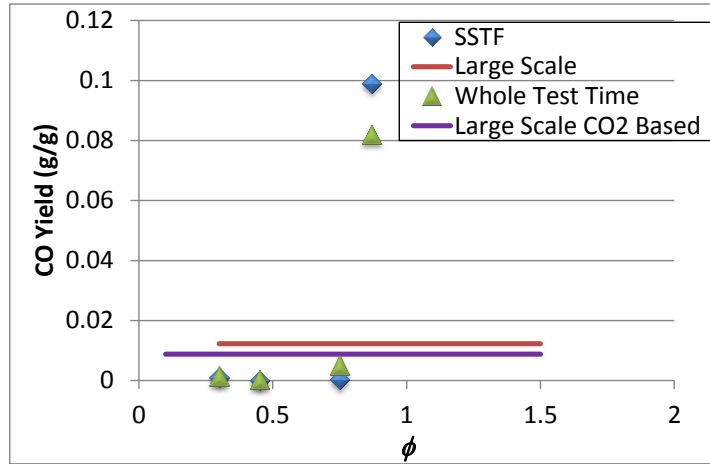


Figure 96 Melos 1006F Recalculated CO Yield Comparison

4.1.5 MGN 09005

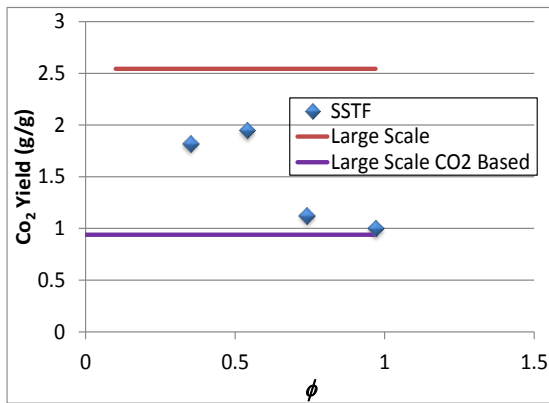


Figure 97 MGN 09005 CO₂ Comparison

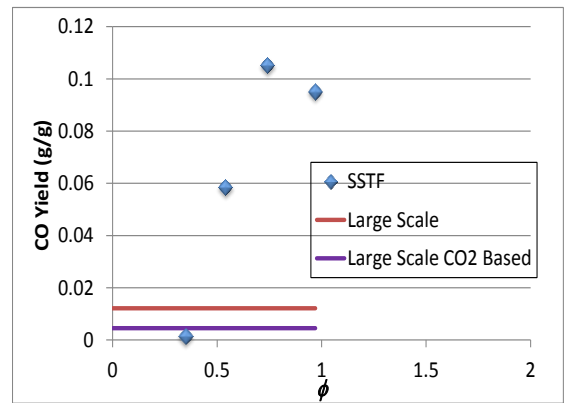


Figure 98 MGN 09005 CO Comparison

Figure 97 shows the CO₂ data from the small-scale test lies between the two large-scale yields, tending towards the CO₂ based mass loss yields as the value of ϕ increases. Figure 98 shows the CO displaying the opposite trend, with the SSTF data moving further away from the large-scale yields as ϕ increases. The CO₂ based mass loss yield is once again closest to the SSTF data, at $\phi = 0.35$.

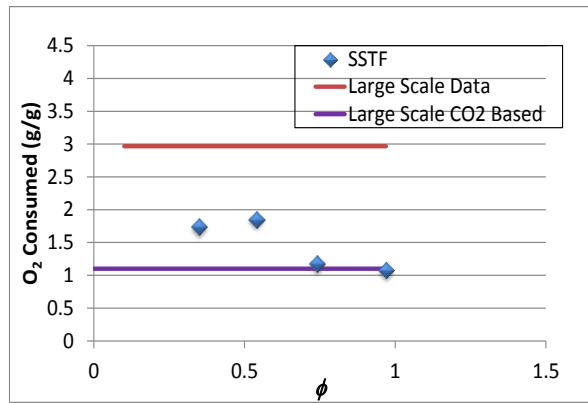


Figure 99 MGN 09005 O₂ Comparison

The O₂ data in Figure 99 shows good agreement with that of the CO₂ data in Figure 97, the large-scale data with the exception that the SSTF not only tends towards the large-scale yield line at higher values of ϕ but crosses within the range $0.74 < \phi < 0.97$

4.1.5.1 MGN 09005 Recalculated Yields

Figure 100 shows that integrating over the whole test has some significant changes on both the SSTF yields but the comparison of data. The first data point is the same for both the SSTF yields, but the following data points start to diverge. The biggest difference in terms of comparing the two scales of testing is the second data point, $\phi=0.54$, where instead of being ≈ 5 times greater than the large-scale yields, the integrated yield lies between the two yield values. The implication being that the conditions representative of those in the large-scale test lie in the range $0.35 < \phi < 0.54$.

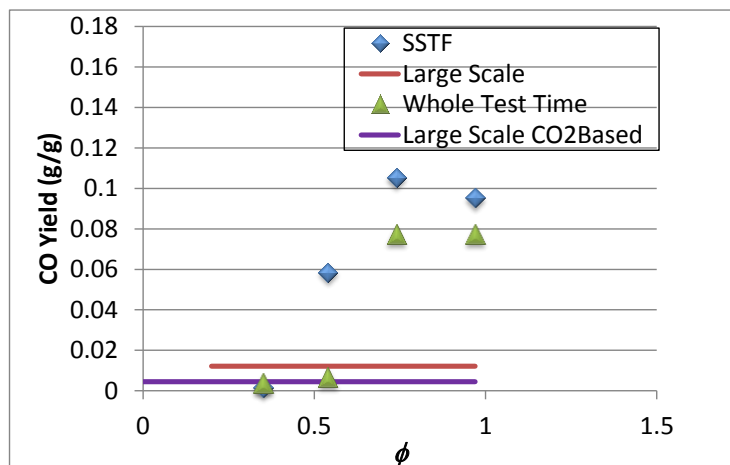


Figure 100 MGN 09005 Recalculated CO Yield Comparison

4.1.6 WLS 08006

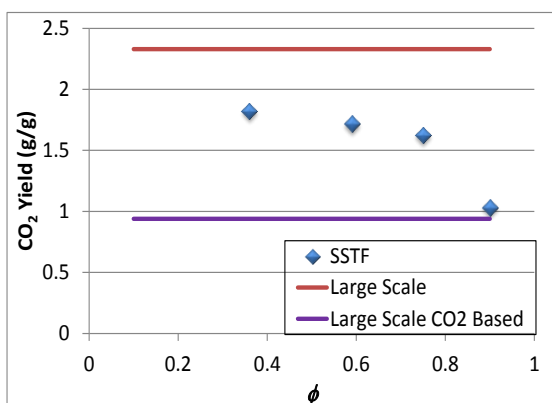


Figure 101 WLS 08006 CO₂ Comparison

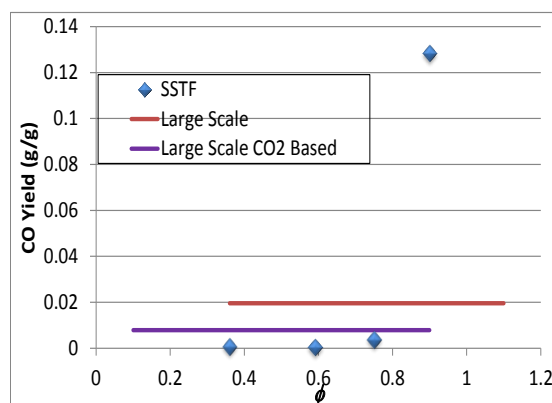


Figure 102 WLS 08006 CO Comparison

The CO₂ data shown in Figure 101 shows the expected decrease of CO₂ yield with decreasing ventilation conditions, it also shows the SSTF data moving away from the TGA based mass loss yield and towards the CO₂ based mass loss yield, with the final data point ($\phi=0.9$) almost intersecting the trendline. Figure 102 shows the CO data, with both large-scale yields sitting between the last two points of the SSTF data, implying a representative ϕ being within the range of $0.75 < \phi < 0.9$. Again the CO₂ based mass loss yields are closest to the SSTF data.

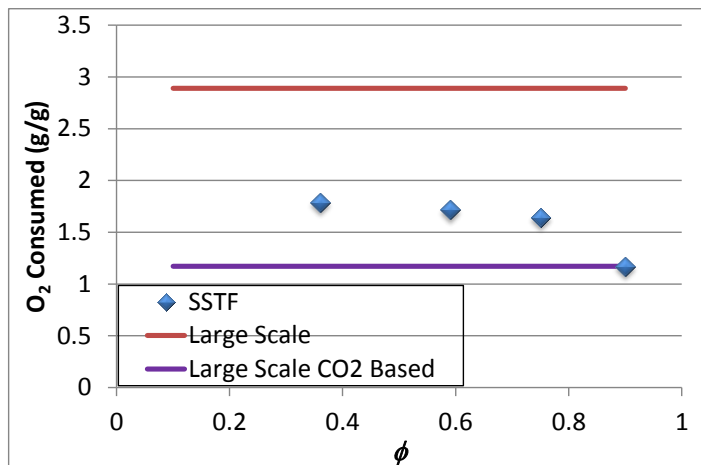


Figure 103 WLS 08006 O₂ Comparison

Figure 103 shows O₂ consumption data again displaying the same trend in SSTF data as the CO₂ data, with the CO₂ based yields being slightly higher than in the CO₂ data, resulting in the last point of SSTF data crossing the large-scale yield line.

4.1.6.1 WLS 08006 Recalculated Yields

The use of integration had no effect on the SSTF data with the exception of the data point at $\phi=0.9$ as shown in Figure 104. Even with this change to the last data point the impact on the relation to the large-scale yields is negligible.

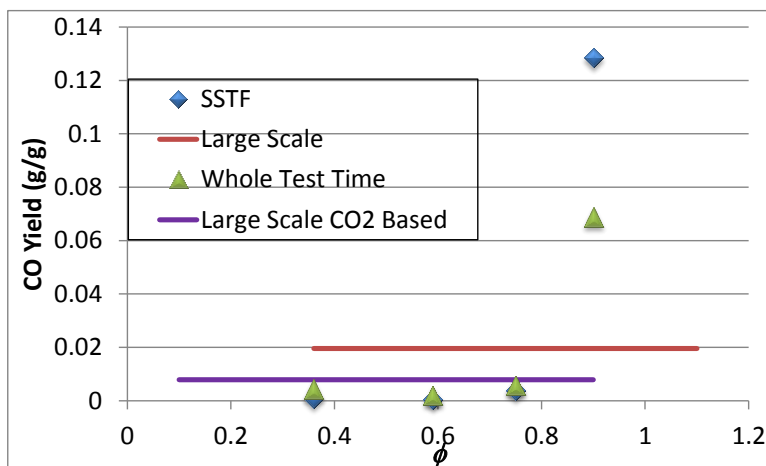


Figure 104 WLS 08006 Recalculated CO Yield Comparison

4.1.7 1x25mm² PVC

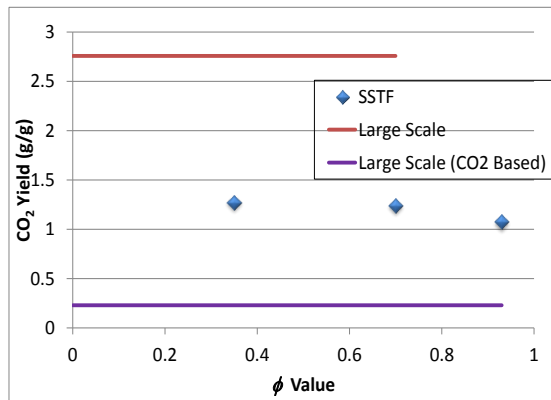


Figure 105 125 PVC CO₂ Comparison

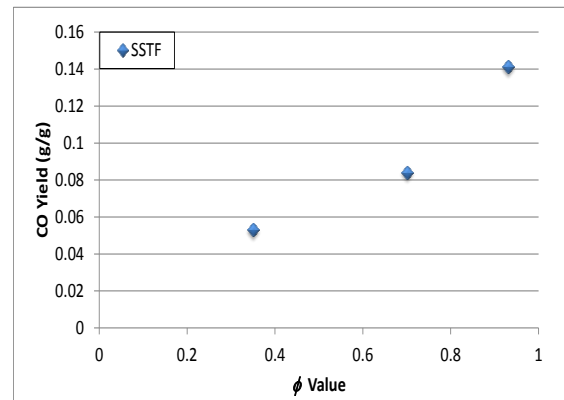


Figure 106 125 PVC CO Comparison

Figure 105 shows that the CO₂ data from the SSTF lies between the two large-scale yields. It displays a slight trend towards the CO₂ based large-scale data as ϕ increases. The CO data (Figure 106) shows the test data obtained from the SSTF but the large-scale data is absent due to the large-scale CO data being entirely negative, thus making it unusable in calculating a yield.

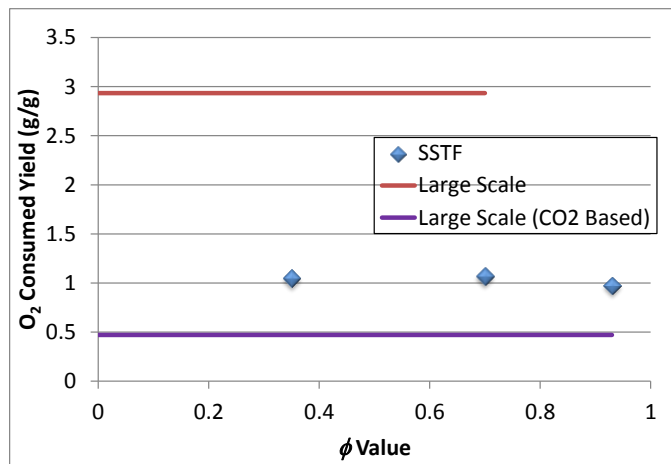


Figure 107 125 PVC O₂ Comparison

The O₂ consumption data in Figure 107 shows the SSTF data lying again between the two large-scale yields, however the O₂ data doesn't tend as much towards the large-scale data as the CO₂ data does.

4.1.7.1 1x25mm² PVC Recalculate Yields

Figure 108 illustrates that there is little difference between the two methods in terms of yields, thus resulting in two very similar trendlines. However because there is no large-scale CO yield data available for 125PVC any differences that could have been there would have been all but moot.

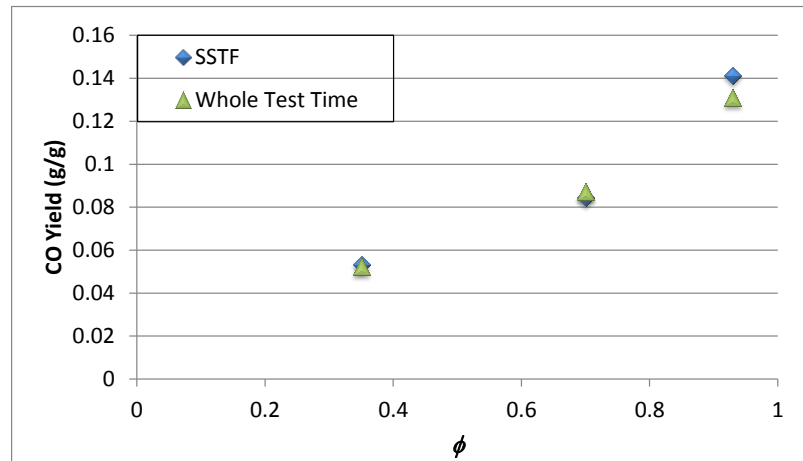


Figure 108 125 PVC CO Yield Comparison

4.2 EQUIVALENCE RATIO COMPARISON SUMMARY

Most of the data implies that the large-scale ventilations conditions are best represented in the small-scale by a ϕ associated with under-ventilated tests. As previously mentioned even with the data repeatedly implying an under-ventilated ϕ it's hard to imagine under-ventilated conditions being representative of a test designed to be well-ventilated. One of the main things that came out of the comparison is that the SSTF consistently was closer to, if not intersecting, the yields calculated using the CO₂ based mass loss estimations

4.3 EQUIVALENCE RATIO WITH RE-CALCULATED YIELDS COMPARISON SUMMARY

With the exception of the MGN cable type the re-calculated yields based on integrating over the whole test period to get the average CO (%) had very little impact on how the SSTF data interacted with the large-scale data.

4.4 CO/CO₂ RATIOS

The next method of comparison focused on was CO/CO₂ ratios. In order to make all the data comparable the SSTF data was modified such that the test data started at zero minutes rather than its normal six minutes.

4.4.1 1x2.5mm² LSOH

In [Figure 109](#) 125LSOH1 displays a large peak at the start of the test, corresponding to a large CO peak, before returning to near zero where it remains for most of the test. The large-scale data has a ratio greater than that of 125LSOH1, implying a representative $\phi > 0.37$. Normally a test carried out with a higher ϕ than that of 125LSOH would help narrow the ϕ range for approximating the large-scale conditions by adding an upper boundary. However in the case of 125LOSH2, this is not the case; the CO/CO₂ ratio displays entirely negative values. In order to try and understand why 125LSOH contained entirely negative values the relevant CO and CO₂ data was analysed ([Figure 110](#)).

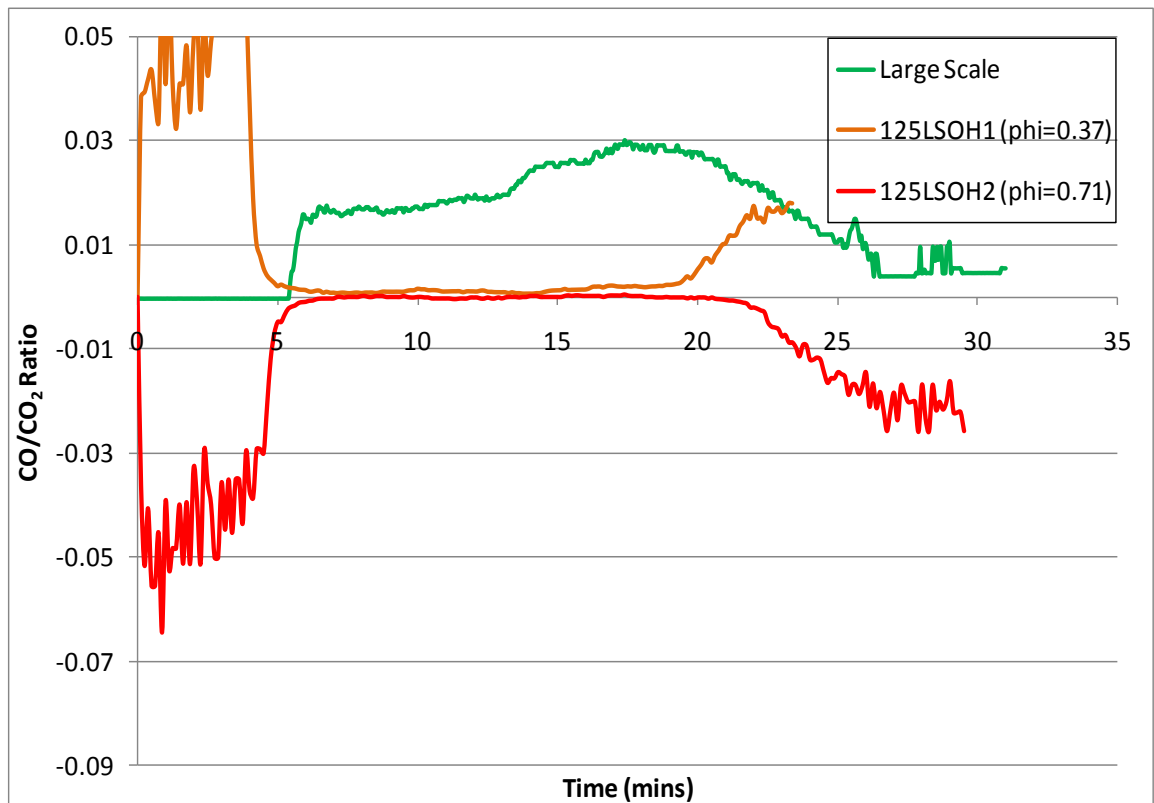


Figure 109 125LSOH CO/CO₂ Ratio

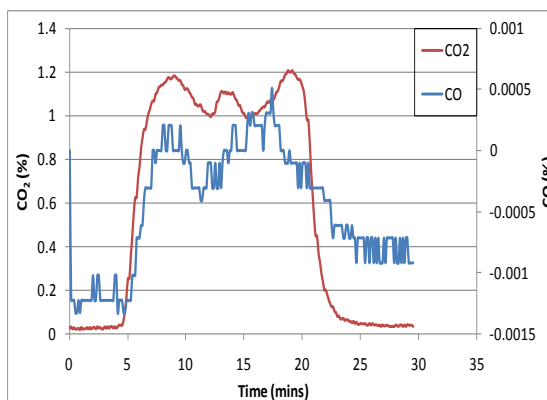


Figure 110 125LSOH CO₂ and CO Data

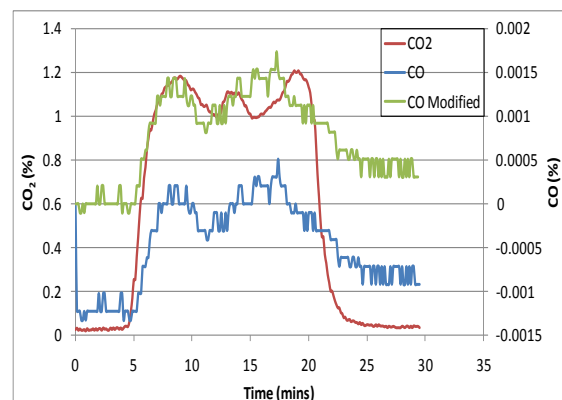


Figure 111 125 LSOH CO₂, CO and Modified CO Data

As can be seen in [Figure 110](#) the CO₂ data is entirely positive, but more significantly the CO data can be seen to drop from 0 to a negative value at the start of the test. The calibration data was examined and nothing erroneous was found, this coupled with the CO data responding in the same manner as the CO₂ data infers that the analyser was responding correctly therefore the CO data was modified by removing the drop in values at the start of the test. This was achieved by calculating the magnitude of the drop and then adding that value onto every data point taken

during the test. Figure 111 shows the results of modifying the data, which is clearly an improvement over the original data; importantly the profile of the modified CO is the same as the original. The modified CO data was then used to recalculate the CO/CO₂ ratio, and can be seen in Figure 112.

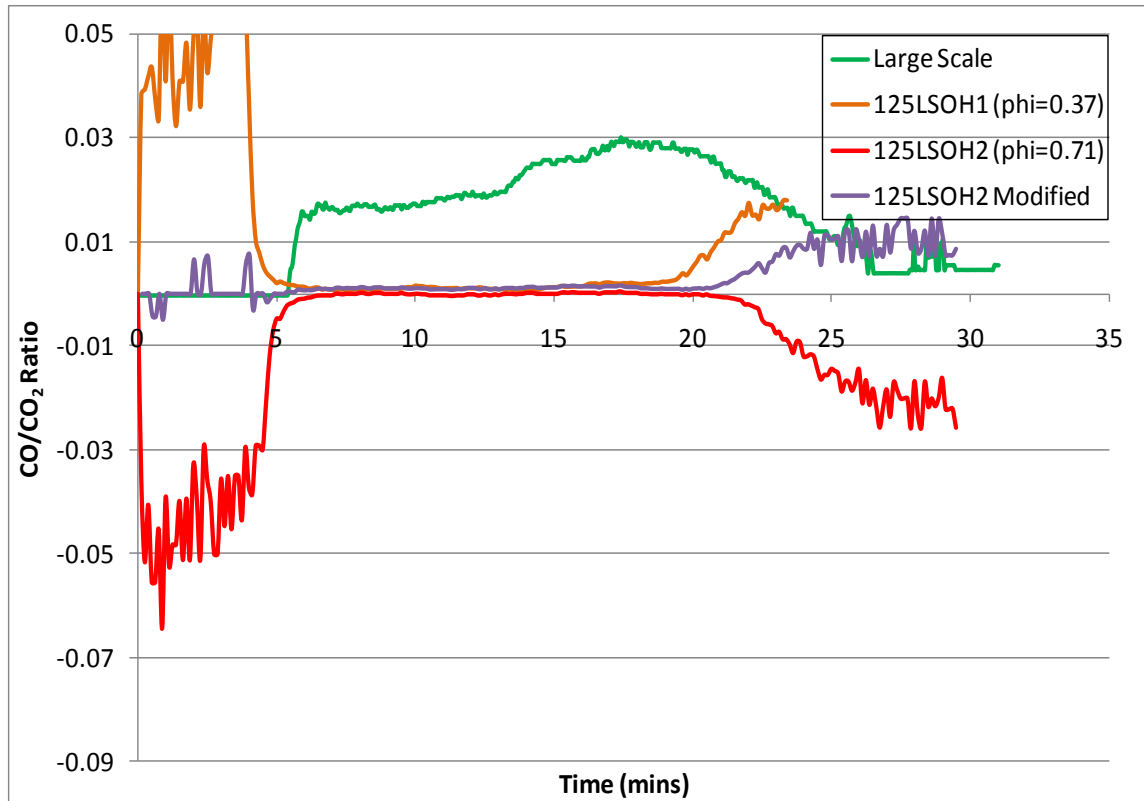


Figure 112 125LSOH Modified CO/CO₂ Ratio

The prediction was that the 125LSOH2 modified data would follow the same profile as that displayed by 125LSOH2 but starting from zero instead of dropping to -0.05. However 125LSOH2 didn't conform to the prediction, instead the modified CO/CO₂ ratio remains close to zero throughout the entire test. Due to the modified data staying close to zero it does not provide an upper boundary for the large-scale data, meaning that all can be inferred from is that the approximate $\phi > 0.37$.

4.4.2 3x1.5mm² LOSH

In Figure 113 315LSOH5 shows the highest overall CO/CO₂ ratio, between 15 and 40 minutes, then drops to a value close to zero, where it stays until 55 minutes. It then begins to climb back to the value it was before it fell. The drop in the CO/CO₂ ratio corresponds to a drop in both the CO and CO₂ values in the small-

scale test. 315LSOH1 and 315LSOH2 both exhibit large peaks at the beginning of the test, relative to the other test data; the reason being that in these two tests the peak in CO coincided with a smaller value of CO₂ than the other tests. The negative ratio values displayed at the start of the test are due to the CO data being very close to zero, and the slight fluctuations in that data sometimes resulting in negative values. In the ratio calculations these very slight negative values are divided by a value of CO₂ less than 1, resulting in the slight deviation away from zero being amplified. The large-scale data lies between 315LSOH4 and 315LSOH5 implying a representative ϕ value being in the range $0.69 < \phi < 0.93$. However the large-scale data is closer to 315LSOH4, indicating the approximate ϕ value being closer to 0.69.

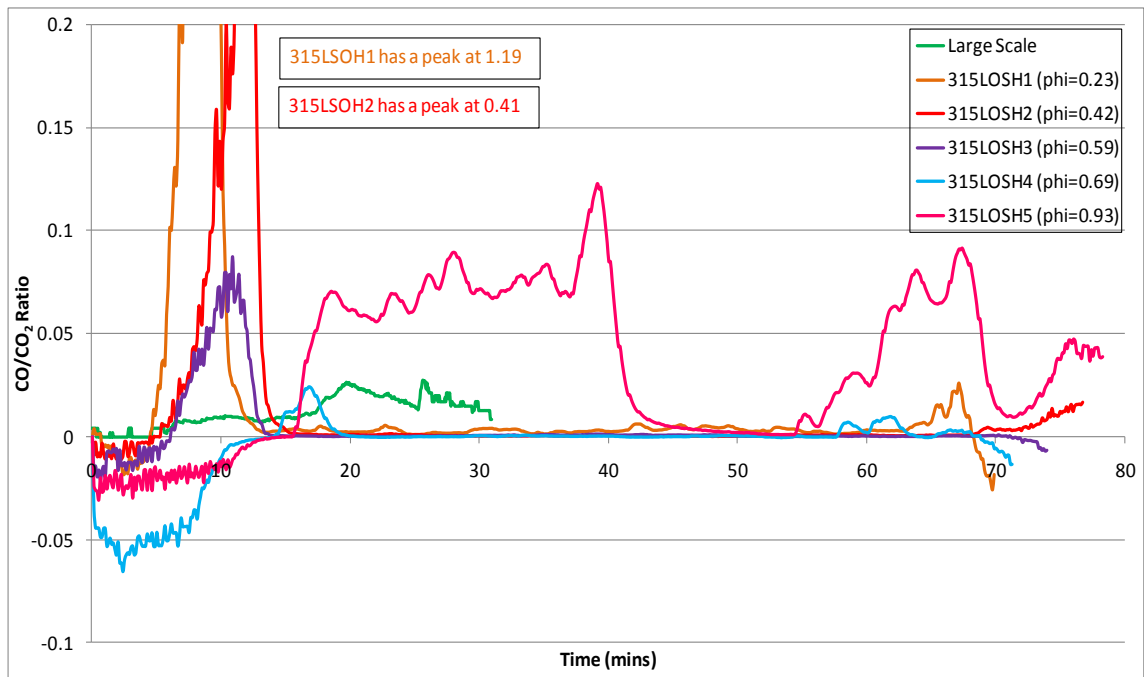


Figure 113 315LSOH CO/CO₂ Ratio

4.4.3 FR 4804

The data in Figure 114 shows that as ϕ increases in value, there is a corresponding rise in the CO/CO₂ ratio. It also shows that the large-scale data value is closest to that of FR1. FR1 has the lowest ϕ ratio, suggesting that the large-scale test conditions are more similar to the most-well-ventilated SSTF tests. The series of

peaks and troughs is caused by the intermittent flaming that occurs during the testing of FR 4804 in the SSTF.

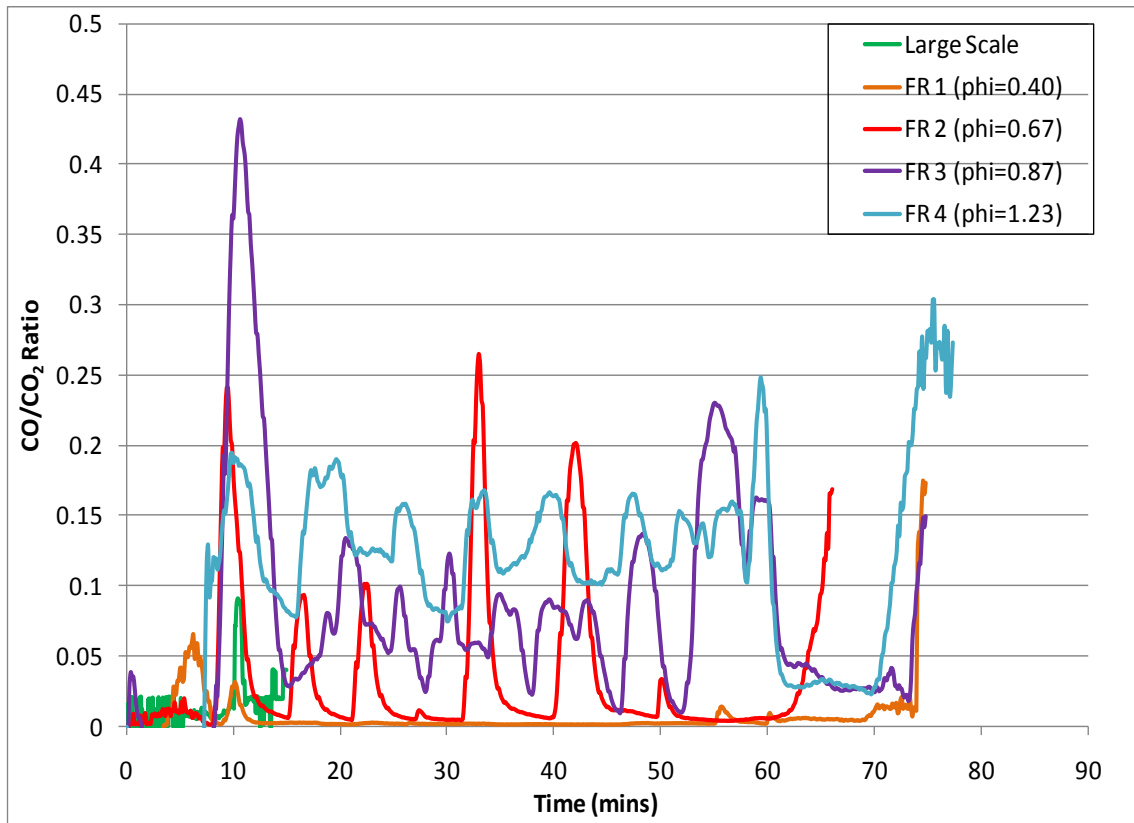


Figure 114 FR 4804 CO/CO₂ Ratio

4.4.4 Melos 1006F

Figure 115 shows that the higher the value of ϕ , the greater the CO/CO₂ ratio. Some of the tests exhibit negative ratios at the start of the test, which as explained earlier are due to the CO values that are only just negative being amplified by a CO₂ value less than 1. Melos 1-3 all show very similar values, whereas Melos 4 is markedly different. This is explained by the cable's property of a sharp increase in CO values over a very narrow ϕ range as shown in Figure 32. The large-scale CO/CO₂ ratio is less than that of Melos 4, but greater than Melos 3, thus for Melos the CO/CO₂ data shows that the large-scale test has an equivalent ϕ value in the range of $0.75 < \phi < 0.87$.

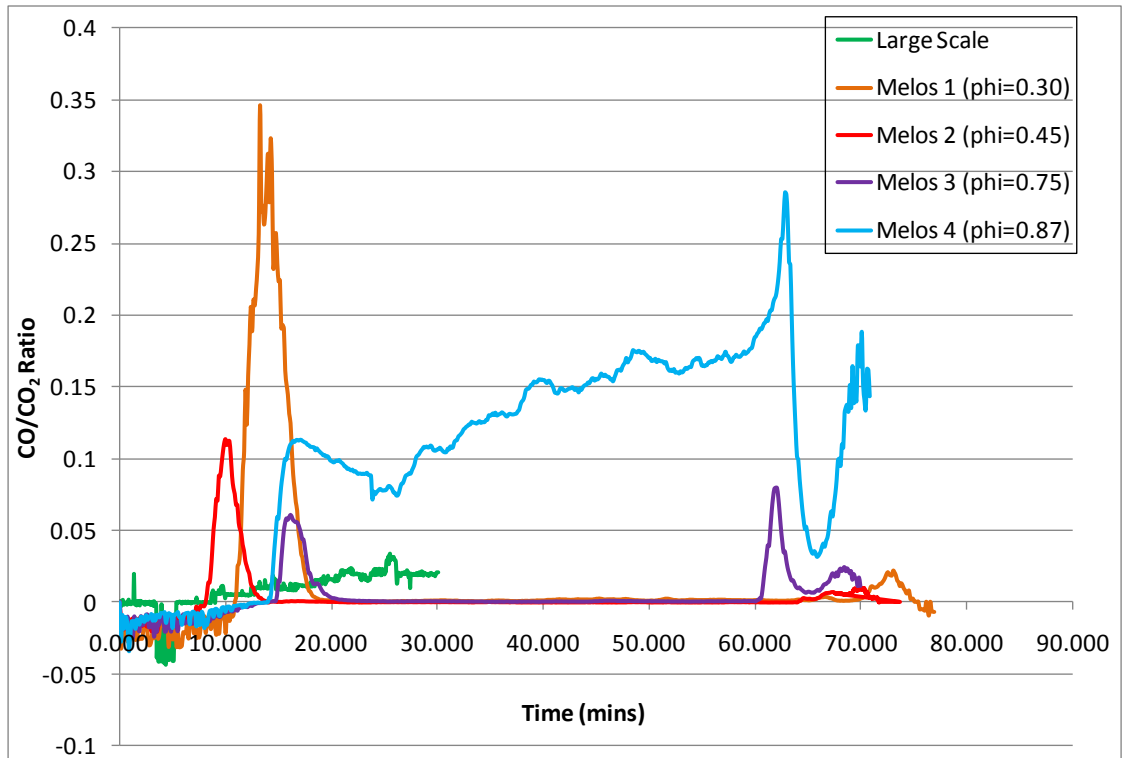


Figure 115 Melos 1006F CO/CO₂ Ratio

4.4.5 MGN 09005

The CO/CO₂ ratios are presented in Figure 116. The highest values are results of the tests with the highest values of ϕ . Two of the tests, MGN 3 and MGN 4 both exhibit negative value at the start of the test, due to the same reason as the other tests in Figure 113 and Figure 115. The large-scale test data is once more closest to the SSTF test that has the lowest ϕ .

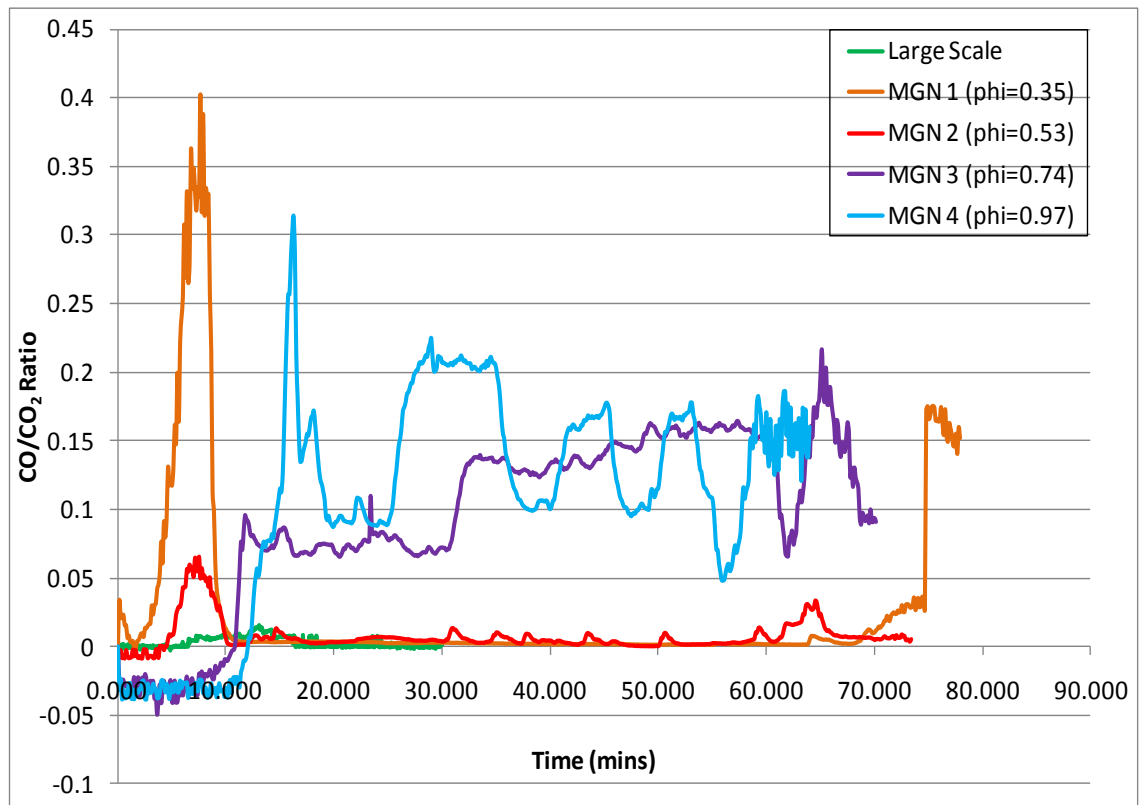


Figure 116 MGN 09005 CO/CO₂ Ratio

4.4.6 WLS 08006

In Figure 117 the largest highest CO/CO₂ ratio, is displayed by the test with the greatest value of ϕ . Whilst all the others show very similar CO/CO₂ trends of very close to zero. The large-scale CO/CO₂ ratio is low, and similarly to Melos the data lies above the values of the first three tests and below the value of the last test. This implies that the large-scale test exhibits ventilation conditions within the range $0.75 < \phi < 0.9$.

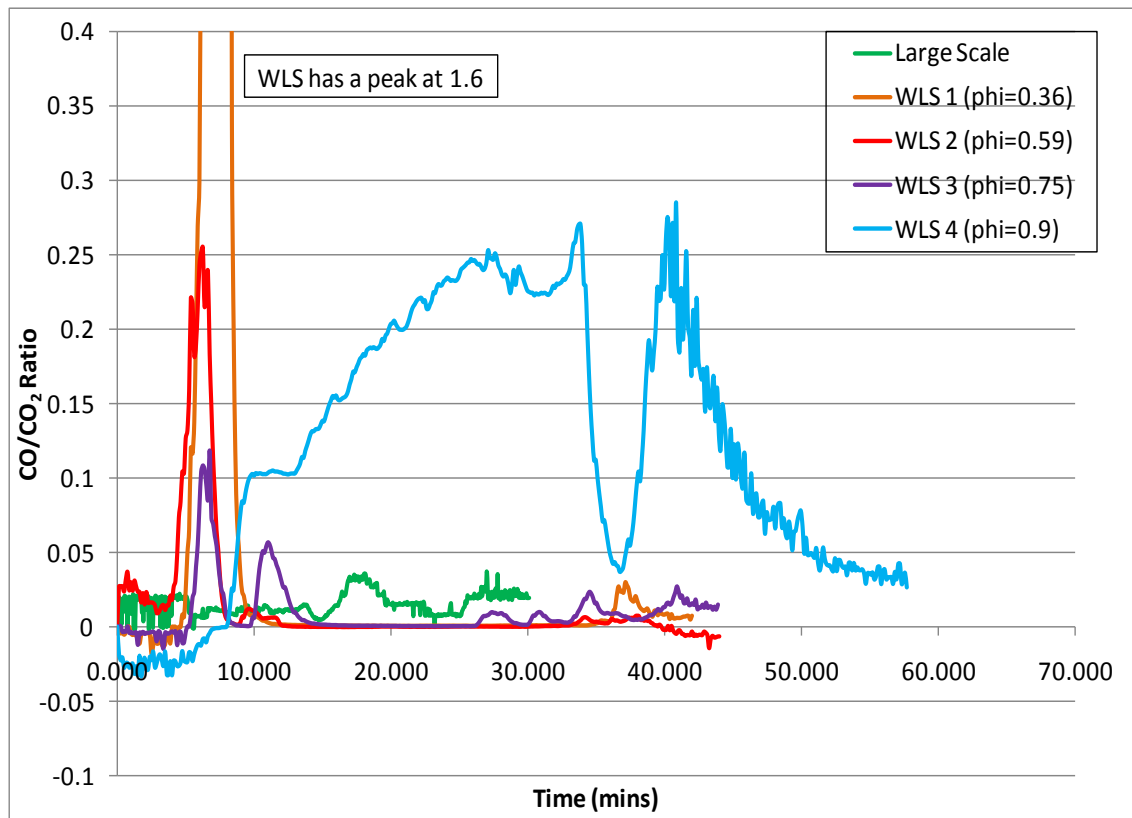


Figure 117 WLS 08006 CO/CO₂ Ratio

4.5 CO/CO₂ RATIO COMPARISON SUMMARY

Overall the CO/CO₂ ratios for the large-scale test tend to be closest to the SSTF test that is the most well-ventilation lending support to the representative ϕ value being small. It is hard directly compare the large and small-scale tests due to the differences in the methods, e.g. The large-scale test is much shorter than the small-scale test. Some of the small-scale test samples don't ignite until a time equivalent to a third of the way through the large-scale test.

4.6 CO₂/CO RATIOS

CO₂/CO ratios were also calculated, however the data is more difficult to interpret and compare. In the SSTF small changes are seen in the CO readings across the test, even during what's considered steady-state period. These changes are amplified by the act of using those values as the denominator producing numerous peaks which have a large magnitude due to the small values of CO (%).

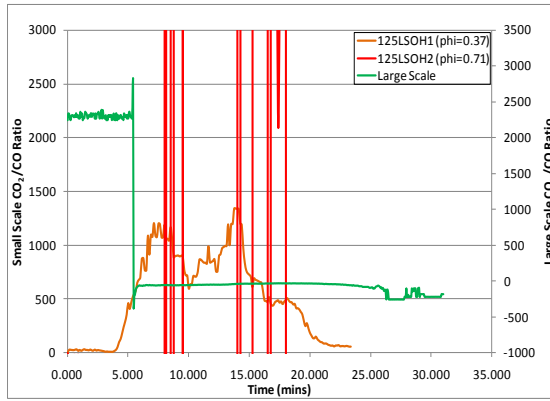


Figure 118 125LSOH CO₂/CO Ratio

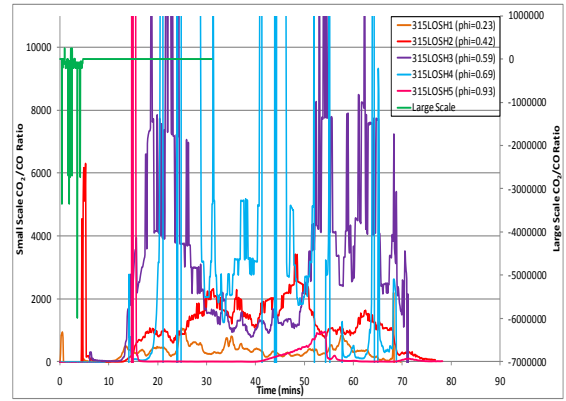


Figure 119 315LSOH CO₂/CO Ratio

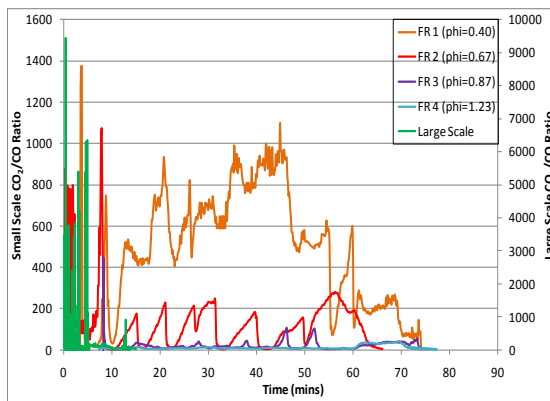


Figure 120 FR 4804 CO₂/CO Ratio

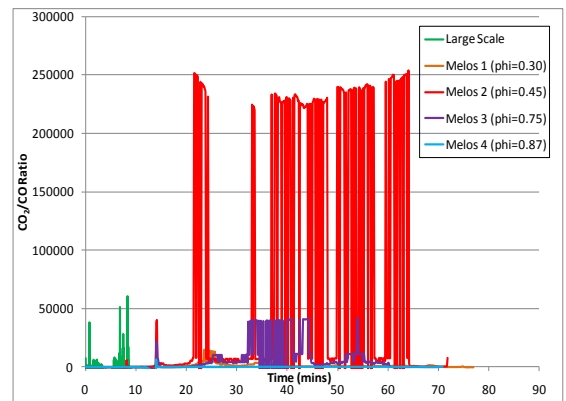


Figure 121 Melos 1006F CO₂/CO Ratio

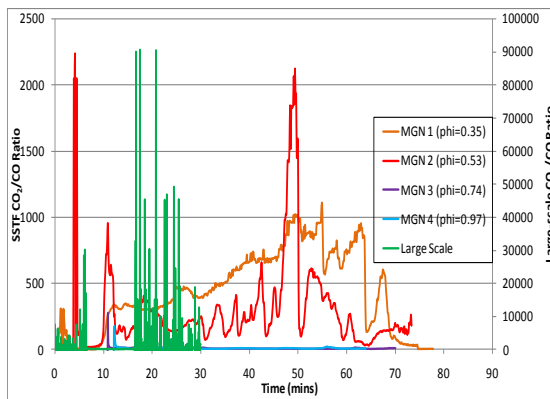


Figure 122 MGN 09005 CO₂/CO Ratio

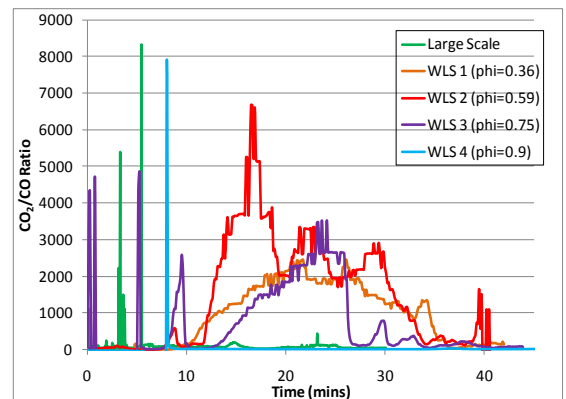


Figure 123 WLS 08006 CO₂/CO Ratio

Each of Figure 118, Figure 119, and Figure 121 show at least one unusual CO₂/CO ratio, there is no consistency, just peaks and troughs. A reason for this would be unsteady CO or CO₂ data, but as can be seen in each of their respective graphs showing CO₂ and CO data (Figure 124, Figure 125, Figure 126, and Figure 127) both traces look relatively steady. Thus the only explanation is the very small changes in CO values. Whilst the traces are relatively steady there are still minute

variations across the CO data. These changes are in the thousandth of a percent range, which are translated into huge peaks and troughs in the CO₂/CO ratios.

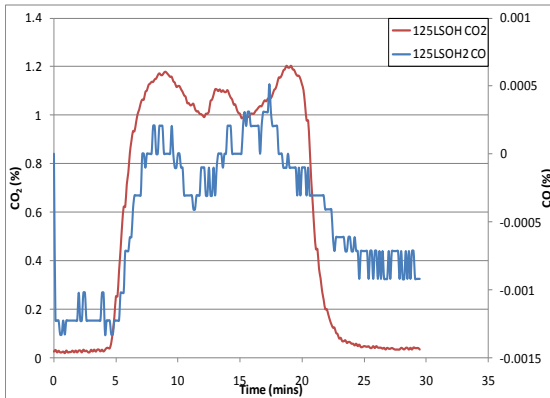


Figure 124 125LSOH 2 CO₂ and CO Data

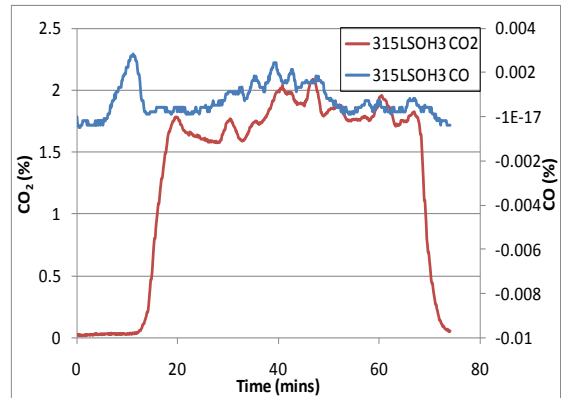


Figure 125 315LSOH 3 CO₂ and CO Data

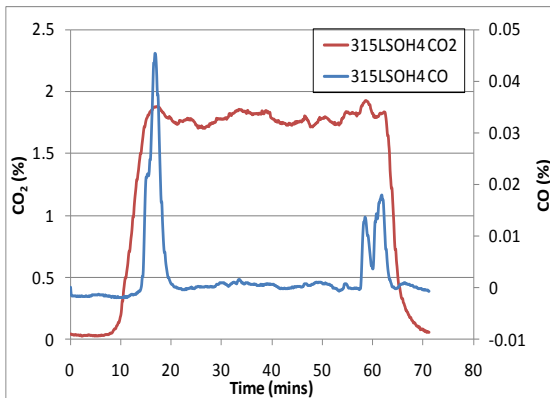


Figure 126 315LSOH 4 CO₂ and CO Data

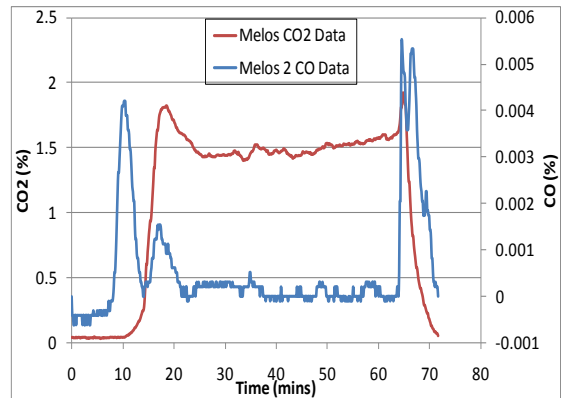


Figure 127 Melos 2 CO₂ and CO Data

To try and improve the CO₂/CO ratios a 10 point moving average was applied to the data for 315LSOH and WLS 08006.

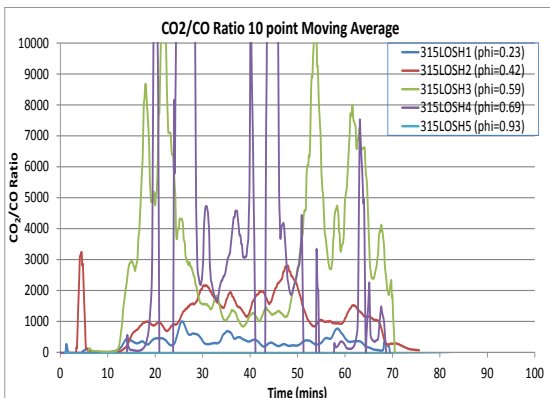


Figure 128 315LSOH 10 Point Moving Average

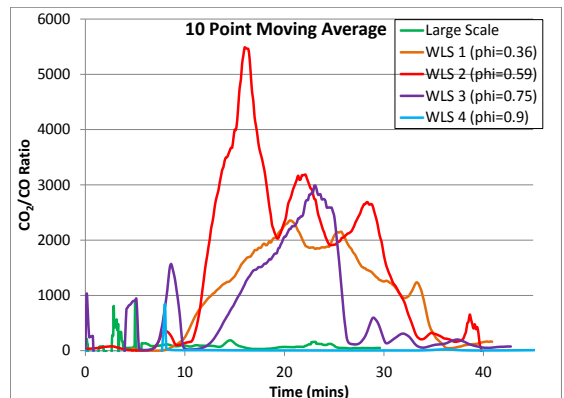


Figure 129 WLS 08006 10 Point Moving Average

As can be seen in [Figure 128](#) and [Figure 129](#) the application of a moving average does improve the overall smoothness of the line, as would be expected, it doesn't greatly improve the data for comparing across the two scales.

4.7 CO₂/CO RATIO COMPARISON SUMMARY

Whilst CO₂/CO ratio is a common method to compare fire conditions between tests, its use to compare between the scales here has been proven limited, if useful at all, due to both the high degree of oscillation apparent in most of the ratios and the magnitude of the values of those ratios. To be perspective a CO₂/CO ratio with a magnitude ≤ 100 is held as being acceptable, whereas the values here are generally in a range of magnitude of 10^3 to 10^4 .

4.8 HEAT RELEASE (kW/g)

Another method used to compare the two data sets was heat release. Using oxygen depletion calorimetry, the data from the paramagnetic oxygen analysers from the Purser furnace can be used to generate heat release data that can be compared to the large-scale data. However the large-scale data has heat release in kW, whereas oxygen depletion calorimetry uses the assumption of 13.1kJ released per gram of oxygen consumed, resulting in a heat release value in kJ.

However kW can be calculated from kJ using the conversion of $1\text{kW} = 1\text{kJ/s}$.

There are however exceptions to the above methodology: the large-scale data for 1 x 2.5mm² LSOH, 3 x 1.5mm² LSOH, and 1 x 25mm² PVC were devoid of measured heat release rate (HRR) data, so instead to calculate HRR, the average oxygen depletion value was combined with oxygen depletion calorimetry in the same way the SSTF data was handled. Regardless of the methodology used to generate the value for HRR, all values were normalised against mass loss.

4.8.1 1 x 2.5mm² LSOH

The heat release data in [Figure 130](#) clearly shows the large-scale data dwarfing that of the SSTF data, which all have similar values for the different fire

conditions. There is however a trend for the HRR value to increase slightly with a decreasing value of ϕ . This again lends support to a low value of ϕ being representative of the large-scale test conditions; unfortunately the highest level of ventilation easily achievable within the SSTF is that of $\phi = 0.14$, which can be clearly seen to have a magnitude far less that of the large-scale data.

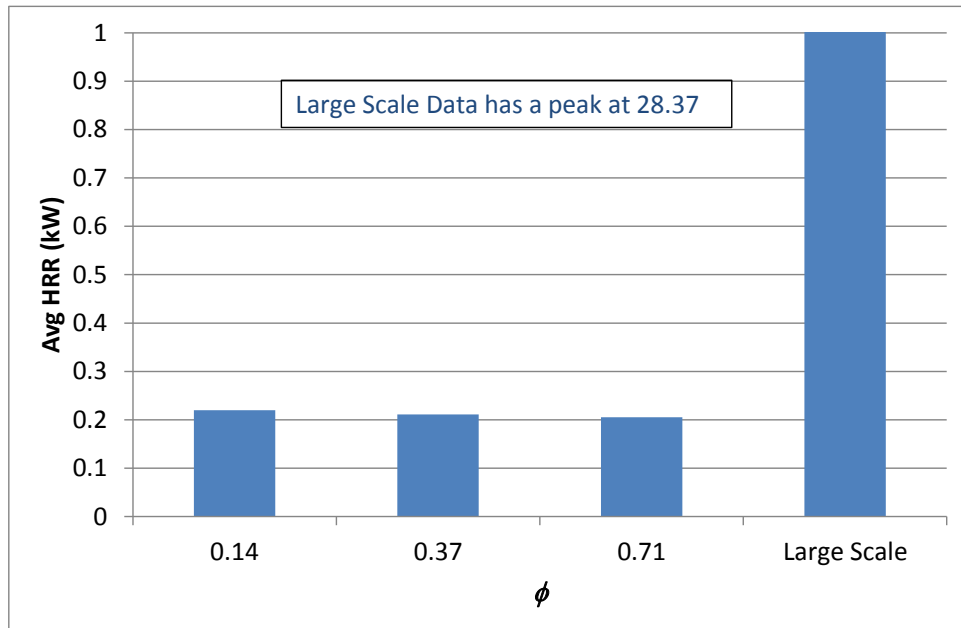


Figure 130 125LSOH Heat Release Rate

4.8.2 3 x 1.5mm² LSOH

Figure 131 shows a general trend for the HRR to decrease with an increasing value of ϕ , however the run at $\phi = 0.23$, which is the most ventilated for this cable type produced a HRR value that is 100 times smaller than the HRR value generated by the large-scale test. This highlights the large disparity between the scales, inferring a lack of correlation between the two scales.

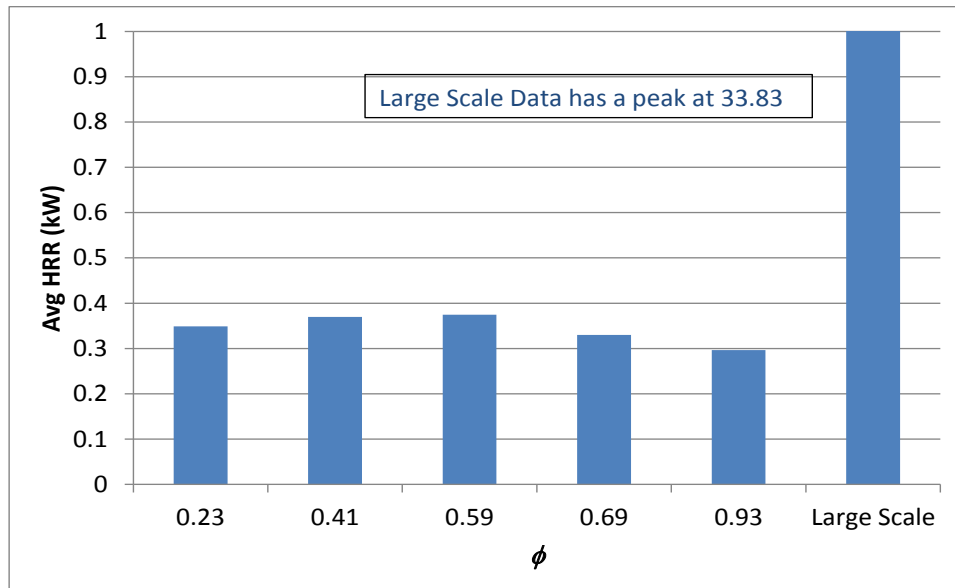


Figure 131 315LSOH Heat Release Rate

4.8.3 1 x 25mm² PVC

Figure 132 shows that the heat release rate (HRR) for the large-scale test is of a far greater magnitude than those of the small-scale tests. The results from the SSTF themselves show a fairly consistent value of roughly 0.2 kW across the range of ϕ values. But the results further highlight the disparity between the two scales, across the different cable types.

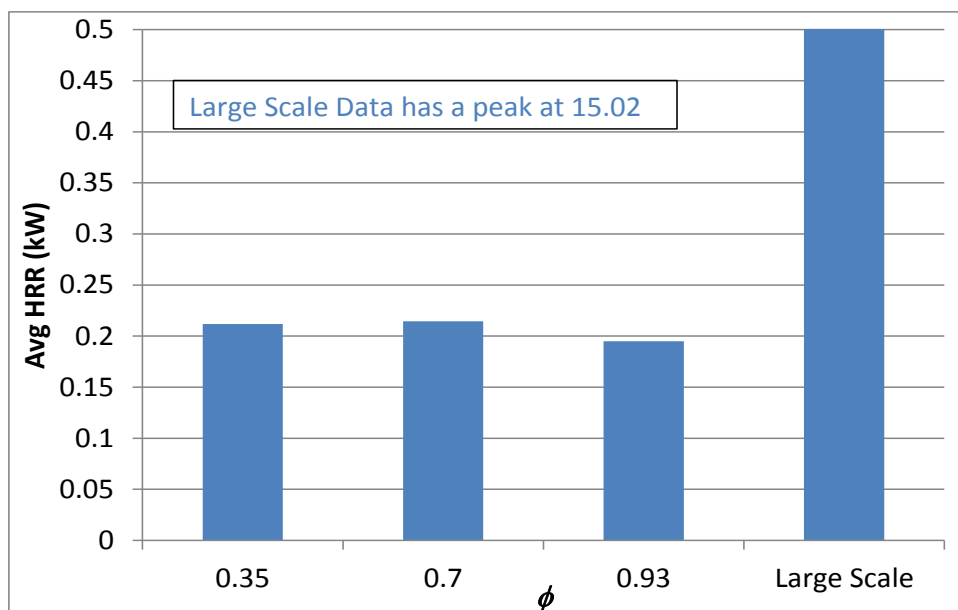
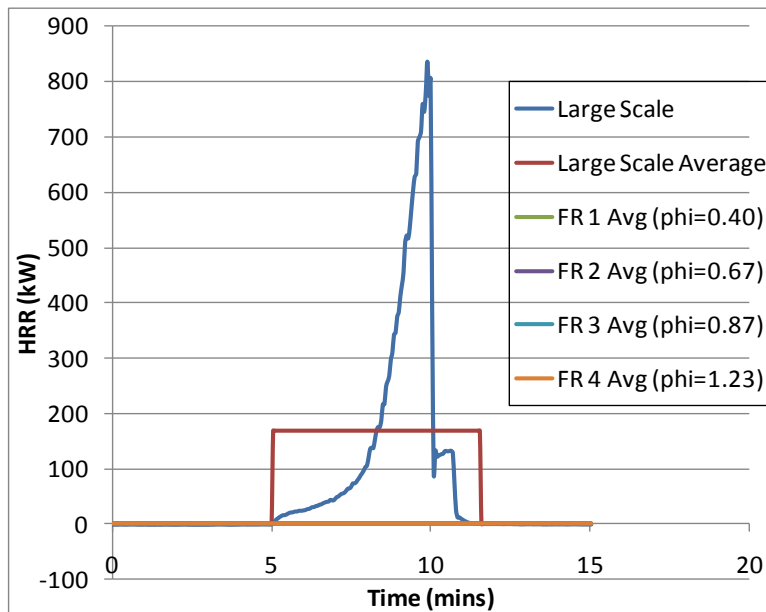


Figure 132 125PVC Heat Release Rate

4.8.3 FR 4804

Figure 133 shows the large-scale data is of a far greater magnitude than the SSTF data. It also shows the general trend of HRR increasing as the value of ϕ decreases.

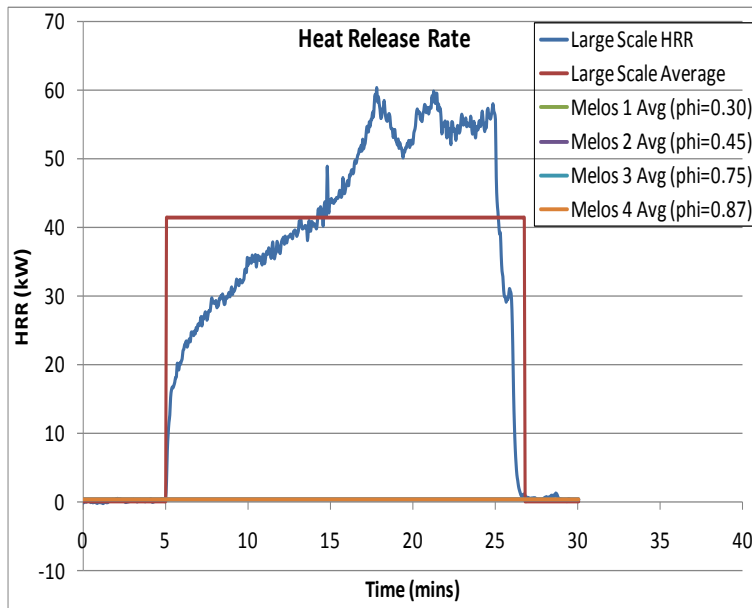


Test	Avg HRR
Large-scale	169
FR 1 ($\phi=0.40$)	0.355
FR 2 ($\phi=0.67$)	0.4
FR 3 ($\phi=0.87$)	0.274
FR 4 ($\phi=1.23$)	0.27

Figure 133 FR 4804 Heat Release Rate

4.8.4 Melos 1006F

Figure 134 shows that the large-scale data is $\approx 200x$ greater than any of the SSTF values. Whilst not as good as the trend shown by FR, there is still an overall trend for the HRR to increase as ϕ goes from 0.87 to 0.30

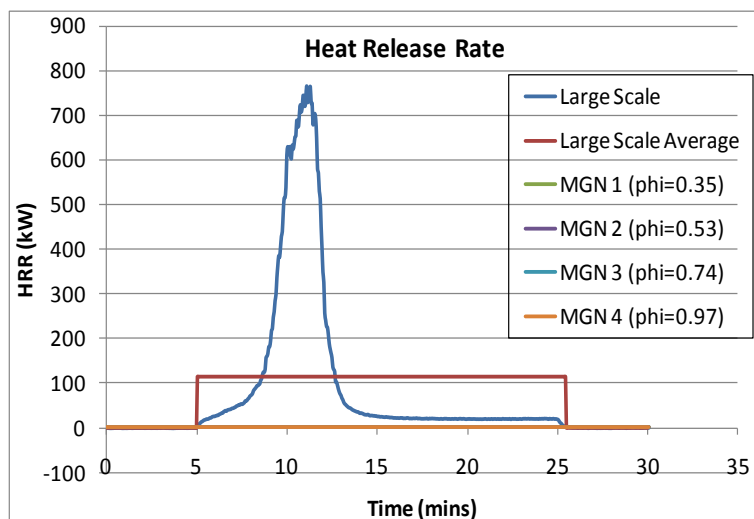


Test	Avg HRR
Large-scale	41.4
Melos 1 ($\phi=0.30$)	0.271
Melos 2 ($\phi=0.45$)	0.271
Melos 3 ($\phi=0.75$)	0.295
Melos 4 ($\phi=0.87$)	0.232

Figure 134 Melos 1006F Heat Release Rate

4.8.5 MGN 09005

The data presented in Figure 135 shows the large-scale HRR greatly exceeds that of the SSTF HRR data. The HRR once more shows an overall trend to increase with falling values of ϕ

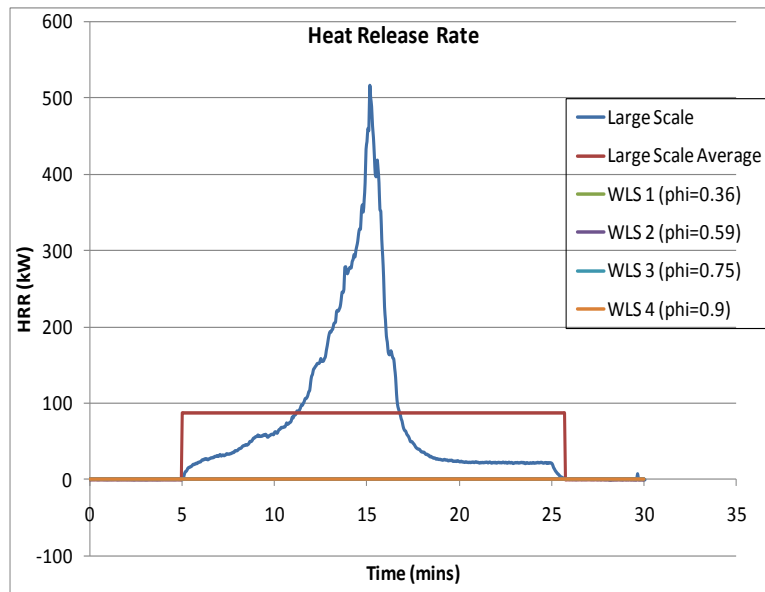


Test	Avg HRR
Large-scale	114.8
MGN 1 ($\phi=0.35$)	0.312
MGN 2 ($\phi=0.53$)	0.325
MGN 3 ($\phi=0.74$)	0.208
MGN 4 ($\phi=0.97$)	0.194

Figure 135 MGN 09005 Heat Release Rate

4.8.6 WLS 08006

The large-scale data shown in Figure 136 shows the large-scale data dwarfing that of the SSTF data. The HRR increases with every decrease in the value of ϕ



Test	Avg HRR
Large-scale	87.8
WLS 1 ($\phi=0.36$)	0.547
WLS 2 ($\phi=0.59$)	0.535
WLS 3 ($\phi=0.75$)	0.45
WLS 4 ($\phi=0.90$)	0.369

Figure 136 WLS 08006 Heat Release Rate

4.9 HRR (kW/) COMPARISON SUMMARY

All the cable types show a huge disparity between the HRR values of the large-scale and SSTF test data, with the large-scale often being a magnitude of 10^2 greater. In terms of trying to correlate the two scales, this disparity makes it virtually impossible as the vast differences in data values would infer a complete lack of correlation.

4.10 HEAT RELEASE (kJ/g)

Using HRR (kW) didn't provide any useable data to establish a correlation between the scales, a different method of heat release rate was used. The previous comparisons were carried out using HRR in kW, the following comparisons used HRR expressed in kJ and were normalised against mass loss. The two data sets

were compared using the conversion of 1kW = 1kJ/s, but this time it was the large-scale data that was converted from kW to kJ .

In [Figure 137](#) it can be seen that for cable types FR and Melos there is a large disparity between the small-scale and large-scale values, with the large-scale being about a quarter of the small-scale values. However 125PVC, MGN and WLS both show more promising results. For MGN the results indicate that the large-scale test would be represented by a value of $0.74 < \phi < 0.97$, whereas the 125PVC and WLS results only point to a $\phi < 0.35$ and < 0.36 , respectively. Whilst the MGN result is promising in terms of the large-scale data actually fitting within the data generated from the small-scale, once again it is suggesting that the large-scale test would be best represented by a ϕ value that is associated with under-ventilated conditions, which is highly unlikely to occur in a test apparatus that was designed such that the tests carried out in it would always be well-ventilated.

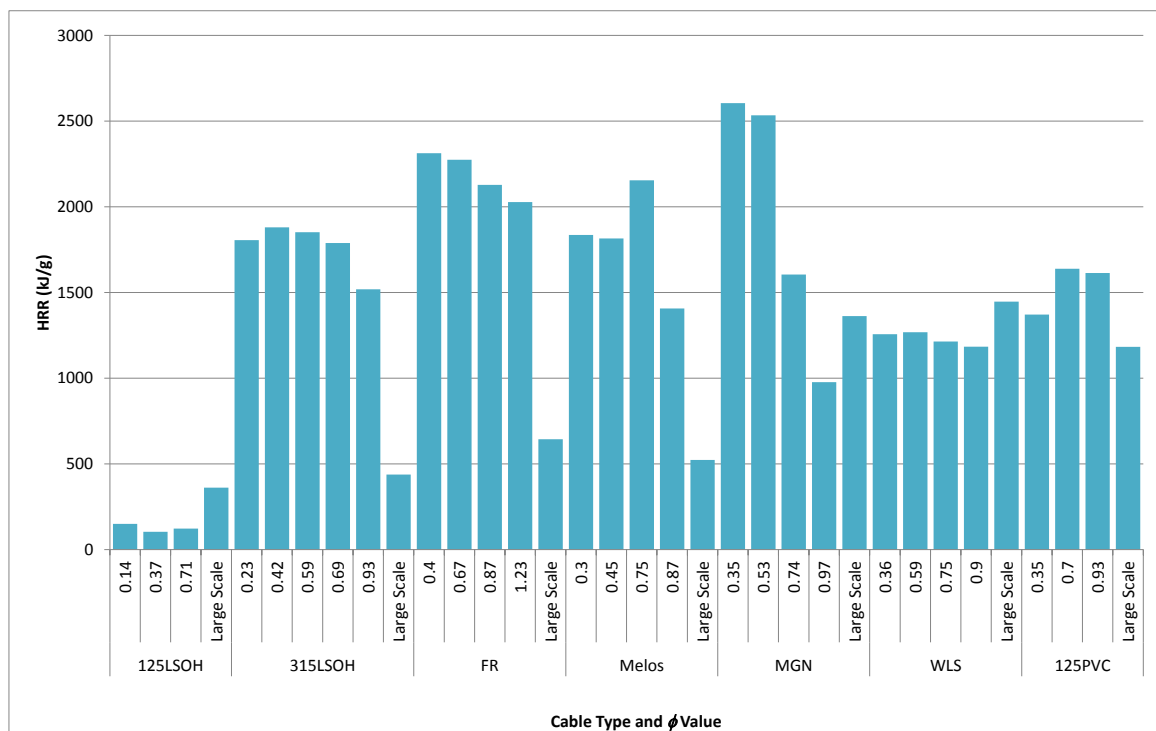


Figure 137 Heat Release Rate (kJ/g)

4.11 HEAT RELEASE (kJ/g) COMPARISON SUMMARY

The change to express HRR in kJ/g over kW/g produced a couple of positive results, those being MGN, WLS and 125PVC as the large-scale data is in the same

range as that from the SSTF. The results for 125PVC and WLS are not definitive as the SSTF data can only provide one boundary, which is the ϕ value that the large-scale test can't exceed; however the smaller the value of ϕ the more problematic testing and analysing of data. The data from MGN is more useful as the SSTF data provides two boundaries, giving a definitive range that the representative ϕ must lie within. However the range given is problematic as according to ISO 19700²⁹ $\phi > 0.75$ is under-ventilated, meaning that the representative ϕ would be that of a ventilation condition considered to be under-ventilated, which is unlikely due to the very high degree of ventilation used with the large-scale method.

5 COMPARING TOXICITY BETWEEN LSOH AND PVC CABLES

The method chosen to compare the toxicity between the two different classifications of cables, PVC and non-halogenated, was FED. FED allows the toxicity of multiple species to be assessed and displayed as a contribution to the overall toxicity. When using FED there are two models that can be used, the N-Gas model developed by NIST and the Purser Model developed (Chapter 1.6.1) The LC₅₀ values for the species and the values for the m and b constants were taken from ISO 13344⁴¹. The analysis was only carried out on cables tested under similar ventilation conditions so that they could be accurately compared, in addition the values of the species concentrations used to generate the FED value were normalised by mass charge concentration where necessary. The results of the analysis are shown in Figure 138.

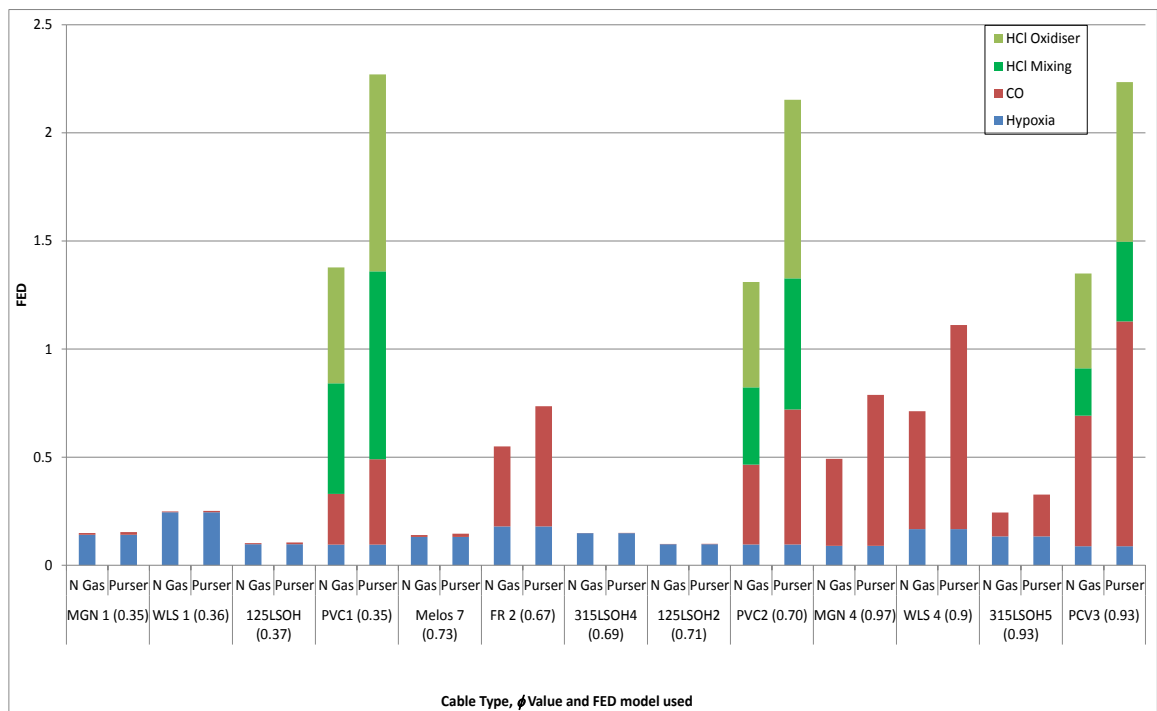


Figure 138 FED Results

The broadest of trends shown by Figure 138 is the increase of FED values with the increasing ϕ values, showing the most under-ventilated conditions to be the most toxicologically dangerous. The different models do show different results for FED values when CO and HCl have a large contribution to the overall value, they don't differ for Hypoxia as it is calculated in the same way for both models. The difference

in terms of CO and HCl contribution is due to the Purser Model assuming the CO₂ driven hyperventilation will affect the toxicity of all the species, not just CO.

Regardless of which model is used they both show the same important difference of PVC cables being more toxic than their LSOH counterparts. Across the entire range of ventilation conditions only 1 LSOH cable has an FED ≥ 1 , whereas the PVC cables, when using the Purser Model all have a FED ≥ 1 , and for two out of the three cases, HCl accounts for the largest contribution to the FED value. [Figure 138](#) shows a differentiation of the HCl contribution into two different categories: Mixing and Oxidiser. The Mixing fraction is the FED contribution by HCl measured directly from the mixing chamber, i.e. HCl present within the fire effluent formed directly from the PVC cable. Whereas the Oxidiser fraction is the HCl contribution sampled from after the secondary oxidiser, this shows the contribution of HCl that would be contained within a stable intermediate compound such as an organochloride, until heated to a higher temperature; the secondary oxidiser is held at a temperature of 900°C. The implications of which are that most well-ventilated fires won't have temperatures in excess of roughly 500-600°C, thus the contribution of HCl from the secondary oxidiser will most likely not be present during that fire stage. In terms of the Purser model this does not have much impact in terms of FED as the FED ≥ 1 even when only considering the mixing chamber fraction. However if using the NIST model then the two well-ventilated tests, $\phi = 0.35$ and $\phi = 0.70$, then the addition of the oxidiser fraction becomes significant. If only the mixing chamber fraction is taken into account then the FED < 1 , however with the oxidiser fraction included the FED > 1 . Whether the oxidiser fraction is included or not the FED values for the PVC cable using the NIST model are still greater than the LSOH equivalents.

6 CONCLUSIONS

This project was carried out in order to assess whether it would be possible to predict the outcome, in terms of toxicity of a large-scale test (prEN-50399-2-1), on a bench scale test method: ISO TS 19700. The testing being carried out was in part to observe the effect of ventilation on the toxicity of the cable materials which is why accuracy of the air flows was of paramount importance; hence the airflows needing to be calibrated and then validated to ensure their accuracy. The Purser furnace was chosen as the test method of choice due to its ability to replicate any given fire stage with accuracy, and its proven reproducibility⁹, further reinforced by the results of the repeat tests carried out during this research. The data collected during this research also allowed for a comparison of toxicity between the PVC and non-halogenated cables across a range of ventilation conditions.

6.COMPARISON OF TOXICITY BETWEEN PVC AND NON-HALOGENATED CABLES

PVC is the dominant material used in cable insulating the world over and due to this high use the implications of such higher toxicity compared to other cables shall be considered. Whilst PVC cables do offer desirable attributes in terms of flexibility, water resistance and fire retardation, the possible consequences of a fire involving PVC cable where it manages to spread throughout a highly populated building unnoticed, giving off toxic products such as HCl and CO must be considered. In order to fully understand the risk:benefit ratio the toxicity data must be compared against any desirable qualities that it may appear to possess over rival materials.

In this study the toxicity of the combustion of the different cable was assessed using FED calculations. For all ventilation conditions the PVC cable had a consistently higher FED value than any of the other LSOH cable materials. For both models the FED value for the PVC cable was >1 for all ventilation conditions.

Of other interest is the amount of HCl that was not released until after being heated to a higher temperature, which was either comparable to the HCl released directly into the effluent, or in some cases greater. In real world terms this would imply that

only half or less of the Cl content of PVC would be converted into gaseous HCl during a typical well-ventilated fire (temperatures $\leq 600^\circ\text{C}$), with the rest of the HCl that was trapped in organic molecules only being released once the room had reached a state of flashover (as this release took place at temperatures $\approx 900^\circ\text{C}$ during small-scale testing).

6.2 COMPARISON OF RESULTS BETWEEN SCALES

To compare the data an array of methods were chosen: equivalence ratio, CO/CO₂ ratio, CO₂/CO ratio and heat release rate: both kW/g and kJ/g, to try and maximise the chances of successfully comparing the two sets of data. However none of the methods were what could be considered overly successful. Of the methods used the equivalence ratio, using the CO₂ based mass loss, was one of the most successful.

For almost all cable types the SSTF data and the CO₂ based yield calculations either intersected or could be seen to be converging. However the majority of these imply a representative ϕ associated with under-ventilated conditions, for a test designed for well-ventilated conditions. That being said, in hindsight it would have been advantageous to carry out further testing on the small-scale at $\phi > 1$ to get a complete picture and better understand what was happening. One of the most important things to come out of the equivalence ratio based comparison was the difference in the large-scale yields between those calculated based on the methodology using burn length and TGA data, and the yields calculated based on the mass of CO₂ produced. Those based on CO₂ produced were almost half of the value of those based on TGA data and were much closer to the SSTF data.

The other methods for comparison were equally as unsuccessful. The attempt to correlate using CO₂/CO ratios, was particularly unsuccessful in trying to compare data. Other attempts such as the CO/CO₂ ratio and Heat Release Rate (kJ) were slightly more successful. However the only conclusion that could be made with any certainty is the ventilation conditions of the large-scale test would be best represented by a lower ϕ , but didn't generate a definitive value. Some results generated were able to infer that the value lay within a certain range, however most of these ranges contained ϕ values associated with under-ventilated conditions. The

chances of a ϕ value that is representative of under-ventilated fire conditions also being representative of conditions within a large-scale test designed to burn cables in an excess of air is highly unlikely.

From the above difficulties encountered with above methods of comparing data the scale of difficulty in trying to correlate between these two tests becomes apparent, if not between large and small-scale tests as a whole. In this research one of the most obvious sources of error would be the estimation of burn length. Firstly it is an estimation of a photograph, and secondly, if not most importantly is the assumption that had to be made about that burn length: that all of the material within it was completely combusted. The cables towards the outer edges of the burn length may only reach temperatures sufficiently hot enough to decompose hydrate sheaths, but leave the bulk of the polymer un-combusted, therefore there will be a mass loss recorded, but no corresponding rise in toxic gases recorded, leading to wrongful estimations in terms of yield calculations. This problem was partially allayed by switching the mass loss estimation to using the mass of CO_2 produced to estimate the amount of cable compound burnt. However this methodology whilst undeniably gave yields closer to those from the SSTF comes with problems of its own. It is assumed that the main polymer used is PE, which isn't the case for all of the cables, but it is a necessary assumption as polymers used such as EVA are co-polymers and as such their molecular weight is variable. Also, possibly more importantly is the assumption that CO_2 is only evolved from the combustion of the main polymer material. For certain cables such as the PVC cable chalk is present, which will decompose to give CO_2 , also for PVC the HCl evolved interferes with CO_2 production in the gaseous phase altering the amount produced. The other major problem that presented itself when using CO_2 based mass loss to calculate yields was that for all cable types using the same assumptions (main polymer content, percentage by mass of main polymer content) the CO_2 yields all came out the same. This is a by-product of the calculation, because to generate a CO_2 yield the mass of CO_2 is divided by the mass of polymer lost, using the mass of CO_2 to generate the mass of polymer is going to result in a fixed ratio: hence the same yield value for different cable types. However the yields for O_2 consumption and CO remain unaffected.

The large volume of air used in the large-scale test poses another possible source of error. Even though the when calculated yields the data are normalised, such

large volumes of air can easily quench the fire plume as it passes over the reaction zone, as has been noted with the cone calorimeter when used to assess toxicity. An additional problem would have been with HCl analysis, given that HCl is a polar compound and thus is “sticky” the large, cold walls of the large-scale apparatus would have provided an ideal place for the HCl molecules to adsorb onto, along with the large exhaust duct promoting the formation of large soot particles, again to which the HCl molecules will readily adsorb onto. However the lack of large-scale HCl data prevents any comments or inferences being made concerning the PVC cables tested on the large-scale apparatus during the course of this research project.

If any further research is to be done into comparing data between the two scales certain things need to be taken from what has been learnt during this research project. Firstly, of paramount importance is an accurate mass loss measurement from the large-scale test, it does not have to be a dynamic measurement during the test, just an accurate before and after weight, including any ash or residue that may have fallen off the cable ladder during the test. However attention has to be paid to the problem of hydrate sheaths decomposing around 300-400°C, generating a mass loss but with no generation of toxic species. Also to be considered is the huge differences in the degree of ventilation between the tests. In terms of the large-scale test rig one of the problems is not directly the large volume of air used, moreover the fact that the vast majority of that air is not involved in the fire zone, resulting in quenching and dilution of the fire gases. Regarding the Steady State Tube Furnace one of the problems encountered with the apparatus in this research was the inability to replicate the very low values of ϕ that were generated by some of the comparison methods as the apparatus used was only able to supply a primary air flow of 25 L/min. This could be solved by incorporating a larger flow meter into the primary air supply allowing greater flows, but this itself poses a problem, as the primary air flow is increased the secondary air flow must be decreased accordingly to maintain a total flow of 50 L/min; the secondary flow is relied upon to produce adequate mixing of the fire gases such that the gas sampled by the analysers is of uniform concentration.

Running parallel to this should be investigating using the CO₂ produced for mass loss estimation. Trying to accurately weigh a cable ladder, including residue that may have fallen off the ladder is hard to remain consistent. However the

measurement of CO₂ is consistent and reliable. The problem is trying to refine the assumptions made in the calculation, mainly that of only the main polymer contributing to the CO₂ production, research into the effect of the presence of chalk in the cable, how it factors in to CO₂ production. Likewise the effect of HCl evolved from PVC has on CO₂ production, by doing this the mass loss can further be refined, leading to more accurate results.

Trying to correlate between scales has proved difficult, toxic gas concentrations have been shown to be condition dependent, sometimes more than material dependent, and going between bench-scale and large-scale inherently involves a rather large change in conditions. The work carried out in this project, whilst not providing definitive answers has produced positive indications. In this work the results from the ϕ based comparison has shown that the two scales can show agreement, however generally at a under-ventilated value of ϕ , but it is a start and can be built on. Further testing carried out at a wider range of ϕ values would allow a better understanding of how the yields vary with ventilation conditions whilst concurrently either reinforcing or dismissing the implications that the large-scale test is best represented by a ϕ associated with under-ventilated conditions. It has allowed a direct comparison of toxicity between PVC and LSOH cables. It has provided information on which comparison methods are not worth investigating further, and conversely those that are. It has shown that the steady state tube furnace is able to accurately replicate a multitude of fire conditions. Finally it has also shown possible sources of errors, or complications in the correlation process that could be investigated and hopefully addressed, with the goal of developing a systematic correlation.

REFERENCE LIST

1. Pollard, D. Cables for Fixed Installations. In *Electric Cables Handbook*, McAllister, D., Ed.; Granada Publishing: 1982; p 175.
2. Field, A. W.; McAllister, D. Materials Used In Cables. In *Electric Cables Handbook*, McAllister, D., Ed.; Granada Publishing: 1982; p 41.
3. Babrauskas, V. Mechanisms and Modes for Ignition of Low-Voltage PVC Wires, Cables, and Cords. Interscience Communications Ltd: London, 2005; pp 291-309.
4. Sillars, R. W. Poly(vinyl chloride). In *Electrical Insulating Materials and their Applications*, Peter Peregrinus Ltd.: Stevenage, 1973; pp 156-160.
5. Hull, T. R.; Wills, C. L.; Lebek, K.; Paul, K.; Price, D. Methodology for Small-scale Toxic Hazard Assessment of Burning Cables. In *Fire and Polymers IV*, 922 ed.; American Chemical Society: 2005; pp 348-363.
6. Hull, T. R.; Wills, C. L.; Lebek, K.; Paul, K.; Price, D. Combustion Toxicity of and Polyolefin and PVC Cables. Unpublished Work, 2010.
7. Drysdale, D. The Mechanism of Gas Phase Combustion. In *An Introduction to Fire Dynamics*, 2nd ed.; John Wiley & Sons: 1998; p 23.
8. Atkins, P.; de Paula, J. The Structure of Chain Reactions. In *Elements of Physical Chemistry*, 4th ed.; Oxford University Press, Inc: New York, 2005; p 277.
9. Lebek, K. Investigation of Fire Toxicity of Polymer Materials and Cables. University of Bolton, 2007.
10. Stevens, M. P. Step-reaction addition and chain-reaction condensation. In *Polymer Chemistry: An Introduction*, 2nd ed.; Oxford University Press. Inc: New York, 2010; pp 17-18.
11. Billmeyer Jr, F. W. Radical Chain (Addition Polymerization). In *Textbook of Polymer Science*, 3rd ed.; John Wiley & Sons: 1987; pp 49-81.
12. Stevens, M. P. Chain-reaction Polymerization. In *Polymer Chemistry: An Introduction*, 2nd ed.; Oxford University Press. Inc: New York, 2010; pp 16-17.
13. Ebdon, J. Polymer Science & Technology. Unpublished Work, 2009.
14. Billmeyer Jr, F. W. Step-reaction polymerization. In *Textbook of Polymer Science*, 3rd ed.; John Wiley & Sons: 1987; pp 14-15.
15. Beyler, C. L.; Hirschler, M. M. Thermal Decomposition of Polymers. In *The SFPE Handbook of Fire Protection Engineering*, 2nd ed.; Beyler, C. L., Custer, R. L. P., DiNenno, P. J., Drysdale, D., Hall Jr, J. R., Walton, W. D., Watts, J. M., Eds.; National Fire Protection Association: Quincy, 1995; pp 99-117.

16. Hilado, C. J. The Burning Process on a Micro-scale. In *Flammability Handbook for Plastics*, 5th ed.; Technomic: Lancaster, 1998; pp 29-31.
17. Kaczorek, K. Bench-scale Fire Toxicity Measurements of Polymers and Cables. University of Central Lancashire, 2009.
18. Hirschler, M. M. Chemical Aspects of Thermal Decomposition of Polymeric Materials. In *Fire Retardancy of Polymeric Materials*, 1 ed.; Grand, A. F., Wilkie, C. A., Eds.; Marcel Dekker Inc: New York, 2000; pp 27-79.
19. Price, D.; Anthony, G.; Carty, P. Char Structure. In *Fire Retardant Materials*, Horrocks, A. R., Price, D., Eds.; Woodhead Publishing Limited: Cambridge, 2010; pp 18-19.
20. Hull, T. R. Reaction to Fire Testing and Assessment of Fire Toxicity. In *Advances in Fire Retardant Materials*, Horrocks, A. R., Price, D., Eds.; Woodhead Publishing Ltd: 2008.
21. Hull, T. R. Factors affecting Ignitability and Fire Development. In *Advances in Fire Retardant Materials*, Horrocks, A. R., Price, D., Eds.; Woodhead Publishing Limited: Cambridge, 2009.
22. Hull, T. R.; Stec, A. A. Introduction Polymers and Fire. In *Fire Retardancy of Polymers*, Hull, T. R., Kandola, B. K., Eds.; The Royal Society of Chemistry: Cambridge, 2009; pp 6-7.
23. Drysdale, D. Ignition: The Initiation of Flaming Combustion. In *An Introduction to Fire Dynamics*, 2nd ed.; John Wiley & Sons: 1998; p 193.
24. Quintiere, J. G. Ignition. In *Principle of Fire Behaviour*, Delmar Publishers: 1998; p 66.
25. Drysdale, D. Pilot Ignition of Solids. In *An Introduction to Fire Dynamics*, 2nd ed.; John Wiley & Sons: 1998; p 212.
26. Drysdale, D. Spontaneous Ignition of Combustible Solids. In *An Introduction to Fire Dynamics*, 2nd ed.; John Wiley & Sons: 1998; p 227.
27. Drysdale, D. Introduction. In *An Introduction to Fire Dynamics*, 2 ed.; John Wiley & Sons: 1998; p 1.
28. Quintiere, J. G. The Evolution of Fire Science. In *Principles of Fire Behaviour*, Delmar Publishers: Albany, 1998; p 2.
29. ISO TS 19700 Controlled equivalence ratio method for the determination of hazardous components of fire effluents. 2007.
30. Karlsson, B.; Quintiere, J. G. General Description of Fire Growth In An Enclosure. In *Enclosure Fire Dynamics*, CRC Press: 2000; p 14.
31. Daeid, N. N. An Introduction to Fires and Fire Investigation. In *Fire Investigation*, 1st ed.; Daeid, N. N., Ed.; CRC Press LLC: 2004; pp 1-12.

32. Quintiere, J. G. Compartment Fires. In *Principles of Fire Behaviour*, Delmar Publishers: 1998; p 170.
33. DeHaan, J. D. The Nature and Behaviour of Fire. In *Kirk's Fire Investigation*, 6th ed.; Pearson Education, Inc.: 2007; pp 23-64.
34. Stec, A. A.; Hull, T. R.; Lebek, K. Characterisation of the steady state tube furnace (ISO TS 19700) for fire toxicity assessment. *Polymer Degradation and Stability* **2008**, *93* (11), pp 2058-2065.
35. Pitts, W. M. The global equivalence ratio concept and the formation mechanisms of carbon monoxide in enclosure fires. *Progress in Energy and Combustion Science* **1995**, *21* (3), pp 197-237.
36. ISO 19703 Generation and Analysis of Toxic Gases. 2005.
37. BS ISO 19706. Guidelines for Assessing the Fire Threat to People. 2007.
38. Fire Statistics, United Kingdom 2006. London 2008.
39. Hull, T. R. Challenges in fire testing: reaction to fire tests and assessment of fire toxicity. In *Advances in Fire Retardant Materials*, Horrocks, A. R., Price, D., Eds.; Woodhead Publishing Limited: Cambridge, 2009; pp 255-256.
40. Hull, T. R.; Paul, K. T. Bench-scale assessment of combustion toxicity--A critical analysis of current protocols. *Fire Safety Journal* **2007**, *42* (5), pp 340-365.
41. ISO 13344 Estimation of The Lethal Toxic Potency of Fire Effluents. 2004.
42. Stec, A. A.; Hull, T. R. Assessment of Fire Toxicity from Polymer Nanocomposites. In *Fire Retardancy of Polymers: New Strategies and Mechanisms*, Hull, T. R., Kandola, B. K., Eds.; The Royal Society of Chemistry: Cambridge, 2009; pp 405-417.
43. Purser, D. Toxicity Assessment of Combustion Products. In *SFPE Handbook of Fire Protection Engineering*, Third ed.; DiNenno, P. J., Drysdale, D., Beyler, C. L., Walton, W. D., Custer, R. L. P., Hall Jr, J. R., Watts, J. M., Eds.; National Fire Protection Agency: Quincy, 2002; pp 2-83-2-173.
44. Blomqvist, P.; Hertzberg, T.; Dalene, M.; Skarping, G. Isocyanates, Aminoisocyanates and Amines from Fires - A Screening of Common Materials Found In Buildings. *Fire and Materials* **2003**, *27*, pp 275-294.
45. Purser, D. Halogen Acid Vapour-phase Systems. In *Fire Retardancy of Polymers*, Hull, T. R., Kandola, B. K., Eds.; The Royal Society of Chemistry: Cambridge, 2009; pp 393-394.
46. Purser, D. Influence of Fire Retardants on Toxic and Environmental Hazards from Fires. In *Fire Retardancy of Polymers*, Hull, T. R., Kandola, B. K., Eds.; The Royal Society of Chemistry: Cambridge, 2009; pp 381-404.

47. Hull, T. R. Challenges in fire testing: reaction to fire tests and assessment of fire toxicity. In *Advances in Fire Retardant Materials*, Horrocks, A. R., Price, D., Eds.; Woodhead Publishing Limited: Cambridge, 2009; pp 258-261.
48. Hull, T. R.; Lebek, K.; Pezzani, M.; Messa, S. Comparison of toxic product yields of burning cables in bench and large-scale experiments. *Fire Safety Journal* **2008**, *43* (2), pp 140-150.
49. Babrauskas, V.; Gann, R. G.; Levin, B. C.; Paabo, M.; Harris, R. H.; Peacock, R. D.; Yusa, S. A methodology for obtaining and using toxic potency data for fire hazard analysis. *Fire Safety Journal* **1998**, *31* (4), pp 345-358.
50. ISO 13344. Estimation of lethal toxic potency of fire effluents. 1996.
51. ISO 5660-2. 2002.
52. ISO 5660-1 The Cone Calorimeter Test. 1993.
53. Hull, T. R. Challenges in fire testing: reaction to fire tests and assessment of toxicity. In *Advances in Fire Retardant Materials*, Horrocks, A. R., Price, D., Eds.; Woodhead Publishing Limited: Cambridge, 2008; pp 255-290.
54. Hull, T. R. Bench-scale measurement of heat release, The Cone Calorimeter. In *Advances in Fire Retardant Materials*, Horrocks, A. R., Price, D., Eds.; Woodhead Publishing Limited: Cambridge, 2008; pp 269-271.
55. <http://www.pslc.ws/macrog/mpm/analysis/cone.htm>. 2010. 20-9-2010.
Ref Type: Online Source
56. NF X 70-100-1 Fire Tests: Analysis of Gaseous Effluents. Pt 1 Methods for Determining Gases Produced by Thermal Degradation. Pt 2 Tubular Furnace Degradation Method. 2001.
57. BS 7900 Tube Furnace Method for The Determination of Toxic Product Yields in Fire Effluents. 2003.
58. ISO 19701 Methods for Sampling and Analysis of Fire Effluents. 2005.
59. ISO 11358 Plastics - Thermogravimetry (TG) of Polymers - General Principles. 1997.
60. Billmeyer Jr, F. W. Analysis and Testing of Polymers. In *Textbook of Polymer Science*, 3rd ed.; John Wiley & Sons: 1987; pp 229-257.
61. Dollimore, D. Thermogravimetry. In *Thermal Analysis: Techniques and Applications*, Charsley, E. L., Warrington, S. B., Eds.; The Royal Society of Chemistry: Cambridge, 1992; pp 31-58.
62. O'Mara, M. M. Combustion of PVC. *Pure and Applied Chemistry* **1977**, *49*, 649-660.
63. IEC 60332 -3 Tests on Electric Cables Under Fire Conditions - Part 3-10: Test for Vertical Flame Spread of Vertically Mounted Bunched Wires or Cables. 2009.
64. prEN 50399-2-1 Common test methods for cables under fire conditions - Heat release and smoke production measurement on cables during flame spread test. 2010.

65. Nakayama, Y.; Boucher, R. F. Reynolds Number. In *Introduction to Fluid Mechanics: Revised*, Boucher, R. F., Ed.; Butterworth Heinemann: 1998; p 46.
66. Hull, T. R.; Lebek, K.; Pezzani, M.; Messa, S. Comparison of toxic product yields of burning cables in bench and large-scale experiments. *Fire Safety Journal* **2008**, *43* (2), pp 140-150.
67. Hull, T. R.; Carmen, J. M.; Purser, D. Prediction of CO Evolution from Small-scale Polymer Fires. *Polymer International* **2000**, *49*, p 1256.

Appendix A

Calculating Percentage by Mass for all Cable Types

1 x 2.5 mm² LSOH

Sample	Length of Cable (cm)	Cable Mass (g)	Copper Mass (g)	Cable Compound Mass (g)
1	10cm	3.3	2.03	1.27

Component	Avg % By Mass
Copper	61.52
Cable Compound	38.48

1 x 25 mm² PVC

Sample	Length of Cable (cm)	Cable Mass (g)	Copper Mass (g)	Cable Compound Mass (g)
1	10.7cm	26.6	19.81	6.78

Component	Avg % By Mass
Copper	74.47
Cable Compound	25.49

3 x 1.5 mm² LSOH

Sample	Length of Cable (g)	Cable Mass (g)	Sheath & Bedding Mass (g)	Copper Mass (g)			Insulator Mass (g)			Total Copper (g)	Total Cable Compound (g)
				1	2	3	1	2	3		
1	10.7cm	16.11	10.84	1.37	1.33	1.33	0.41	0.41	0.41	4.03	12.07

Component	Avg % By Mass
Copper	25.02
Cable Compound	74.92

Melos 1006F ATH

Sample	Length of Cable (g)	Cable Mass (g)	Sheath Mass (g)	Copper Mass (g)			Insulator Mass (g)			Total Copper (g)	Total Cable Compound (g)
				1	2	3	1	2	3		
1	10.0cm	13.01	7.76	1.34	1.35	1.34	0.41	0.41	0.4	4.03	8.98

Component	Avg % By Mass
Copper	30.98
Cable Compound	69.02

MGN 09005

Sample	Length of Cable (g)	Cable Mass (g)	Sheath Mass (g)	Copper Mass (g)			Insulator Mass (g)			Total Copper (g)	Total Cable Compound (g)
				1	2	3	1	2	3		
1	10.0cm	10.74	5.62	1.31	1.32	1.31	0.39	0.39	0.39	3.94	6.79

Component	Avg % By Mass
Copper	36.69
Cable Compound	63.22

FR 4804

Sample	Length of Cable (g)	Cable Mass (g)	Sheath Mass (g)	Copper Mass (g)			Insulator Mass (g)			Total Copper (g)	Total Cable Compound (g)
				1	2	3	1	2	3		
1	10	10.78	5.48	1.35	1.35	1.36	0.41	0.41	0.42	4.06	6.72

Component	Avg % By Mass
Copper	37.66
Cable Compound	62.34

WLS 08006

Sample	Length of Cable (g)	Cable Mass (g)	Sheath Mass (g)	Copper Mass (g)			Insulator Mass (g)			Total Copper (g)	Total Cable Compound (g)
				1	2	3	1	2	3		
1	10	9.22	3.94	1.36	1.35	1.34	0.41	0.41	0.41	4.05	5.17

Component	Avg % By Mass
Copper	43.93
Cable Compound	56.07

Appendix B

Calculating Equivalence Ratio

Using 315LSOH4 as an example, following the calculation from BS 7990

$$\phi = \frac{\dot{m}_{loss} \times \Psi_O}{O}$$

\dot{m}_{loss} = mass loss rate (mg/min)

Ψ_O = Stoichiometric Oxygen demand

O = Oxygen Supply Rate (mg/min)

Calculating Mass Loss Rate:

$$\dot{m}_{loss} = m_{loss} \times \dot{b}$$

$$m_{loss} = \frac{\text{cable compound weight (mg)}}{\text{specimen length (mm)}} - \frac{\text{cable compound residue weight (mg)}}{\text{residue length (mm)}}$$

Cable mass = 99.85g, of which 74.81g is cable compound (calculated from % by mass data), => 25.04g Copper Conductor

Residue mass = 59.5g of which 25.04g is Cu => 34.46g cable compound residue.

$$m_{loss} = \frac{74.81g \times 1000}{700mm} - \frac{34.46g \times 1000}{700mm} = 57.64 \text{ mg/mm}$$

\dot{b} = feed rate (mm/min)

$$\dot{b} = 11.97 \text{ mm/min}$$

$$\dot{m}_{loss} = 57.64 \times 11.96 = \mathbf{689.37 \text{ mg/min}}$$

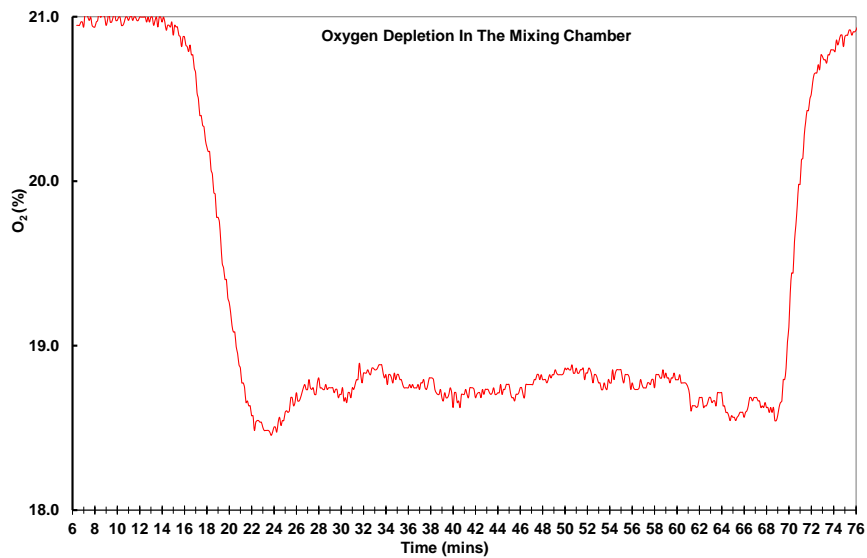
Calculating Stoichiometric Oxygen Demand

$$\Psi_o = \frac{D_{O_2} \times 1330}{C_{m.loss}}$$

D_{O_2} = Oxygen Depletion

$C_{m.loss}$ = mass charge concentration

$$D_{O_2} = \frac{\text{Oxygen depletion in the mixing chamber (\%)}}{100}$$



$$D_{O_2} = \frac{2.27\%}{100} = 0.0227$$

$$C_{m.loss} = \frac{\dot{m}_{loss}}{\dot{a}}$$

\dot{m}_{loss} = mass loss rate (mg/min)

\dot{a} = Total Air (l/min)

$$C_{m.loss} = \frac{689.37}{50} = 13.79 \text{ (mg/l)}$$

$$\Psi_o = \frac{0.0227 \times 1330}{13.79} = 2.19$$

Calculating Oxygen Supply Rate

$$O = P \times 0.2095 \times 1330$$

P = Primary air flow (l/min)

$$O = 7.90 \times 0.2095 \times 1330 = \mathbf{2201}$$

Calculating ϕ

$$phi = \frac{689.37 \times 2.19}{2201} = 0.69$$

Appendix C

Calculating Large-scale Yields

Using 315LSOH LS.

Data supplied from large-scale test technician

Damage Length = 1.99m

Number of Cables = 15

Cable Mass Data

10.7cm of cable = 16.11g

1.99m of cable = $(16.11\text{g}/10.7\text{cm}) \times 199\text{cm} = 299.62\text{g}$

=>15 cables = 4494g total cable compound

Cable Composition By Mass Data:

52.70% is Sheath = 2368.34g

14.59% is Bedding = 655.67g

7.64% is Insulator = 343.34g

From TGA Mass Loss Data

Sheath mass loss = 50.49% = 1195.77g lost

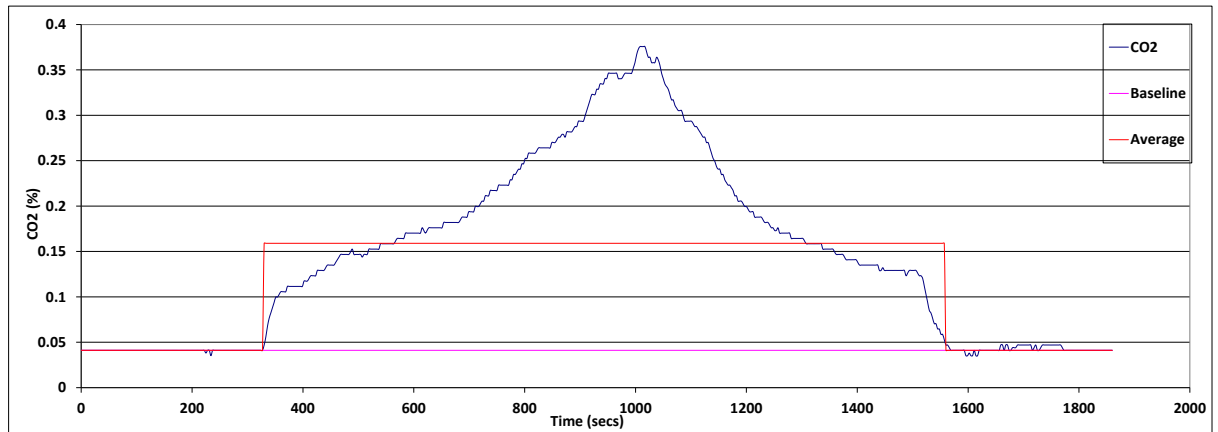
Bedding mass loss = 36.66% = 240.37g lost

Insulator mass loss = 96.16% = 330.16g lost

Assuming complete combustion total mass loss = 1766.30g*

*Mass loss based on TGA data, this mass loss value can be replaced with the mass loss value based on CO₂ produced (as shown how to calculate in), but the resultant yields will then be based on the mass loss values from CO₂ produced.

CO₂ Yield:



To calculate the yield of CO₂, the average CO₂ needs to be calculated first.

$$\text{Average } CO_2 = \frac{\text{Total } CO_2}{\text{Time Integrated Over}}$$

Integrating under the curve gives a total CO₂ of 195.45 %s⁻¹

Time Integrated Over = 1227 seconds

$$\text{Average } CO_2 = \frac{195.45}{1227}$$

The average CO₂ then needs to be converted into a volume:

$$CO_2(L) = \frac{\text{Average } CO_2}{100} \times \text{Total Air (L)} \times \text{Time(s)}$$

$$CO_2 = \frac{0.59}{100} \times 833 \times 1227$$

$$CO_2 = 1628.11$$

The volume of CO₂ is then converted into a mass:

$$CO_2(g) = CO_2(L) \times \frac{\text{Molar Mass } CO_2}{24 \text{ (volume occupied by 1 mole of gas)}}$$

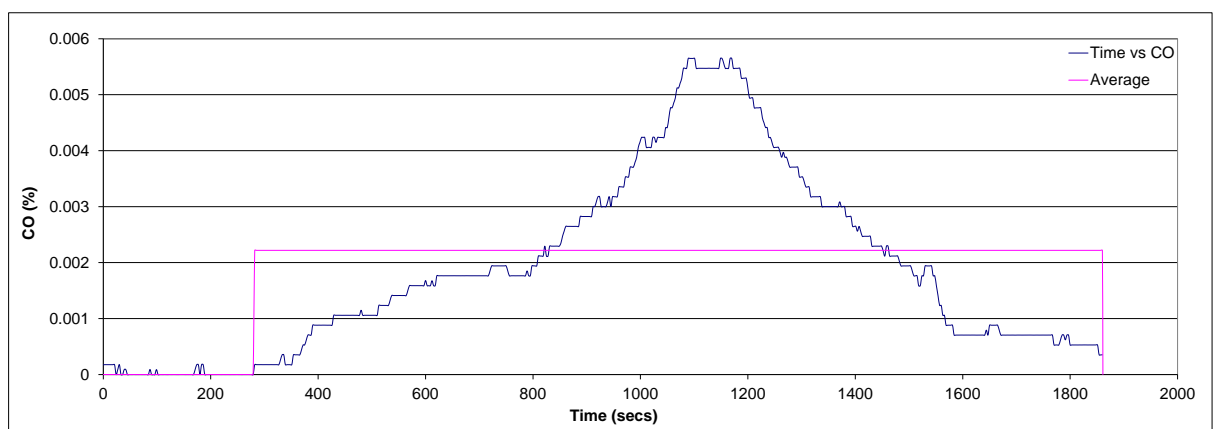
$$CO_2 (g) = 1628.11 \times \frac{44}{24}$$

$$CO_2 = 2984.86$$

$$CO_2 \text{ Yield} = \frac{\text{Mass of } CO_2(g)}{\text{Mass Loss (g)}}$$

$$\text{Yield of } CO_2 = 1.69 \text{ g/g}$$

CO Yield:



The CO yield is calculated in much the same way:

$$\text{Average } CO = \frac{\text{Total } CO}{\text{Time Integrated Over}}$$

Integrating under the curve gives a total CO of 3.49 %s⁻¹

Time Integrated Over = 1572 seconds

$$\text{Average } CO = \frac{3.49}{1572} = 0.0022$$

The average CO then needs to be converted into a volume:

$$CO(L) = \frac{\text{Average } CO}{100} \times \text{Total Air (L)} \times \text{Time(s)}$$

$$CO = \frac{0.0022}{100} \times 833 \times 1572$$

$$CO = 28.81 L$$

The volume of CO is then converted into a mass:

$$CO (g) = CO (L) \times \frac{\text{Molar Mass } CO}{24 (\text{volume occupied by 1 mole of gas})}$$

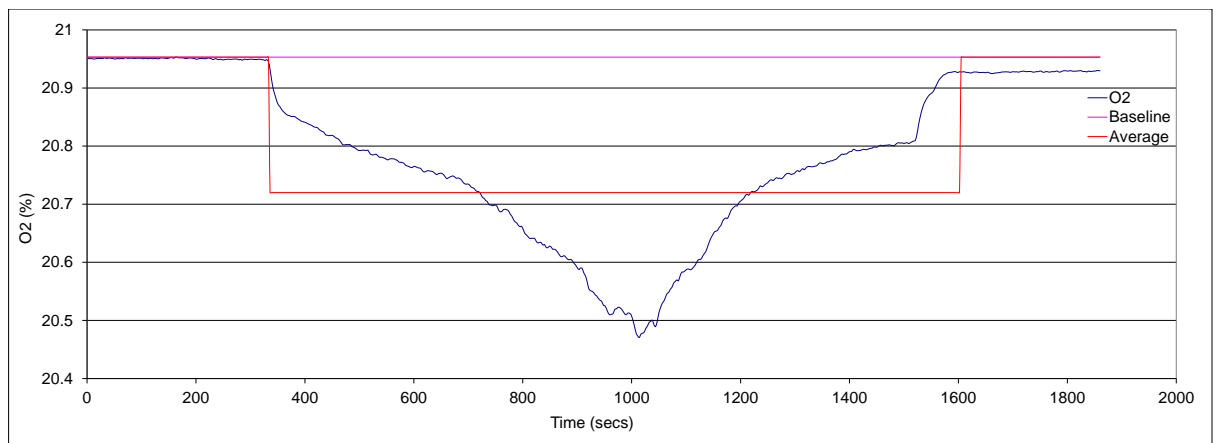
$$CO (g) = 28.81 \times \frac{28}{24}$$

$$CO = 33.61$$

$$CO \text{ Yield} = \frac{\text{Mass of } CO(g)}{\text{Mass Loss (g)}}$$

$$CO \text{ Yield} = 0.0190 \text{ g/g}$$

O₂ Depletion Yield:



The O₂ Consumed (g/g) is calculated in the same way

$$\text{Average } O_2 = \frac{\text{Total } O_2}{\text{Time Integrated Over}}$$

Integrating the area between the Baseline and O₂ curves generates the value for total O₂ consumed

$$\text{Total } O_2 \text{ consumed} = 294.37 \text{ \%s}^{-1}$$

$$\text{Time Integrated Over} = 1266 \text{ seconds}$$

$$\text{Average } O_2 \text{ Consumed} = \frac{294.37}{1266} = 0.233$$

The average O_2 consumed (%) then needs to be converted into a volume:

$$O_2 \text{ Consumed (L)} = \frac{\text{Average } O_2 \text{ Consumed}}{100} \times \text{Total Air (L)} \times \text{Time(s)}$$

$$O_2 \text{ Consumed (L)} = \frac{0.233}{100} \times 833 \times 1266$$

$$O_2 = 2457.17 \text{ L}$$

The volume of O_2 consumed is then converted into a mass:

$$O_2 \text{ Consumed (g)} = O_2 \text{ Consumed (L)} \times \frac{\text{Molar Mass } O_2}{24 \text{ (volume occupied by 1 mole of gas)}}$$

$$O_2 \text{ Consumed (g)} = 2457.17 \times \frac{32}{24}$$

$$O_2 \text{ Consumed (g)} = 3276.23$$

$$O_2 \text{ Consumed (g/g)} = \frac{\text{Mass of } O_2 \text{ Consumed (g)}}{\text{Mass Loss (g)}}$$

$$O_2 \text{ Yield} = 1.85 \text{ g/g}$$

Appendix D

CO₂ Based Mass loss Calculations

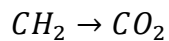
Using 315LSOH as an example:

The cable is LSOH so a reasonable assumption would be that its 30% PE and 70% ATH.

Mass of CO₂ produced = 2984.86g

Mass of CO = 33.82g

Because the mass of CO is negligible it is assumed that when burnt the entirety of the PE content produces only CO₂.



The molar ratio is 1:1, hence 14g of CH₂ gives 44g CO₂,

Conversely 44g CO₂ requires 14g PE, => 2984.86g of CO₂ requires $2984.86 \times \frac{14}{44}$ g of PE.

Mass of PE required = 949.73g.

However the mass of PE only accounts for 30% of the total cable compound, thus the total weight of cable compound = $949.73 \times \frac{100}{30} = 3165.77$ g

Total Mass Loss = 3165.77g